HOKKAIDO UNIVERSITY

Title	The Functionalization of Surface Modified Silicon
Author(s)	魯, 旭
Degree Grantor	北海道大学
Degree Name	博士(工学)
Dissertation Number	甲第12017号
Issue Date	2015-09-25
DOI	https://doi.org/10.14943/doctoral.k12017
Doc URL	https://hdl.handle.net/2115/63380
Type	doctoral thesis
File Information	Lu_Xu.pdf

Hokkaido University Collection of Scholarly and Academic Papers : HUSCAP

The Functionalization of Surface Modified Silicon

By
Xu Lu

Division of Materials Science and Engineering
Graduate School of Engineering
Hokkaido University
Sapporo, JAPAN

2015

CONTENTS

Chapter 1. Introduction 1

1.1 General introduction of Si: properties and applications 1

1.2 Introduction of surface modified Si 8

1.2.1 Surface modified Si prepared by anodization 8

1.2.2 Surface modified Si prepared by metal assisted corrosion 11

1.2.3 Other methods for preparation of surface modified Si 13

1.3 Novel characteristics of the surface modified Si 14

1.3.1 The fluorescence properties of surface modified Si 14

1.3.2 Other optical properties of surface modified Si 16

1.4 The problems of surface modified Si and the corresponding solutions 19

1.4.1 The problems of surface modified Si 19

1.4.2 The possible solutions for the weaknesses of surface modified Si 22

1.5 Content of this thesis 24

Chapter 2. Preparation and Characterization of Surface Modified Silicon 26

2.1 Preparation and characterization of p-type surface modified Si by electrochemical anodization 26

2.1.1 Experimental method for p-type surface modified Si 26

2.1.2 Surface structure of the prepared p-type surface modified Si 28

2.1.3 Photoluminescence and reflectance properties of p-type surface modified Si.... 29

2.2 Preparation and characterization of n-type surface modified Si by electrochemical anodization 33

2.2.1 Experimental method for n-type surface modified Si 33

2.2.2 Surface structure of the prepared n-type surface modified Si 34

2.2.3 Photoluminescence and properties of n-type surface modified Si 35

2.2.4 Formation mechanism of p and n-type surface modified Si 36

2.3 Preparation and characterization of n-type surface modified Si by metal assisted method 38

2.3.1 Experimental method for Ag-assisted n-type surface modified Si 38

2.3.2 Surface structure and photoluminescence properties of Ag-assisted surface modified Si 39

Chapter 3. The Influence of Cu Coating on Photoluminescence Behaviors from the Surface Modified Silicon Prepared by Electrochemical Anodization 43

3.1 The influence of Cu coating on fluorescent properties from hydrofluoric acid treated aged surface modified silicon 43

3.1.1 Introduction 43

3.1.2 Experimental method for Cu-PSi 44

3.1.3 Surface structure of Cu-coated HF-treated aged PSi 46

3.1.4 Photoluminescence properties of Cu-coated HF-treated aged PSi 47

3.1.5 Characterizations of Cu-coated HF-treated aged PSi 53

3.1.6 Photoluminescence properties of Cu-coated HF-treated aged n-type PSi 57

3.2 The fluorescence properties of nanoisland-structured SiO_x/Cu_xO composite 62

3.2.1 Introduction 63
3.2.2 Experimental method for SiO_x/Cu_xO nano-island composite 63
3.2.3 Surface structure of the prepared SiO_x/Cu_xO composite 64
3.2.4 Formation mechanism of SiO_x/Cu_xO nano-island composite 69
3.2.5 Photoluminescence properties of SiO_x/Cu_xO nano-island composite 71

Chapter 4. The Enhanced Far Infrared Emission from Semiconductor and Metal Composite Deposited on Surface Modified Silicon 75

4.1 Introduction of terahertz 75

4.2 New terahertz emission materials 76

4.3 Enhanced terahertz emission from Cu_xO/metal thin film deposited on surface modified silicon 77

4.3.1 Experimental method 77
4.3.2 THz emission mechanism from surface field 79
4.3.3 THz emission properties from Cu_xO/AuCu oxidized in air 81
4.3.4 THz emission properties from heated Cu_xO/AuCu 83
4.3.5 Surface and interface structure of CuxO/AuCu 87

Chapter 5. Summary and Future Work 92

Reference 96

Chapter 1. Introduction

1.1 General introduction of Si: properties and applications

Nowadays semiconductors have become one of the most important group of materials for wide range of applications from optical devices to electronics and so on. Different from conductors and insulators, semiconductors such as silicon (Si), germanium (Ge), GaAs, and GaN possess the electrical conductivities in between the conductors and insulators at room temperature. Additionally, the conductivity of semiconductors can be controlled by changing the dopants and dopant concentration, *e. g* phosphorus and boron, even small doping amount (~ parts per million) can change the conductivity significantly. This property made semiconductor an important material in both scientific fields and modern technological and industrial applications. Among them, the development of Silicon (Si) semiconductor played a crucial role in modern semiconductor industry.[1–9]

As mentioned above, the electrical conductivity of semiconductor is between conductors and insulators. This phenomenon is a result of the changes in the electronic structure (energy band structure) of materials from a conductor to a semiconductor and an insulator. For bulk materials, band gap energy (or band gap in short) is the energy difference of the conduction band and valence band. At absolute

zero temperature, electrons will be restrained in valence band; there are no free electrons in the conduction band. As the temperature increases, some electrons in the valence band can absorb the thermal energy and jump over the band gap. These thermal excited electrons can fill the empty levels in conduction band, becoming free electrons. The electrical conductivity of a material is determined by the numbers of the free electrons in the conduction band or the holes in the valence band, which has a close relationship with the energy value of band gap. A conductor such as a metal has enough small band gap (in the order of k_BT eV), so at room temperature, part of the electrons can jump to the conduction band, create good conductivity. In contrast with a conductor, an insulator has large energy gap that with the thermal energy at room temperature there is no electron can bridge the energy gap to make it conductive. In general, materials with intermediate band gap value (1.0 – 3.0 eV) between conductors and semiconductors are categorized as semiconductors. The schematic diagram of the band gap structures corresponding to conductors, semiconductors and insulators is shown in Figure 1.1.

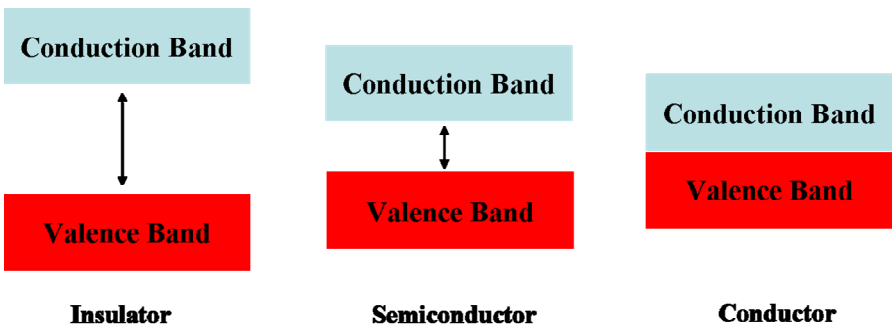


Figure 1.1. The schematic of the band gap values of insulator, semiconductor and conductor

Under room temperature, intrinsic semiconductors still have a low conductivity. However, according to the doping treatment, electrical conductivity of a semiconductor can be varied in a large range. For example, Si is a member of IV group elements *i.e.* with the outermost electronic orbitals (p-orbitals) consisting of four electrons. In condense state, a Si atom has four valence bonds with its neighbors. If a V group element such as phosphorus (P) is doped into Si, as the outermost electronic orbital of phosphorus has five electrons, four electrons from phosphorus can make bonds with Si. The other one electron in P will play a role as free electrical carriers, changing the conductivity of the doped Si. Because electron is a negative particle, this phosphorus doped Si is called as negative Si (n-type Si). In contrary, if an III group element like boron is doped, the outermost electronic orbital of boron has three electrons. Making four bonds between B and Si generates a hole (a bond lack of an electron) which will be responsible for the electrical conductivity of the doped Si similar to the electron in n-type Si. This boron doped Si is named as positive Si or p-type Si. The schematic diagram of the difference between n and p-type semiconductor is shown in Figure 1.2).

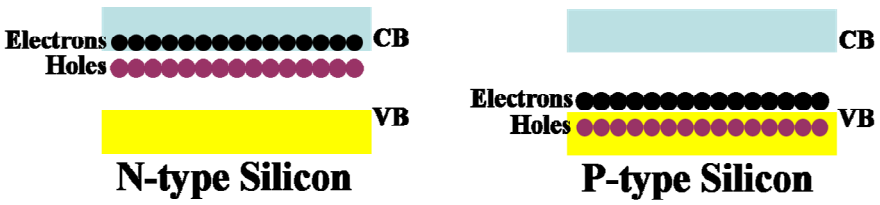


Figure 1.2. The schematic illustration of the difference between N and P type semiconductor

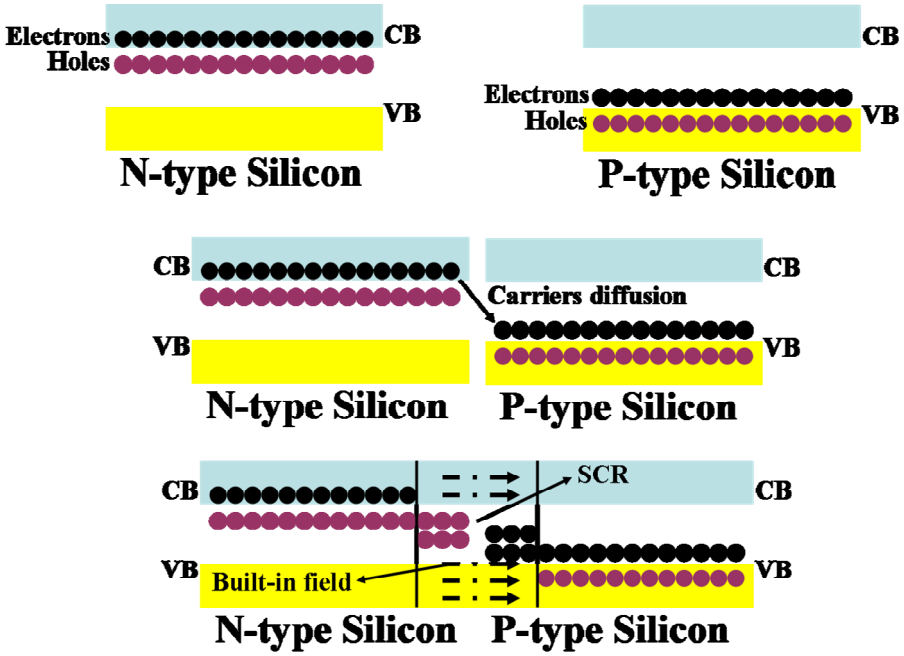


Figure 1.3. The schematic illustration of the P-N junction

One important application in semiconductors is “p-n junction”,[10–15] which is the elementary unit of devices in electronic technology. It is defined as the boundary surface of a p-type and an n-type semiconductor. As mentioned above, in p-type semiconductor, hole is the majority while in n-type one, hole becomes the minority. When a p-type semiconductor contacts with an n-type semiconductor, at their interface, the concentration gradient of carriers will change, resulting in a diffusion of carriers (holes in p-type; electrons in n-type). The electrons will flow into p-type region from n-region, but for holes, it in the opposite. Electrons from n-region diffuse into p-region, filling with the holes; only positive charges remain in n-region.

Simultaneously, holes from p-region also diffuse into n-region, combining with electrons; and leaving negative charges in p-region. During above process, majorities are depleted and a built-in field will be created to balance the diffusion effect at their interface in a direction from n- to p-region. The region at their interface called “Surface Charge Region” (SCR) or “Depletion Layer” which is shown in Figure 1.3.

When an electric potential is applied to p-n junction, assume that the potential in p-side is higher than that in n-side, the electrons in n-side and holes in p-side will be pushed into p-n junction. That can decrease the width of the p-n junction, resulting in a weaker built-in field, which can not suppress the diffusion effect from the majorities. This phenomenon is equivalent to that the electrical resistivity of the SCR region becomes lower. The electrons from n side can pass through the SCR and diffuse into the neutral region. As a consequence, the p-n junction is conductive. In reverse applied potential, the potential in p-side is lower than that in n-side, it will increase the difficulty to pass through the SCR region. In this case, it is considered as a kind of insulator. So, the unique unilateral conductivity of p-n junction makes it widely applied to diode and logic gate.

From the end of last century, energy crisis and related environment problems have become more and more noticeable and the requirement to develop “sustainable green energy sources” has become increasingly urgent. Solar energy is considered as a sustainable energy source without extra environment-harmful effects. For effective use of the solar energy, some semiconductors are designed as “solar cells”.[16–26] As

mentioned above, the energy of band gap of semiconductor usually is between 1.0 ~ 3.0 eV, which corresponding to light wavelengths in the range of 413~1240 nm. This range is also the main energy contribution in the solar emission spectra. It is well known that the electrons in the valence band can be excited to the conduction band, becoming free electrons by absorbing the external energy. This process can be expressed as: if the band gap energy is E_b, an electron in the valence band absorbs a photon with energy of E_a ($E_a \geq E_b$), the electron will be excited to conduction band. As the electron in the conduction band is not stable, finally, it will fall back to the valence band, releasing the energy by light emitting or heat etc. While, if the free electrons in the conduction band can be accumulated before they fall back to valence band, they can be accumulated and used for electric power supply. To make it realistic, semiconductors with suitable band gap structures are chosen as the solar cell.

Recently, optoelectronics has attracted more and more attentions.[27 – 33] Optoelectronic devices are electrical-to-optical or optical-to-electrical transducers, or instruments that use such devices in their operation. Optoelectronics such as photodiodes, phototransistors, and light-emitting diodes are based on the band gap transition effect of photons on electronic materials, especially semiconductors.[34–42] Some applications of optoelectronics have been widely used in our daily life.

As introduced, Si is a conventional semiconductor material with band gap energy of 1.12 eV (1100 nm). The widely use of Si in microelectronics makes it to be one of the most commonly used materials in the world. Concurrently, the suitable band gap

also spread its applications for solar cells (single crystalline Si, amorphous Si and polycrystalline Si solar cells). Thus, many efforts have been devoted to research the Si related phenomena due to the excellent native properties along with the abounded reserve and cheap price.

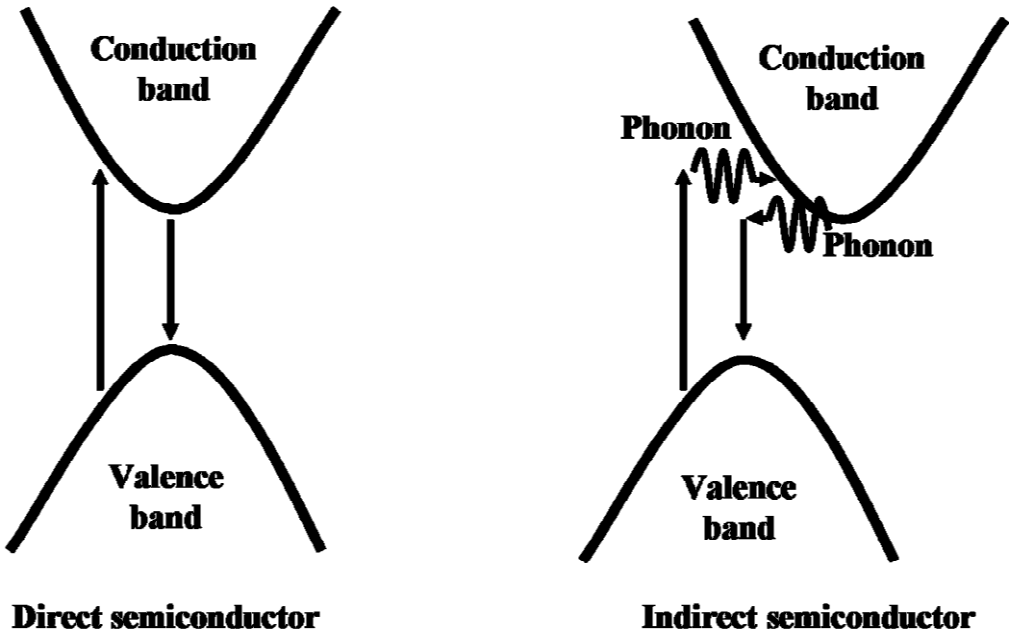


Figure 1.4. The schematic of the band to band transition difference between direct and indirect semiconductors

However, in optoelectronics, Si is not a good choice. First, its surface reflectance is too high, most of the energy from the incident light will be lost by reflection; second, Si belongs to a group of indirect semiconductors. For an indirect semiconductor, in the band gap structure, the momentum vectors (k-vector) of the minimal energy state in the conduction band and maximal energy state in the valence

band are different. That means the band to band transition needs a help from phonon to meet the momentum conservation condition (Figure 1.4). As a result, the excited electrons will stay at the conduction band for a long time and most of the excited electrons will transfer the energy to the adjacent structure in the form of heat. This phenomenon usually results in a poor performance in light-emitting compares with that from direct semiconductor.

In order to extend the application fields of Si, many methods have been tried to improve the optical absorption and fluorescence emission. One convenient way to achieve this purpose is “Surface Modification”. After surface modification, some intrinsic properties of Si such as reflectance, band gap etc, are changed due to the newly formed surface morphology.[43–47] However, there are some problems hindering the practical applications of surface modified Si. So, the study presents in this dissertation focuses on the functionalization of surface modified Si.

1.2 Introduction of surface modified Si

1.2.1 Surface modified Si prepared by anodization

In order to modify the surface structure of Si, in general, the most commonly used preparation method is electrochemical anodization.[48] As the prepared samples by this method always show a porous surface structure, the obtained sample was

called “Porous Silicon”. Porous Si was first discovered by accident in 1956. It was found that under electrochemical conditions, a crude product in the form of thick black, red or brown films were formed on the surface of the Si in stead of the expected polished surface. At that time, the findings were not taken any further study and were only mentioned in technical notes. Although porous Si had been discovered in 1950s, it did not attract considerable scientific attentions until in 1990s. When strong visible fluorescent emission was observed from porous Si by A. G. Cullis and L. T. Canham,[48] scientific community realized that Si-based optoelectronic devices became possible and the related researches about porous Si have become more and more popular.[49,50]

The synthesis of porous Si by electrochemical anodization usually uses a hydrofluoric acid (HF) or oxidant containing electrolyte. The commonly used electrolytes can be categorized into three main classes: HF-H_2O system, HF-organic system and oxidant system.[51–53]

- The composition of electrolytes contains HF-H_2O is the most commonly used anodized solution for preparation of porous Si. It does not mean that only HF and H_2O in the reaction electrolyte, but also some reagents *e.g.* ethanol or ammonium fluoride are added to help change the pH value, reduce the surface tension or for specific designs. The concentration of HF in the electrolyte can adjust the final result like the size of the pore, length of the porous layer, and growth direction. In most case, the concentration of the

HF is in the range of 40% ~ 50%.

- The electrolytes insist of pure organic solvent (DMF, DMSO) and HF is another kind of anodization solution.

- The electrolytes insist of oxidants (HNO_3 or H_2O_2). In this case, HF is not included. Because the oxides formed on the surface and can not be dissolved, so the anodization voltage usually is no a constant.

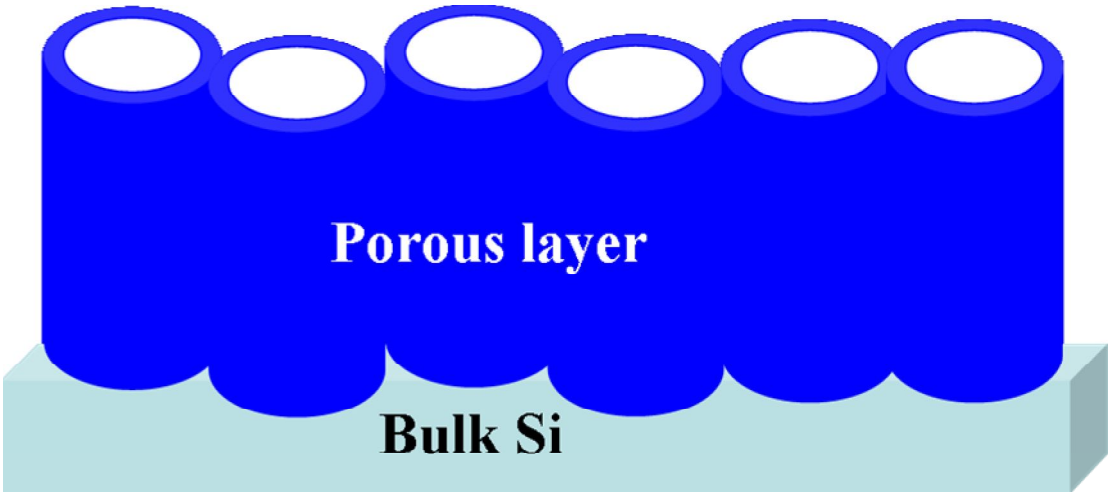


Figure 1.5. Traditional surface morphology of the electrochemically anodized sample

So far, the detailed formation mechanism is not clearly explained, but, a model about SCR has been widely accepted by scientific community.[54] The contact of the Si and electrolyte is same as the contact of p-n junction. As the Fermi levels of Si and electrolyte are different, the diffusion of carriers happens at their interface, so, a SCR will form at Si/electrolyte interface. With the help from the current, holes will move to

SCR region and these holes can accelerate the oxidation of the outermost Si layer. However, the oxidation of the outermost layer is not homogeneous, which arises from the non-ideal plane. The Si wafer contains some pits on the surface, if the end of the pit is very sharp, the sharp region will accumulate more holes than the planar area. So, the corrosion speed at the sharp regions is faster than that of other areas. At last, the surface formed the porous structure. The traditional surface morphology of the electrochemically anodized sample is shown in Figure 1.5.

1.2.2 Surface modified Si prepared by metal assisted corrosion

Metal assisted corrosion is another common way to acquire the surface modified Si.[55–57] Usually, after metal assisted corrossion, Si surface will appear in form of nanowires (NWs). Metal assisted chemical corrosion is an uncomplicated and low-cost method for fabricating various Si nanostructures with different parameters (*e.g.*, cross-sectional lateral morphology, diameter and length of the wires, growth orientation). Almost all preparation procedures can be accomplished in a chemical laboratory without expensive equipment. Thus, beside electrochemical corrosion, metal assisted corrosion method also attracts much increasing attentions.

In a metal-assisted corrosion process, usually, first the Si substrate is partly covered by a noble metal, and then it is etched by an etchant composed of HF and an

oxidative agent (H_2O_2). In general, the Si region beneath the noble metal is etched much faster than the Si region without noble metal coverage. As a consequence, the noble metal sinks into the Si substrate, generating pores or Si wires. The detailed morphologies of the finally obtained Si structures depend mostly on the initial structure of the noble metal coverage conditions. In this case, the metal usually comes from silver nitrate and the oxidant is hydrogen peroxide.[46]

In this method, the oxidation and dissolution of Si is very important. Same as the electrochemical anodization condition, the contact of the Si wafer and solution will form a SCR. Under electrochemical anodization, the holes can inject into SCR by electric potential driven while in metal assisted case, the holes originate from the oxidant. So, the directional transfer of the holes is a key factor for influencing the finally formed morphology. And the noble metal plays a role in cathode on which the reduction process of oxidant happens.

Based on above described procedures, the whole corrosion process can be summarized as followings.[46] (1) The oxidant is preferentially reduced at the interface of the noble metal/Si due to the catalytic activity of the noble metal on the reduction of the oxidant. (2) The holes are released due to the reduction of the oxidant and diffuse and pass through the noble metal injecting into the specific Si substrate region that is in contact with the noble metal. (3) The Si is oxidized by the injected holes and dissolved at the Si/metal interface by HF. The HF and the reacted byproducts diffuse along the interface between the Si and the noble metal. (4) The concentration of holes

has its maximum at the Si/metal interface. Therefore, the Si that is in contact with the metal is etched much faster by HF than a bare Si surface without metal coverage would be. (5) The holes diffuse from the Si under the noble metal to non-metal areas or to the side wall of the pore if the rate of holes consumption at the Si/metal interface is smaller than the rate of holes injection. The obtained sample always showed nanowire morphology. So, the metal assisted corroded sample is a good complementary structure for the electrochemical prepared one.

1.2.3 Other methods for preparation of surface modified Si

Except for above mentioned two methods, for some special purposes, there are some other methods to synthesize the surface modified Si. Template etching,[58] laser etching[59] and ion etching[60] also mentioned in literatures. Template assisted etching can obtain a high regular surface structure with various controllable parameters. The obtained samples have been studied for new photovoltaic devices. Laser and ion etching usually use together. With the high energy of the laser, under the sulfur hexafluoride and oxygen mixed environment, the surface of Si will be etched by F^- ions and form nanowires which are similar with the sample synthesis by metal assisted corrosion. Various surface modified Si structures with changed characteristics has been reported, *e.g.* surface modified Si showed strong visible fluorescence emission, antireflection, photovoltaic etc. In next section, the novel characteristics of

the surface modified Si will be discussed.

1.3 Novel characteristics of the surface modified Si

1.3.1 The fluorescence properties of surface modified Si

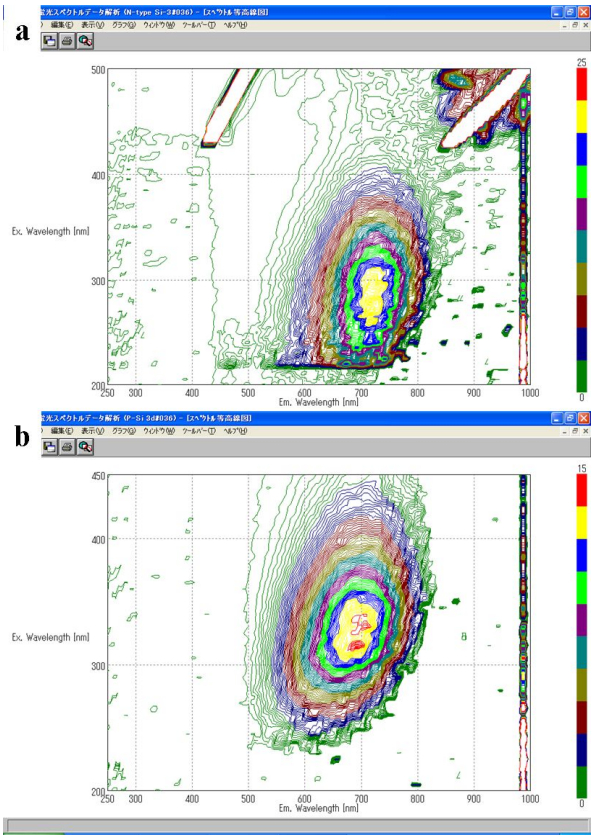


Figure 1.6. PL spectra of the surface modified silicon (a) PL from p-type surface modified Si under excitation wavelength of 260 nm; (b): PL from n-type surface modified Si under excitation wavelength of 320 nm)

One unexpected phenomenon from the surface modified Si is strong visible photoluminescence (PL) emission.[61,62] Figure 1.6 shows the PL spectra of typical surface modified Si prepared by electrochemical anodization, PL bands at red zone are observed from different kinds of samples.

Because Si is an indirect semiconductor with band gap energy of 1.12 eV, it is not a good choice for light-emitting applications. However, this unexpected strong PL has not been exactly explained so far. It is considered that the modified surface structure plays a key role in the visible emission.[63,64] In this explanation, the improved PL is attributed to surface nanostructures that lead to quantum confinement effect. With the size of a specific matter decreases to several nanometers (less than De Broglie wavelength of electron), the motion of the electrons will be restrained. As a result, the electric, thermal, optical properties change significantly. For example, the band gap, the continuous band structure in bulk will change into separated quantum states in nanoscale. This effect widens the band gap of nanosized silicon more than that of the bulk one, resulting in a blue shift of PL band from near infrared to visible range. Simultaneously, as the continuous band structure is replaced by a quantum discrete level, momentum conservation becomes possible that can significantly improve the PL efficiency. Moreover, defects at the surface form new energy levels in the band gap, capturing the excited electrons, which also contributes the PL.[65–70] For surface modified Si, the most common defect is oxygen defect. In the presence of these oxygen defect levels in the extended band gap, excited electrons may first fall into a defect level by a non-radiative process and then transit to another defect level

together with PL emitting. Theoretically, although the defect related emission has a longer lifetime compared to that of the direct band to band transition, in some cases, the PL from defect energy levels is very efficient, and sometimes, is the main PL source.

So far, according to change the parameters of surface modified Si such as the size of nanoparticle, porosity and so on; various PL emissions from ultra-violet to near infrared were obtained. The PL band of surface modified Si changes its position to low frequency direction regularly as the size of nanoparticle increases. This change is in accordance with quantum confinement effect, *i.e.*, the smaller the particle size, the larger the band gap energy.

The improved PL emission opens a new window for Si-based optoelectronics. An optoelectronic device is required to emit, induce, process, response light efficiently. However, bulk Si is difficulty in meeting these requirements. Surface modified Si may be a possible candidate for the strong PL emission. Current optoelectronic materials are some direct band gap semiconductors, such as GaAs, InAs etc, whereas, they can not integrate directly with microelectronics. So, Si-based optoelectronics provide a promising way to integrate optoelectronic and microelectronic.

1.3.2 Other optical properties of surface modified Si

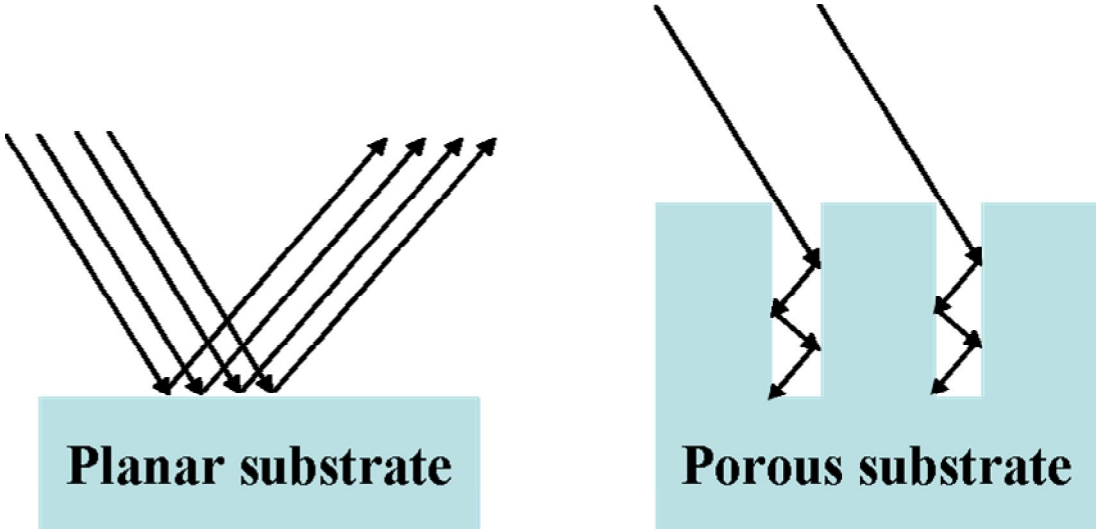


Figure 1.7. The comparison of surface reflectance between planar and porous substrate

Another obvious change of surface modified Si compared to the bulk one is optical parameters. As the porous structure formed on the surface, in some case, the incident light can reflect many times among the surface morphology (Figure 1.7). As a result, surface reflectance decrease very significantly.[71] Also, the specific surface area becomes larger due to the porous structure. These phenomena open a new window for Si based energy conversion and storage materials. Also, multi-reflection among the surface structure can make light absorption concentrates at surface region and enhances the electromagnetic emission from the surface field.

Based on above mentioned novel characteristics, in comparison with the bulk one, there are several potential advantages in surface modified Si for optical application. First, the optical loss is reduced by the surface texture. Generally, the

incident light is expressed by the sum of reflection light, absorption light and transmission light. Since the transmission light can be ignored for thick solid samples, decreased reflectance indicates the increase of absorption. This phenomenon arises from the multi-reflection among the surface structures. As a consequence, most of the incident light is absorbed by the material. Second, the band gap of surface modified Si is tunable, which can be used for optimizing the absorption of laser radiation or sunlight for various conditions. Moreover, the extended wide band gap makes it to be a possible layer material in a heterojunction structure or functionalizes the front/back surface field in a diffused junction cell. Third, the lattice mismatch may be relaxed because of the porous layers.[72] III-nitrate materials and Si directly combination can not obtain an ideal result for both electronic and optical applications due to the lattice and thermal mismatch. However, the porous transition layers between III-nitrate materials and Si is an effective way to reduce the effect of the mismatch due to the three dimensional stress reliefs.[73]

Besides above mentioned advantages, another merit is the emission enhancement in the surface field area. Surface field presents very commonly at the interface of two materials due to the different Fermi levels and electromagnetic emission from surface field is an important emission source for some specific radiations, for example, terahertz emission.[74] For the materials such as Si, Ge, they show a long penetration depth for the incident light in the range of near infrared. That means the photon-generated carriers distribution region is very large. In other word, few of the photon-generated carriers will locate at the surface field region, results in an

inefficient emission from the surface field. But, if the planar surface is replaced by a porous one, the multi-reflection among the porous structure can reduce the penetration depth that enhances the surface field emission efficiency.

1.4 The problems of surface modified Si and the corresponding solutions

1.4.1 The problems of surface modified Si

Although the surface modified Si shows various improved properties compared to bulk Si, for practical application, it still needs to overcome some disadvantages. The typical surface modified Si prepared by electrochemical anodization shows a porous structure with several tens of micrometers in height. For practical application, it requires some intermediate metal layers to control and adjust the electronic property. However, conventional porous morphology is not suitable for forming homogeneous layers structure on the surface. So, pillar or column-structured surface may solve this problem. However, the conventional preparation method of pillar or column-surface modified Si requires a template fabricating process, for example, specific patterns writing by photolithographic template or metal/organic self-assemble. The partly template covered sample then is immersed in a HF containing solution or environment to obtain the pillar/column surface. But, after the corrosion, the photolithographic

template or the self-assembled metal/organic impurities need to be removed from the surface. In the removal process, it will destruct the structure and original states of the surface. So, it is necessary to develop a method to obtain the regular pillar/column surface structure without using any template.

For the fluorescence emission, two main problems for practical application of the surface modified Si are its instability and low quantum yield, especially the low stability (not only the PL intensity decreases rapidly under ambient conditions, but also the position of maximum PL wavelength changes over time), which limits the application of surface modified Si as an optoelectronic candidate.[75 – 79] The mechanism of this PL degradation is still unclear. A plausible reason is the atmospheric oxidation of the modified surface, that is, the size of nano silicon and luminescent defects become smaller and less.

In most cases, for the PL from surface modified Si, the nanosized Si nanoparticles are the main luminescent centers and mostly, the outermost layer is passivated by hydrogen, hydroxyl or organic groups. However, after aging treatment in ambient air, the Si–H, Si–OH or Si–CH_x bonds are replaced by Si–O–Si bond. Simultaneously, surface Si nanoparticles are oxidized, decreasing the size. As a result, the number of luminescent centers becomes less and the remaining luminescent centers become smaller (as mentioned in quantum confinement effect, the smaller the particles, the larger the band gap energy). In fluorescent spectrum, the most immediate effect of this change is degradation of PL intensity and blue shift of the PL

peak position.

In other cases, oxygen defects (SiO_x $x < 2$) are the main reason for the visible PL emission. In this model, as the Si does not oxidize very completely, so, some oxygen defects present in the form of spatial vacancies, i.e., oxygen defects at the nanosized Si surface can form defect levels in the extended band gap. Under this situation, these oxygen defects are the main reason for PL emission. Same as the luminescent centers of nanoparticles, the number of oxygen defects also becomes less as the exposure time in ambient air increases, resulting in the degradation of PL visible emission. In general, because the unsaturated oxide state of Si is much unstable than Si nanoparticles, the fluorescent emission will degrade faster in oxygen-defect model.

Another disadvantage of using Si in fluorescence emission is the single PL emission. Now, the white-light-emitting materials are hot research areas in light-emitting field, so full-color PL from surface modified Si has attracted considerable attentions. So far, except some fluorescent materials like rare earth elements, and ZnO,[80] very few reports focus on other materials. As mentioned above that the practical applications requires the metal transition layers to control and adjust the electronic action of surface modified Si, so, if a common used metal and surface modified Si composite can emit white light, it will be very convenient to combine with actual applications. Some metallic materials like nano Cu nanoparticles, Cu_2O etc. show efficient blue emission and surface modified Si usually emits a red-orange PL. That is to say, the mixture of these two lights can produce white light in potential.

However, Cu element directly combines with surface modified Si always show a single PL emission band because the presence of Cu ions will disrupt the band to band transition in the band gap of surface modified Si.[81,82] As a result, the original PL from surface modified Si become very weak. Not only Cu ions, some other metals like Ag, Au also show the same PL quenching result.

The disadvantages of surface modified Si mentioned above are the major obstacles for practical applications (porous surface and instability of PL behavior) or limit the surface modified Si apply to some commonly used applications (single PL emission). In order to functionalize the surface modified Si, in next section, some possible solutions will be discussed.

1.4.2 The possible solutions for the weaknesses of surface modified Si

In order to obtain the pillar-structured Si (PSi) without using template, although electrochemical anodization is not considered as a good choice, if the electrolyte contains appropriate oxidant, electrochemical anodization may become a possible way to obtain the expected result. As the oxidant can transfer the holes to form Si oxides on the surface, before the anodization starts, corrosion of Si wafer has started along with the preferential direction.

In order to improve the PL behaviors, some possible solutions have been

proposed. One method is surface passivation of freshly prepared surface modified Si. For example, carbon or nitrogen reacts with fresh surface modified Si at high temperatures under vacuum environment, forming stable Si–C or Si–N bonds on the outermost layer of surface modified Si to prevent the inner luminescent centers from heavy oxidation. An alternative method is metal-ion doping in solutions at room temperature. Recently, the deposition of metal/metal oxide on surface modified Si has attracted attention and the combination of metal and surface modified Si makes Si-based applications more realistic.

Although the oxidation is the main reason for the PL degradation, if the outermost layer can be oxidized very fast and the inner structure still keep its original state, the stable oxidized layers can prevent the inner structure from atmospheric oxidation. This method is called “fast oxidation”.

So far, many efforts have been devoted to improving the PL from freshly prepared surface modified Si. However, Most of the previous methods need a high temperature environment. As the porous structure has a strong adsorption for molecules, under high temperature environment, the adsorbed molecules can react with surface modified Si, influencing the PL of the obtained sample. So, if a room temperature treatment method can be developed, that may avoid the problem of the reaction between the impurities and surface modified Si.

For the full-range PL emission, as the presence of Cu ions will disrupt the band to band transition in the band gap of surface modified Si, if the distribution areas of

Cu ions and native PL centers of surface modified Si are different, the mutual disturbance may be avoided. In other words, the dual/multi PL from metal/surface modified Si may become realistic.

So, the purpose of this thesis focuses on the functionalization of the surface modified Si, including the column surface preparation, PL stability enhancement, dual PL emission as well as the improved electromagnetic radiation from surface field area.

1.5. Content of this thesis

In this thesis, the anodized corrosion behaviors of surface modified Si, the optical properties of surface modified Si and the surface treated surface modified Si are reported. In total, there are four chapters below.

- Chapter 2 is the preparation methods of surface modified Si. In this chapter, two methods were carried out to synthesis the surface modified Si both in P and N type Si. Different with the common results reported before, the surface morphology of the prepared samples by electrochemical anodization shows a regular pillar structure. Formation mechanisms for all prepared samples are explained in this chapter.

- Chapter 3 is the fluorescence properties of the prepared samples. The influence of Cu coating on photoluminescence behaviors is presented. Fluorescence spectra from the HF-treated aged surface modified Si covered by a thin Cu composite (Cu-PSi, P type) and anodized SiCu nano-island composite (N type) are characterized in this chapter. Stable photoluminescence was acquired from Cu coated p-type surface modified Si with aging and HF etching treatments; dual photoluminescence emission at blue and red ranges were observed from SiO_x/Cu_xO nanocomposite.

- Chapter 4 is the influence of the regular columnar surface modified Si on far infrared radiation behaviors from the metal/semiconductor nano thin film. A Cu and Au nano thin film composite structure is analyzed by both deposited on the planar Si and columnar substrate.

- Chapter 5 is the summary of whole research, includes the contributions and future perspectives of my study presented in this dissertation.

Chapter 2. Preparation and Characterization of Surface Modified Silicon

2.1: Preparation and characterization of p-type surface modified Si by electrochemical anodization

2.1.1 Experimental method for p-type surface modified Si

The P-type surface modified Si was prepared by electrochemical method. The preparation device is shown in Figure 2.1. A B-doped <111> oriented Si wafer (Nilaco, Japan) with a doping concentration of approximately 1×10^{19} cm^{-3} was used as the working electrode. Pt was used as the cathode. First, the Si wafers were washed with acetone and ethanol by ultrasonic oscillation for 5 min. The cleaned wafers were placed in a solution of aqueous hydrofluoric acid (HF, 5%) for 1 min to remove the surface oxide impurities. Then, the wafers were rinsed again with purified water. The electrolyte (with a total volume of 26.5 mL) comprised ferric nitrate (0.04 M, Junsei, Japan), hydrofluoric acid (HF, 46%, Stella Chemifa, Japan), and purified water (Organo/ELGA, >18 MΩ). The volume ratio of HF and purified water was 7:5. The current density was set to 100 mA cm^{-2} and maintained for 50 min at room temperature.

The obtained samples were characterized by JEOL JSM-6510LA scanning electron microscope (SEM) and a Hitachi H-9500 transmission electron microscope (TEM, 300 kV). The surface properties were analyzed using a JEOL JPS-9200 X-ray photoelectron spectrometer (XPS) equipped with a monochromatic Mg Kα source

operating at 100 W under ultrahigh vacuum (~1.0 × 10^{-7} Pa) condition; the obtained spectra were calibrated to a C 1s peak. Surface reflectance spectra were measured using a Shimadzu UV-3100 spectrophotometer. Photoluminescence spectra were captured using a Jasco FP-6600 spectrofluorometer.

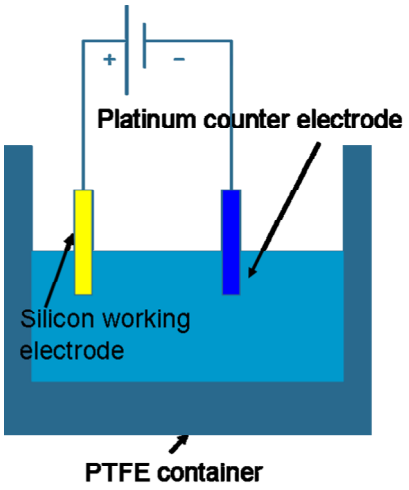


Figure 2.1. The diagram of the experimental device

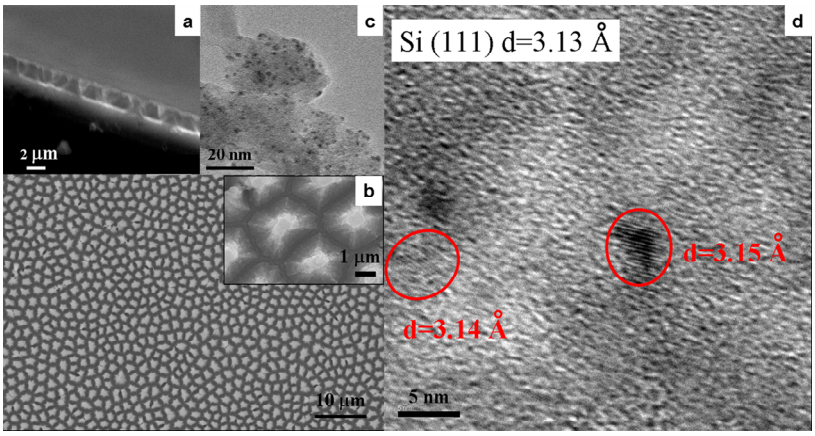


Fig. 2.2. (a) Lateral view of the surface morphology of as-prepared p type surface modified Si; (b) SEM top view image of the as-prepared p type surface modified Si. Insert: magnified top view image of as-prepared p type surface modified Si; (c) TEM image of the surface of the prepared sample, the black dots observed in the image are Si nanoparticles; (d) HR-TEM image of surface morphology. Lattice fringes with distances of 3.14 and 3.15 Å can be observed in the black dots. The distances correspond to Si (111) (3.13 Å).

2.1.2 Surface structure of the prepared p-type surface modified Si

The surface morphology of the as-prepared p type surface modified Si is shown in Figures 2.2a and 2.2b. Compared to the conventional porous structure, the prepared sample shows regular pillar-structured surface morphology (for convenient, use PSi to stand for pillar-structured silicon below). The pyramid-shaped pillars with a diameter of 1 μm and height of 2 μm were observed on the surface. The fine structure of the pyramid-shaped pillar was observed by TEM, as shown in Figure 2.2c. Many nanoparticles (black dots) with the size in the range 0.9–5.0 nm were embedded on the side walls. The high-resolution TEM image in Figure 2.2d shows that the surface contained many isolated Si crystals surrounded by amorphous silicon oxides, as shown by the fringes observed in the black dots (ca. 3.1 Å, corresponding to Si(111)). These results indicate that the surface of the as-prepared PSi was composed of numerous pyramid-shaped pillars containing considerable nanosized Si crystals on their side wall surfaces.

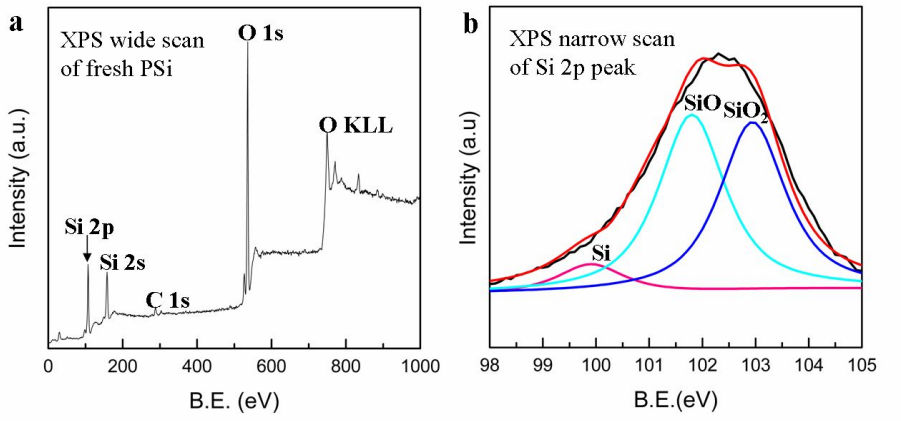


Figure 2.3. (a) Wide X-ray photoelectron spectrum (XPS) of freshly prepared pillar-structured silicon (PSi); (b) Narrow XPS scan of Si 2p peak of the freshly prepared PSi.

XPS analysis provides information about the chemical composition of the surface of PSi as shown in Figure 2.3. From Figure 2.3a, the XPS wide scan confirmed that only Si, O and C on the surface (H can not be detected by XPS, even though, it may exist on the surface). The Si 2p peak can be deconvoluted into three peaks (Si, SiO and SiO_2) in the spectrum of freshly prepared PSi as shown in Figure 2.3b. The unsaturated oxygen state (SiO) indicates the presence of oxygen defects on the surface. It is well known that oxygen defects in the form of SiO_x ($x < 2$) play the same role as luminescence centers.

2.1.3 Photoluminescence and reflectance properties of p-type surface modified Si

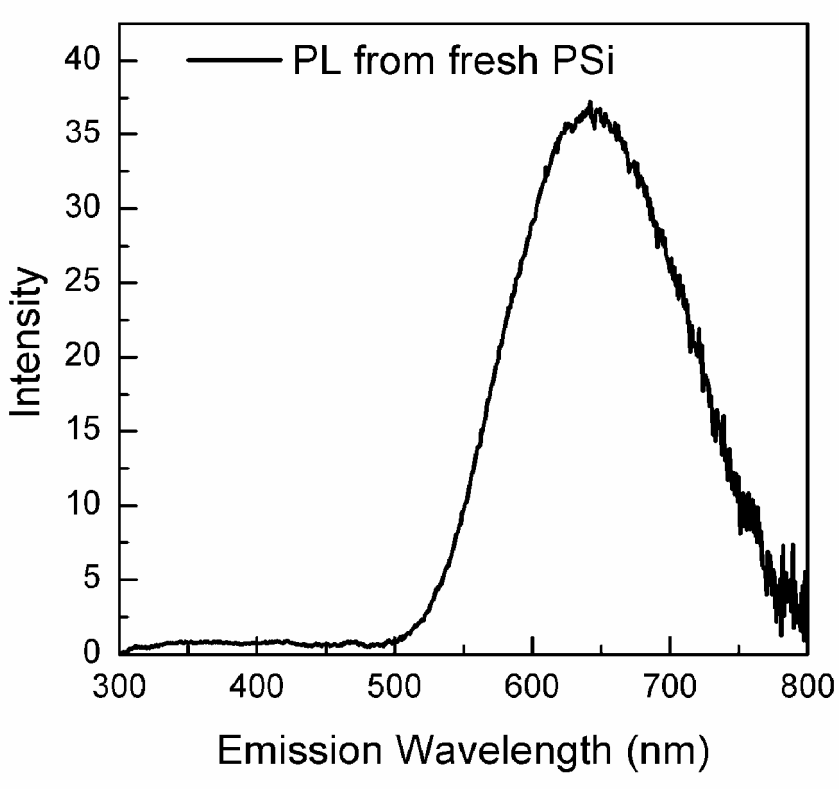


Figure 2.4. Photoluminescence spectrum of freshly prepared PSi (excitation wavelength = 260 nm).

The PL spectrum of the freshly prepared PSi under the excitation wavelength of 260 nm is shown in Fig. 2.4. Compared to the insignificant PL from the bulk silicon (1.12 eV), PSi showed a strong and wide blue-shifted peak at 667 nm (1.85 eV). This PL is usually derived from the quantum confinement effect for nanosized Si crystals (as observed in the TEM image of Figure 2.2d). Under quantum confinement conditions (for example: Si with the size <4.3 nm), the most significant change is that the band gap became wider than that of the bulk and these Si nanocrystals divide the continuous conduction and valence bands into isolated energy levels. Moreover, from XPS scan result shown in Figure 2.3b, the unsaturated oxygen state (SiO) was observed on the surface and the presence of SiO is a kind of oxygen defect type on the surface of Si. Thus, in this case, both silicon nanostructures and oxygen defects (the interface of Si nanoparticle/SiO_x) affect the PL of PSi. So, for PSi, when an electron is excited, three transition paths can be considered: (1) nonradiative centers; (2) recombination with holes; and (3) capture by interface oxygen defects. The latter two models resulted in PL phenomena.

The optical reflectance spectra of the Si samples were measured, as shown in Figure 2.5, to support the PL results. Figure 2.5 shows the surface reflectance spectra of PSi and planar Si. The surface reflectance of PSi decreased to 5% compared to that value (~50%) of planar Si. This decrease in surface reflectance can be attributed to multi-reflection among surface columns. As mentioned in introduction part, the incident light is expressed by the sum of reflection light, absorption light and transmission light. Since the transmission light can be ignored for thick solid samples, decreased reflectance indicates the increase of absorption. As a consequence, most of the incident light is absorbed by the material. This result also demonstrated that

optical loss, which is a very important index for the optical properties of Si, decreased.

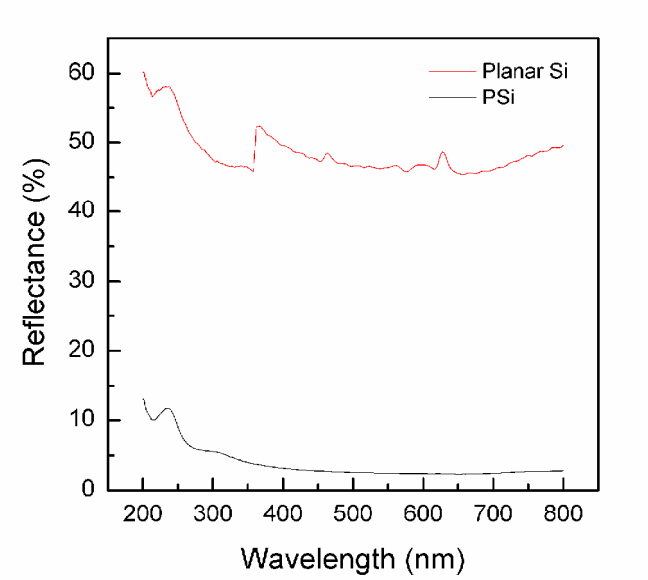


Figure 2.5. Surface reflectance spectra of planar Si (red) and freshly prepared PSi (black).

However, the aging test (see Fig. 2.6) indicates that the PL intensity decreased rapidly when the sample was placed under ambient air conditions. Only 25% of the PL intensity remained after one week and almost disappeared after one month (see Fig. S1). The degradation of PL is a major obstacle for practical optoelectronic applications of PSi. The formation of SiO_2 on the surface may be the reason for this degradation. XPS spectra also indicate this phenomenon (see Fig. 2.7). Si was oxidized with the increase in aging time, and the Si^{2+} peak became weak. Only the Si^{4+} peak was enhanced. These results strongly confirm that the amount of the PL cores of nanocrystal Si and oxygen defect sites decreased due to oxidation, indicating that SiO_x ($x < 2$) became SiO_2.

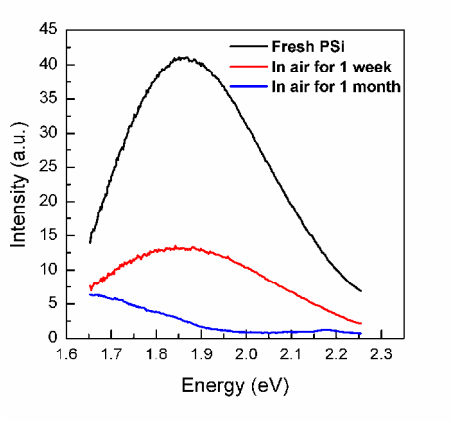


Fig. 2.6. Photoluminescence spectra of as-prepared PSi at different periods after preparation (The sample was kept under ambient air conditions).

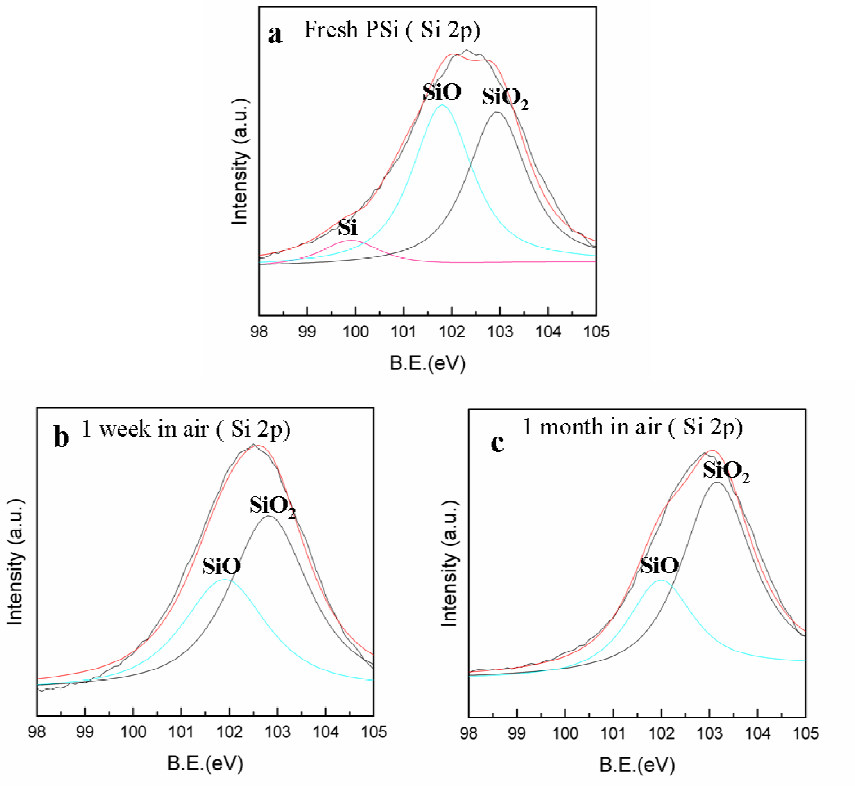


Fig. 2.7. Narrow X-ray photospectra of Si 2p of freshly prepared PSi sample (a), sample kept under ambient conditions for one week (b), and one month (c).

In this section, the surface modified p-type Si was prepared by electrochemical anodization. The pillar surface was successfully synthesized by using a HF/$Fe(NO_3)_3$ solution as the electrolyte. Both the fluorescence emission and optical absorption properties are improved. However, the PL from PSi is unstable, *e.g.* after one month stored in air, PL intensity decreased very rapidly.

2.2: Preparation and characterization of n-type surface modified Si by electrochemical anodization

2.2.1 Experimental method for n-type surface modified Si

The preparation method of the surface modified n-type Si is similar to that of the p-type one. The phosphorus-doped, <111> oriented silicon wafer (Nilaco, Japan) with a electric resistivity less than 0.02 Ωcm was washed with ethanol and acetone by ultrasonic oscillation for 5 min, and then it was rinsed again with purified water. Then, the cleaned Si wafer was anodized in an electrolyte consisting of ferric nitrate (0.008 mol dm^{-3}, Junsei, Japan), hydrofluoric acid (46 %, Stella Chemifa, Japan), and purified water (volume ratio, HF: H_2O = 7: 5 (v/v)) with a 100 mA cm^{-2} current density for 1 h. The obtained sample was washed by purified water and dried in air at room temperature.

The obtained samples were characterized by JEOL JSM-6510LA scanning electron microscope (SEM) and a Hitachi H-9500 transmission electron microscope (TEM, 300 kV). The surface properties were analyzed using a JEOL JPS-9200 X-ray

photoelectron spectrometer (XPS) equipped with a monochromatic Mg Kα source operating at 100 W under ultrahigh vacuum (~1.0×10^{-7} Pa) condition; the obtained spectra were calibrated to a C 1s peak. Photoluminescence spectra were captured using a Jasco FP-6600 spectrofluorometer.

2.2.2 Surface structure of the prepared n-type surface modified Si

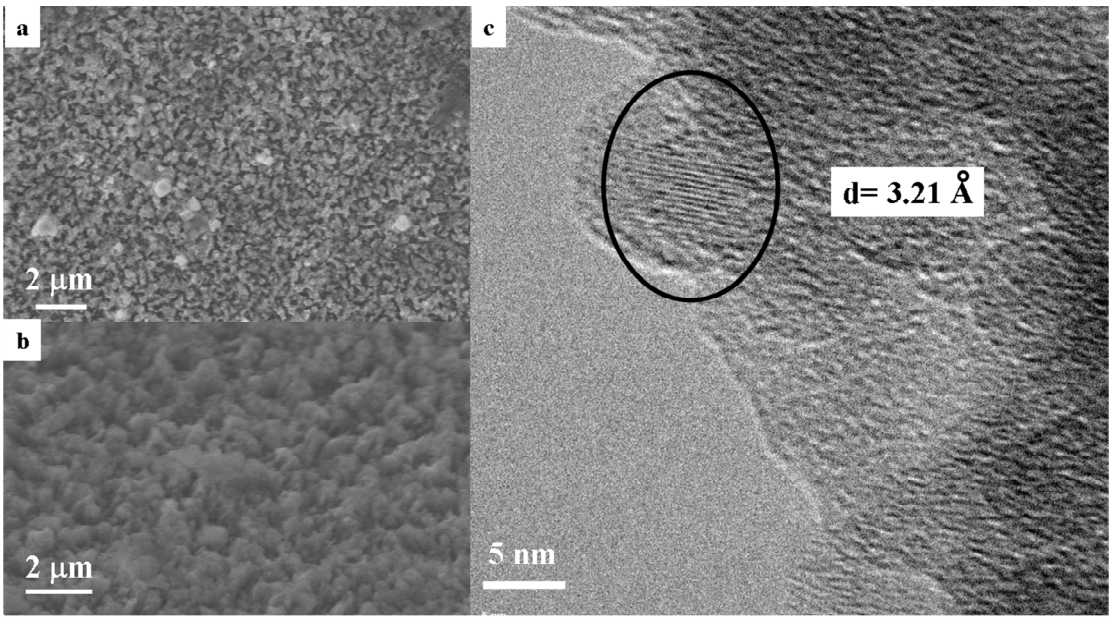


Figure 2.8. (a) Top view of the SEM image of the electrochemical anodized n-type Si; (b) SEM image of the electrochemical anodized n-type Si with 53° tilted; (c) HR-TEM image of the surface structure of n-type PSi, the measured interplanar distance of 3.15 Å corresponds to the Si (111) plane (3.21 Å).

Figure 2.8 shows the surface morphology of the prepared n-type PSi. Pillar structure also formed on the surface as shown in Figure 2.8a and 2.8b. Compared to the surface structure of p-type PSi, the size of the pillar on the surface of n-type PSi became smaller: several hundreds nanometers in diameter and height. Moreover, from

HR-TEM image shown in Figure 2.8c, Si nanoparticles were observed on the surface too and the lattice fringes with distance of 3.21 Å corresponds to distorted Si (111) (3.13 Å). That indicates the n-type PSi has a similar surface fine structure that the isolated Si crystals surrounded by amorphous silicon oxides.

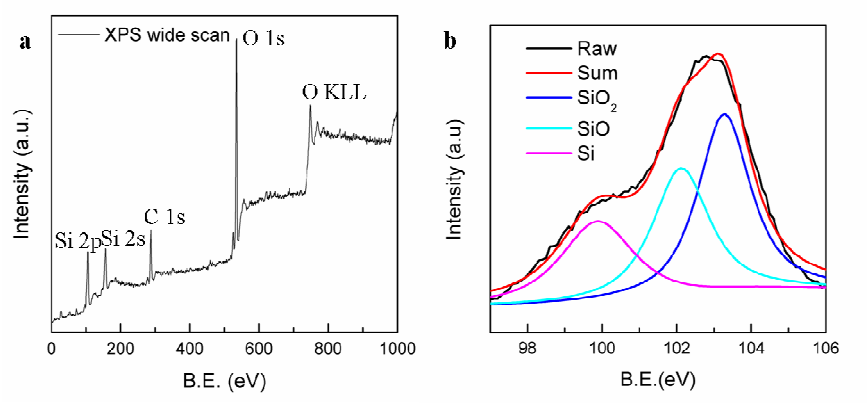


Figure 2.9. (a) Wide XPS scan of freshly prepared n-type PSi; (b) Narrow XPS scan of Si 2p peak of the freshly prepared n-type PSi.

2.2.3 Photoluminescence and properties of n-type surface modified Si

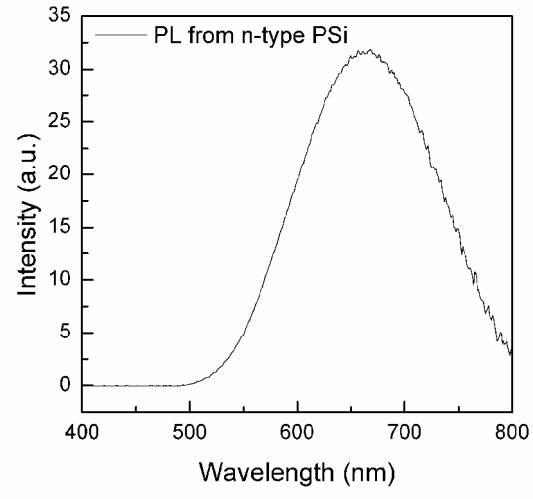


Figure 2.10. PL spectrum of freshly prepared n-type PSi (excitation wavelength = 320 nm).

XPS spectra data provide the surface composition information of the n-type PSi as shown in Figure 2.9. Surface composition elements are same as the p-type PSi. Si, O, C and possible H present on the surface. Narrow XPS scan of the Si 2p peak is shown in Figure 2.9b. After fitted, three peaks at 99.8 eV, 101.8 eV and 103.3 eV which correspond to Si, SiO and SiO_2, respectively. Compared to the p-type PSi, the Si content on the surface was increased due to the low concentration of Fe^{3+} in the electrolyte.

PL spectrum from the freshly prepared n-type PSi is shown in Figure 2.10. The PL spectrum of the n-type PSi is similar to that of the p-type. A red PL peak at 660 nm was observed. From the HR-TEM images shown in Figure 2.8c and XPS results in Figure 2.9, the origin of the red PL can also be revealed as the Si nanoparticles and oxygen defects which had been described in p-type PSi. For PSi (no matter p or n-type), when an electron is excited, the consequent recombination process with holes and interface oxygen defects results in the PL emission.

2.2.4 Formation mechanism of p and n-type surface modified Si

Formation mechanism of the p and n-type PSi is illustrated in Fig. 2.11. In my case, anodization electrolyte is different from the commonly used HF/ethanol solution. It was composed of HF and ferric nitrate. Ferric nitrate is an oxidant which can oxidize the surface of Si wafer before the electric potential is applied. Fe^{3+} transits its holes to Si, partly oxidizing the Si wafer. In this process, Fe^{3+} was reduced to Fe, and Si became SiO_2. The newly formed Fe and SiO_2 are finally dissolved by HF, leaves a pit on surface. After the potential was applied, the pit has a sharp point tip which can accumulate more carriers (holes) than the planar regions. As a result, the corrosion

rate of the sharp point tip is faster that that of the planar area. At last, Si surface will form a regular pillar structure. Because p-type Si wafer contains more holes than n-type one, corrosion in p-type Si wafer will along the deep pit, and the influence of shallow pit can be ignored. However, in n-type Si wafer, hole is the minority. Influences from deep and shallow pits on surface morphology are nearly equal, which makes the size of the pillar on p-type Si is larger that that on n-type one. The total corrosion process can be expressed as below:

$$Si + 4F^- + 2H^+ + 2h^+ = SiF_4 + H_2 \qquad 2.1$$

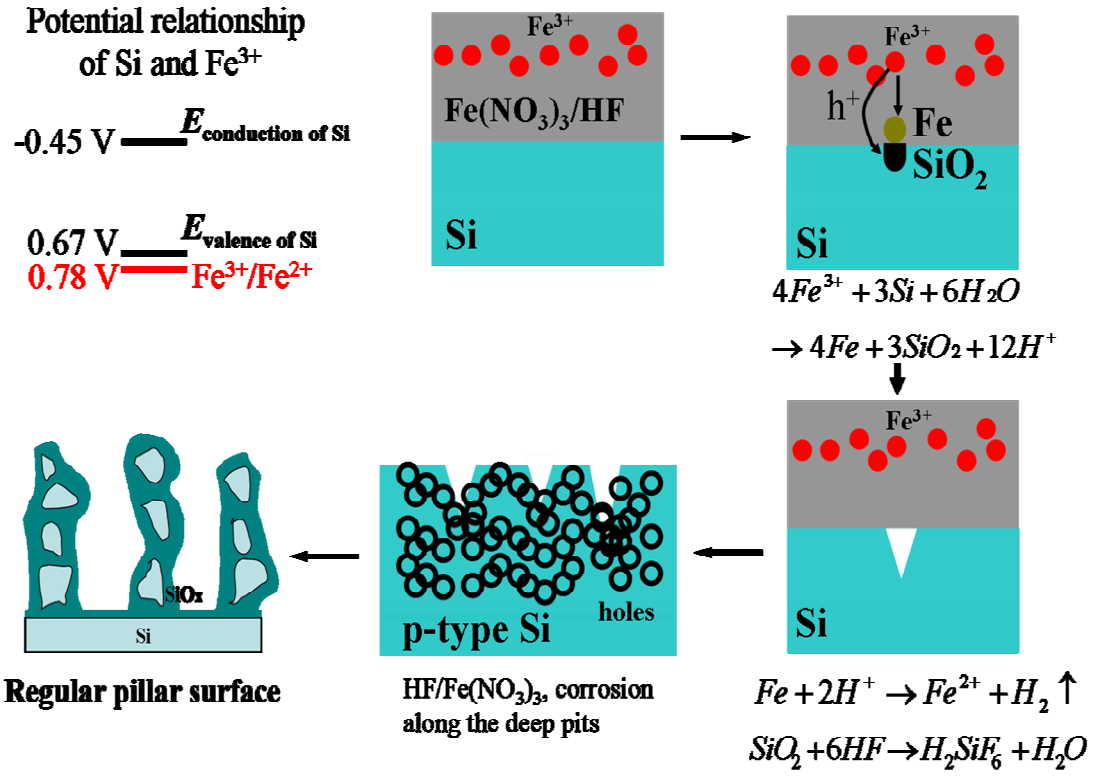


Fig. 2.11. Schematic illustration of the formation process of the prepared PSi.

In preparation process, concentration of ferric nitrate, anodization duration, and

current density are three major parameters for pillar-surface formation. As mentioned above, the role of ferric nitrate is that makes the corrosion rate different at different areas (pit region and planar region) to form regular pillar surface morphology. If the concentration of ferric nitrate is too few, formation of pit on surface will be restricted. In that case, corrosion will start at the vacant sites in the lattice structure of Si, resulting in a random porous structure instead of the regular pillar one. To the contrary, if ferric nitrate is redundant, it can oxidize all surface area of Si wafer rather than partly-oxidation. For this, the following electrochemical anodization will show a homogeneous corrosion at all surface area. As a consequence, there is no special structure formed on Si surface. Anodization duration plays a similar role. It is reasonable to assume that less anodized duration will cause a low corrosion degree; while, collapse of the pillar will happen if the duration is prolonged. Besides these two, current density can also influence surface morphology. Current density means the concentration of hole in the anodized area. Corrosion speed will increase by following the increase of current density. Note that if current density is too high, electropolish phenomenon will replace the specific-structure formation. So, for regular pillar-surface structure, conditions in section 2.1.1 and 2.2.1 are optimum.

2.3: Preparation and characterization of n-type surface modified Si by metal assisted method

2.3.1 Experimental method for Ag-assisted n-type surface modified Si

Beside electrochemical anodization, another common used method is metal assisted corrosion. As for a comparative sample, an n-type surface modified Si was

synthesized by silver assisted method. A phosphorus-doped <111> oriented Si wafer with a doping concentration of approximately 1×10^{19} cm^{-3} was used. First, the Si wafers were washed with acetone and ethanol by ultrasonic oscillation for 5 min. The cleaned wafers were placed in a solution of aqueous hydrofluoric acid (HF, 5%) for 1 min to remove the surface oxide impurities. Then, the wafers were rinsed again with purified water. Next, immersed this cleaned silicon wafer in silver nitrate ($AgNO_3$)/HF solution for 1 min at room temperature to deposit silver particles on Si wafer. The concentration of HF and silver nitrate were 4.6 mol/L and 0.01 mol/L, respectively. At last, transferred the silver coated Si wafer in a HF/H_2O_2 aqueous solution and kept the silver-deposited Si wafer in HF/H_2O_2 solution for 30 min at 60℃. Concentration of the HF and H_2O_2 were 5.0 mol/L and 0.2 mol/L, respectively.

The obtained samples were characterized by JEOL JSM-6510LA SEM. The surface properties were analyzed using a JEOL JPS-9200 X-ray photoelectron spectrometer (XPS) equipped with a monochromatic Mg Kα source operating at 100 W under ultrahigh vacuum (~1.0×10^{-7} Pa) condition; the obtained spectra were calibrated to a C 1s peak. Photoluminescence spectra were captured using a Jasco FP-6600 spectrofluorometer.

2.3.2 Surface structure and photoluminescence properties of Ag-assisted surface modified Si

Surface morphology of the prepared Ag-assisted surface modified silicon is shown in Fig. 2.12. Pillar structure formed on the surface and the diameter of the pillar was about 3–5 μm with 30 μm in height. Unlike the PSi prepared by electrochemical anodization, the distribution of these pillars was irregular and the growth direction of the column was also non-uniform. Simultaneously, very pillar

contains many thin Si nanowires (Fig. 2.12d).

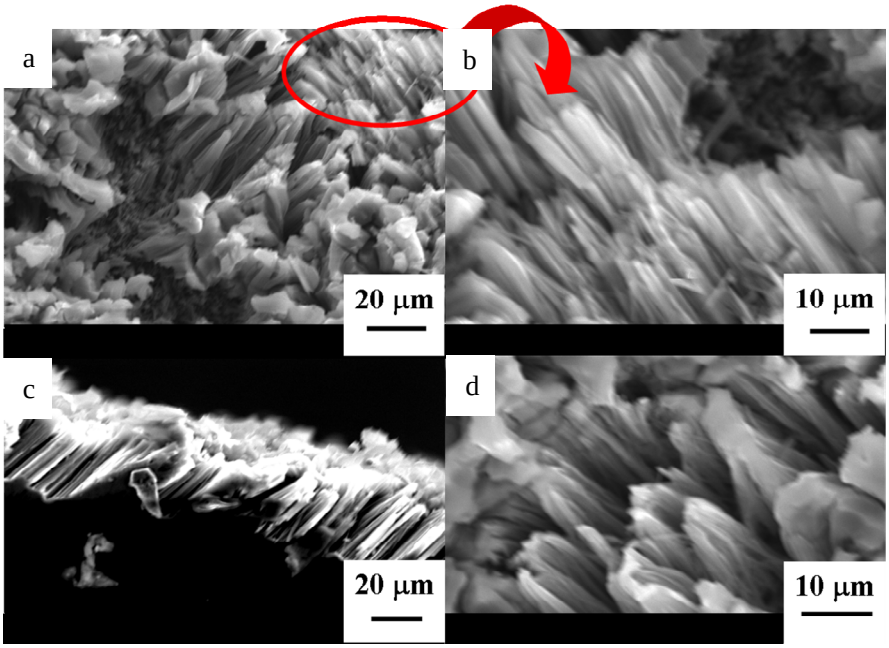


Fig. 2.12. Surface morphology of the Ag-assisted corroded PSi.

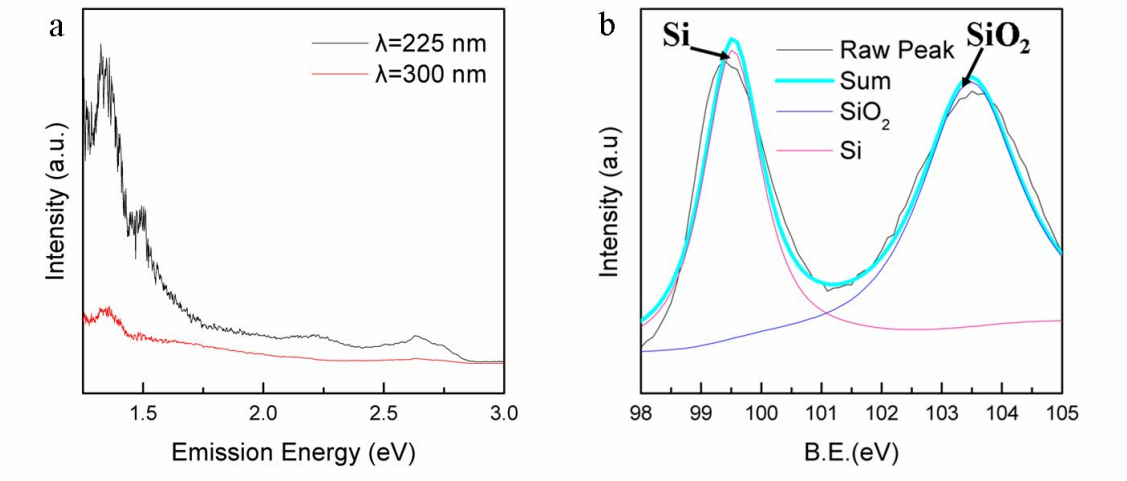


Fig. 2.13. (a) PL spectra of the Ag-assisted PSi under different excitation wavelengths; (b) XPS spectra of the Si 2p peak of the the Ag-assisted PSi.

The PL emission properties of the Ag-assisted PSi showed different fluorescence zone compared to that from the electrochemical anodized PSi as shown in Fig. 2.13a. The red PL emission from electrochemical anodized PSi was replaced by a near infrared one. Surface composition is also different. An obvious change is that the unsaturated Si oxide disappeared. That means the PL center in this case has some changes, *i.e.*, the oxygen defects did not contribute any effort for the PL emission and the origin of the PL only arose from the Si nanoparticles.

Same as the formation mechanism mentioned in section 1.2.2, the oxidation and dissolution of Si is very important. The contact of the Si wafer and aqueous solution formed a SCR. The directional transfer of the holes from the oxidant is a key factor for influencing the finally formed morphology. And the noble metal played a role in cathode on which the reduction process of oxidant happens. Holes originate from the Ag^+ were transferred to Si bulk and the Ag^+ ions were reduced into Ag. Concurrently, Si beneath the reduced Ag was oxidized into Si^{4+}. The reduction of Ag^+ was preferentially happened at the surface of Si bulk and the holes were released and passed through the Ag clusters, injecting into the Si bulk which was in contact with the Ag. As a consequence, the oxidized Si was dissolved by HF, finally, the surface structure that shown in Fig. 2.12 formed.

In this chapter, the surface modified Si was prepared by electrochemical anodization and silver assisted corrosion. The columnar surface was successfully synthesized by using a $HF/Fe(NO_3)_3$ solution as the electrolyte for both p and n-type Si. The fluorescence behavior and optical absorption properties are improved. The silver assisted corroded sample also showed a columnar surface and a near infrared

PL emission. Different with the sample prepared by electrochemical anodization, the unsaturated oxygen state (SiO) did not present on the surface. However, for all samples, the PL was unstable, *i.e.* after one month stored in air, PL intensity decreased very rapidly.

Chapter 3. The Influence of Cu Coating on Photoluminescence Behaviors from the Surface Modified Silicon Prepared by Electrochemical Anodization

3.1: The influence of Cu coating on fluorescent properties from hydrofluoric acid treated aged surface modified silicon

3.1.1 Introduction

As mentioned in Chapter 1, one big problem of PSi for practical application is the unstable PL. Not only the PL intensity decreases rapidly under ambient conditions, but also the position of maximum PL wavelength changes over time. The mechanism of this PL degradation is still unclear. A plausible reason is the atmospheric oxidation of the surface, i.e., the size of nano silicon and luminescent defects become smaller and less. The surface of fresh prepared PSi terminated with Si dangling bonds was passivated by hydrogen (Si–H), oxygen (Si–O), or other elements or groups (Si–CH_x), and finally, SiO_2 dominates the surface. In order to improve the PL properties, previous studies recommended that the surface passivation of fresh PSi can solve the instability problem. For example, carbon or nitrogen reacts with fresh PSi at high temperatures envrironment, forming stable Si–C or Si–N bonds on the outermost layer of PSi that prevent the inner luminescent centers from heavy oxidation. An alternative method is metal-ion or organic doping in solutions at room temperature. However, most of the mentioned methods need a high temperature environment, and as the porous structure has a strong adsorption for molecules, under high temperature environment, the adsorbed molecules can react with porous Si, influences the PL of the obtained sample.

So far, very few studies focused on the efficient PL from PSi treated under room temperature condition because some methods use room temperature treatment always show a poor PL performance. In this section, a PL improvement was obtained by coating a Cu layer onto the HF treated aged PSi at room temperature. The mechanism of the enhanced PL of Cu-PSi was elucidated. Surface chemical states of PSi contained substantial amounts of unsaturated silicon sub-oxide (SiO), the unstable SiO combined with the sputtered Cu, forming new Cu related defects. The Cu related defects along with surface nanostructures enhanced the PL.

3.1.2 Experimental method for Cu-PSi

The Cu-PSi was prepared by electrochemical and magnetron sputtering method. The preparation method of PSi was same as the P-type surface modified Si. A B-doped <111> oriented Si wafer (Nilaco, Japan) with a doping concentration of approximately 1×10^{19} cm^{-3} was used as the working electrode. Pt was used as the cathode. First, the Si wafers were washed with acetone and ethanol by ultrasonic oscillation for 5 min. The cleaned wafers were placed in a solution of aqueous hydrofluoric acid (HF, 5%) for 1 min to remove the surface oxide impurities. Then, the wafers were rinsed again with purified water. The electrolyte (with a total volume of 26.5 mL) comprised ferric nitrate (0.04 M, Junsei, Japan), hydrofluoric acid (HF, 46%, Stella Chemifa, Japan), and purified water (Organo/ELGA, >18 MΩ). The volume ratio of HF and purified water was 7:5. The current density was set to 100 mA cm^{-2} and maintained for 50 min at room temperature.

Cu thin films were deposited on PSi surfaces by magnetron sputtering. Before the sputtering, the prepared aged (2 months in air) PSi was immersed in 5% HF solution for 5 s to remove the over-oxidized SiO_2 layers and was dried by nitrogen

flow. Then, it was quickly placed in a vacuum chamber (the pressure was less than 5.0 × 10^{-3} Pa), and the distance between the sample and sputtering target was ca. 60 mm with 30 mA and 230 V sputtering current and voltage, respectively. The sputtering time was set to 1–3 min under 20 °C.

A JEM-2010 transmission electron microscope (TEM, 300 kV) was used to observe the interface structure. The surface properties were analyzed using a JEOL JPS-9200 X-ray photoelectron spectrometer (XPS) equipped with a monochromatic Mg Kα source operating at 100 W under ultrahigh vacuum (~1.0 × 10^{-7} Pa) condition; the obtained spectra were calibrated to a C 1s peak. PL was measured using a Jasco FP-6600 spectrofluorimeter, and a JEOL JIB-4600F/HDK multibeam system was used to process the FIB sample. Surface reflectance spectra were measured using a Shimadzu UV-3100 spectrophotometer. Fourier transform infrared (FTIR) spectra were recorded using a Shimadzu IRAffinity-1 spectrophotometer in the range 400–4000 cm^{-1}.

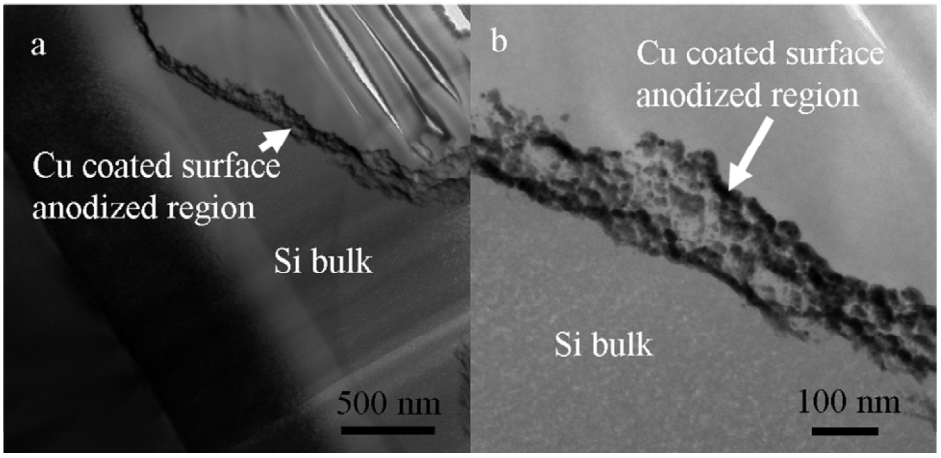


Fig. 3.1. TEM lateral image of the Cu-PSi, the sputtering time of Cu was 1 min. (b) Enlarged lateral image of the Cu-PSi. (Cu-PSi, PSi was aged in air for 2 months before sputtering). The sputtering time of Cu was 1 min. The sample was prepared using FIB (JEOL JPS-9200 X-ray photoelectron spectrometer) with a thickness of 100 nm

3.1.3 Surface structure of Cu-coated HF-treated aged PSi

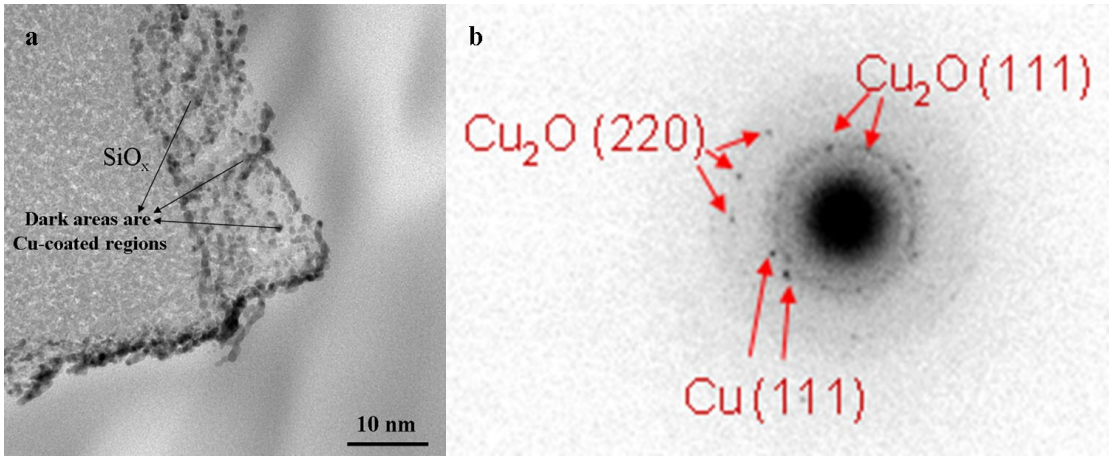


Fig. 3.2. (a) Further magnified cross-sectional TEM image of Cu-PSi; (b) Selected area electron diffraction pattern of Cu-PSi (The diffraction area is the same as the area shown in Fig. 3.2a)

Lateral interface structure of the Cu-PSi is shown in Fig. 3.1. The boundary of the bulk Si and anodized Si layer is very clear and the thickness of the anodized Si layer is about 100 nm. As the deposited Cu can only distributed on the anodized layer and compare to Si or SiO_x, the number of the transmitted electron is less, the dark area on the anodized layer is the Cu element. It is notable that the thickness of the Cu layer is not homogeneous, *e.g.* some anodized regions covered by Cu while some areas still exposed to ambient air. The reason for this phenomenon is surface tension.[83] As the silicon surface is not an ideal surface, when a thin layer of Cu (usually less than 20 nm) is deposited on the surface for a short period of time, it cannot form a continuous film by surface tension influence (In my case, the sputtered rate of Cu was estimated of about 3.5 nm/min).

The further magnified lateral interface image and its selected area electron

diffraction (SAED) pattern are shown in Fig. 3.2. The composition of the sputtered Cu zones was in the form of Cu and Cu_2O polycrystalline. The presence of Cu^+, it is a very important factor for the PL from Cu-PSi, which will be discussed below.

3.1.4 Photoluminescence properties of Cu-coated HF-treated aged PSi

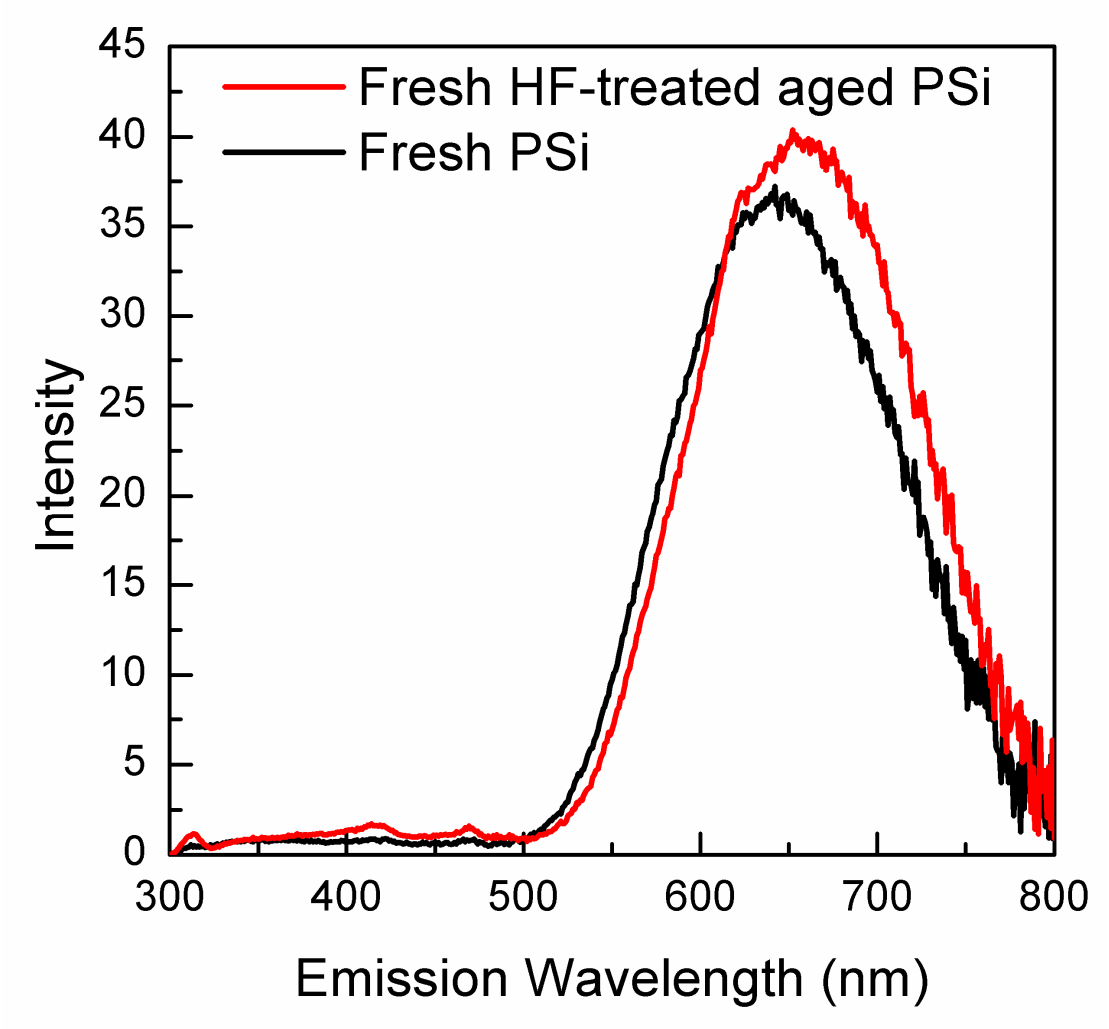


Fig. 3.3 Photoluminescence spectra of fresh porous silicon (PSi) (black) and fresh HF-treated aged (2 months in air) PSi (red). Excitation wavelength = 260 nm.

As mentioned in Fig. 2.6, the PL from PSi downgraded very rapaidly. This degradation of PL intensity is the major obstacle for practical applications of PSi. To

improve the PL behaviour, the PL-collapsed aged (2 months in air) PSi sample was immersed in 5% HF for 5 s to remove the newly formed SiO_2 thin layer on the surface. The fluorescence spectrum of the fresh HF-treated aged PSi is shown in Fig. 3.3. Under 260 nm excitation, the red peak reappeared at 670nm (the intensity of the red PL peak from fresh HF-treated aged PSi even 10% higher than that from fresh PSi) and a new weak peak observed at 415 nm. The PL results shown in Figs. 2.4, 2.7 and 3.3 reveal that the major factor for the red PL in Fig. 2.4 and 3.3 originates from the oxygen defects at the Si nanoparticle/SiO_x ($x < 2$) interface. As the exposure time of PSi in air increases, the amount of oxygen defects on the surface decreases rapidly by oxidation, and also the size of Si nanoparticles decreases by this process, thus decreasing the PL from PSi. The rate of oxidation of Si is significantly lower than that of SiO_x ($x < 2$), therefore, Si nanoparticles still exist on the surface of PL-degraded age PSi, particularly after stable SiO_2 dominated the surface, because the Si nanoparticles are surrounded by SiO_x ($x < 2$). So, some Si nanoparticles became smaller or were fully oxidized to form Si oxide and another part of the Si nanoparticles maintained their size almost no change. After the HF treatment on the aged PSi surface, the oxygen defects recovered at the surface of Si nanoparticles, resulting in the reappearance of PL in the red region (Fig. 3.3, red line). And in general, the blue shift of the newly formed deep blue PL band (415 nm) can be attributed to the following: (i) After oxidation in air, the change in the value of x in SiO_x ($x < 2$) that changes the positions of the oxygen defect energy levels in the band gap; and (ii) the decrease in the size of the Si nanoparticles by oxidation in air (the smaller the particle size, the larger the band gap).

Although the PL reappeared, this HF-treated aged PSi still very easy to oxidize. To further improve the PL behaviour, a Cu coating was applied to prevent the fresh HF-treated aged PSi surface from oxidation. The PL spectra of Cu-PSi are shown in Figs. 3.4. Figure 3.4 shows that with the change in sputtering time, a significant PL dissimilarity was detected. Compared to the freshly PSi, all the Cu-coated samples showed a clear PL band with intensity change factors in the range 0.35 – 4 in the blue zone (470 nm) with three shoulders (460nm, 485nm and 496nm) and a sub-band at ~565 nm. Among them, the 2-min Cu-coated sample had the strongest improvement (the PL spectra and relative characterization below refer to 2-min Cu-coated sample if no special explanation is provided). The enhanced PL originated from Cu diffusion and new Cu-SiO_x ($x < 2$) compound after Cu sputtering, i.e., Cu diffused into interstitial defects in the SiO_x and the unstable SiO may combine with Cu to form Cu-SiO_x ($x < 2$).[84–86] The diffused Cu and Cu-SiO_x donated new Cu-related defect sites to the Si nanoparticle/SiO_x band gap.

On the other hand, sputtering duration time influences the PL intensity very significantly. That can be attributed to the number of the Cu-SiO_x and the changed surface reflectance. The 1-min Cu coated sample has a ~3.5 nm Cu layer and in this thickness, it can not form the continuous film structure on the surface due to the surface tension, as mentioned in Fig. 3.1. As a result, the number of the Cu-related defects is less than that of the 2-min and 3-min samples. However, as the deposition time increased, the surface reflectance also increased, resulting in a higher optical loss. Composite analysis, the 2-min sample shows the best PL performance.

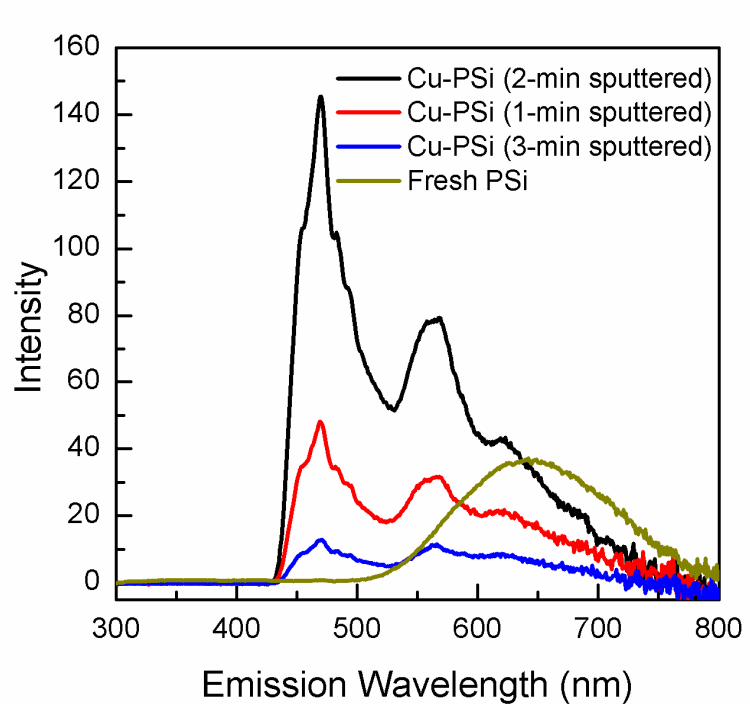


Fig. 3.4. Comparison of photoluminescence spectra of Cu-PSi samples (2 months aged in air and HF treated the surface before sputtering) under different sputtering conditions under an excitation wavelength of 260 nm.

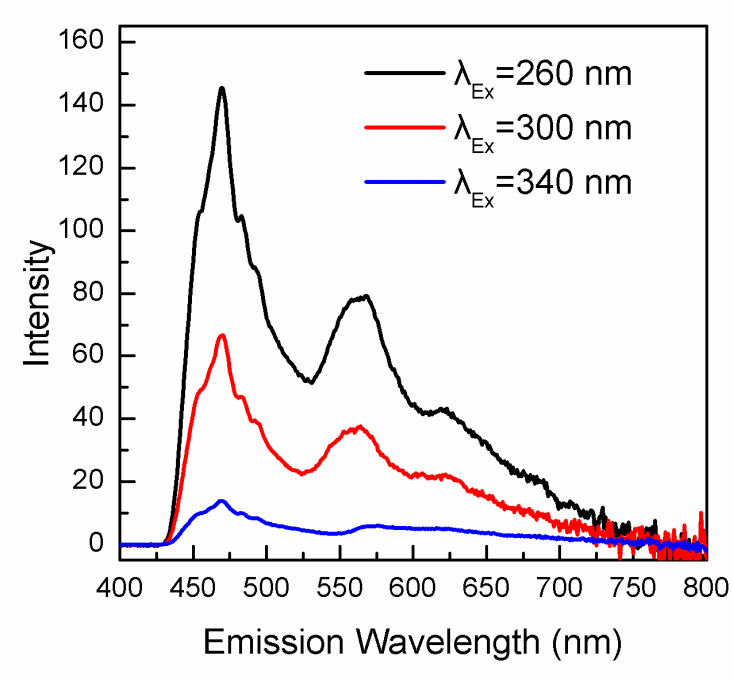


Fig. 3.5. Photoluminescence spectra of Cu-PSi with a sputtering time of 2 min (2 months aged in air and HF treated the surface before sputtering) under various excitation wavelengths.

Figure 3.5 shows the PL emission spectra under different excitation wavelengths from 260 to 340 nm. The blue peak position at 470 nm did not change, therefore, this peak originated from the new Cu-related defect sites and the three shoulders arose from the $3d^{10} \rightarrow 3d^{9}4s^{1}$ transitions of Cu^{+} as well as the intra d → d band transition of Cu^{2+} in the interstitial vacancies of Si oxides.[87,88] Because of the fixed value difference between the defect energy levels, the PL position also remains constant. However, the peak at ~565 nm changed according to the excitation wavelength. Thus, the origin of this PL at ~565 nm can be attributed to the remaining silicon or new Cu_2O, Cu nanoparticles.

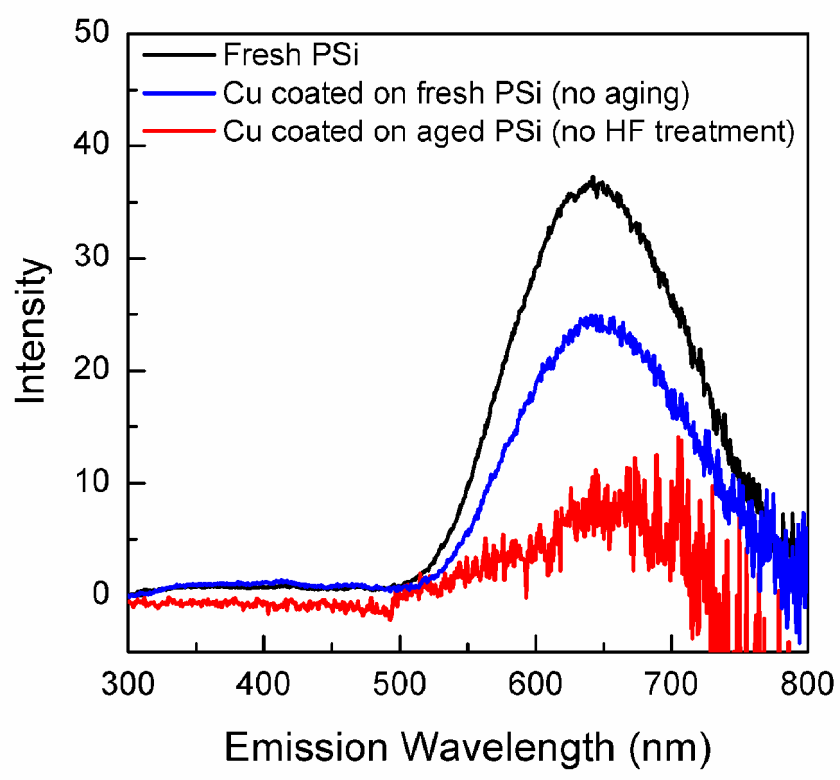


Fig. 3.6. Photoluminescence spectra of various Cu coated (2 min) PSis under different treatment conditions (black: fresh PSi; red: Cu coated PSi, PSi was freshly prepared without aging in ambient air; blue: Cu coated PSi, PSi was aged in air for 2 months without HF treatment before Cu sputtering). Excitation wavelength = 260 nm.

More PL spectra of various Cu coated porous silicon samples were measured as shown in Fig. 3.6. The PL intensity of Cu coated fresh porous silicon (red line) decreased to 65% of the original value, while the sample of Cu coated aged (2 months in air) porous silicon without HF treatment (blue line) had a collapsed PL in the red range. The results (blue and red lines) in Fig. 3.6 can be explained by the following considerations: (i) for the fresh prepared sample, the surface was passivated by –H, –OH or $–CH_x$ (H can not be detected by XPS), so the sputtered Cu can not efficiently contact the unstable SiO on the surface; (ii) for the aged one, as the SiO_2 dominated the surface state, stable SiO_2 and Cu do not react at room temperature. Simultaneously, these results also demonstrated that the Cu_2O and Cu nanoparticles in Fig. 3.2 were not the major factor for the PL. Because only Cu coated HF-treated aged porous silicon showed a PL enhancement, so only this sample will be discussed below.

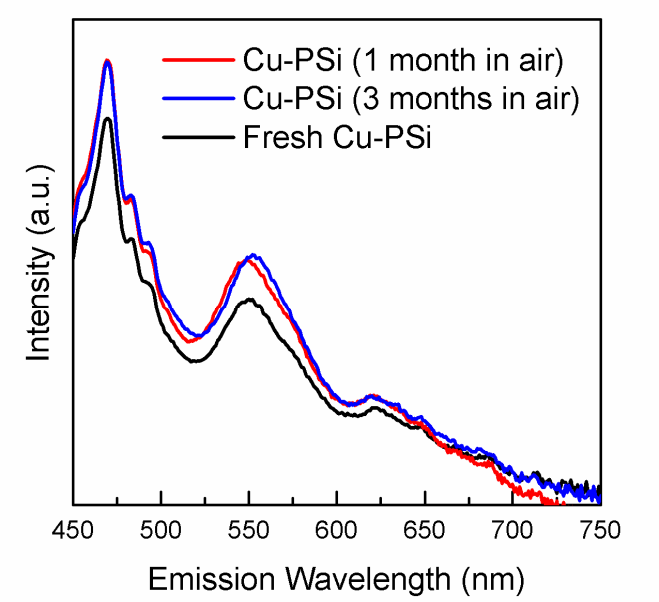


Fig. 3.7. Aging effects on the photoluminescence intensity of Cu-PSi under 2 min sputtering treatment.

The PL stability of Cu-PSi is shown in Fig. 3.7. Unlike severe degradation of fresh PSi, the PL intensity of Cu-PSi showed no significant change under ambient conditions for one month. Even after three months under ambient conditions, the PL intensity was very stable. This stability is due to the protection by the metal coating. The formed Cu-SiO_x ($x < 2$) on the surface prevents the reaction between oxygen and the inner materials. However, as the oxidation time increased, PL from Cu-PSi also degraded. In our case, Cu-PSi can keep its intensity for at least six months.

3.1.5 Characterizations of Cu-coated HF-treated aged PSi

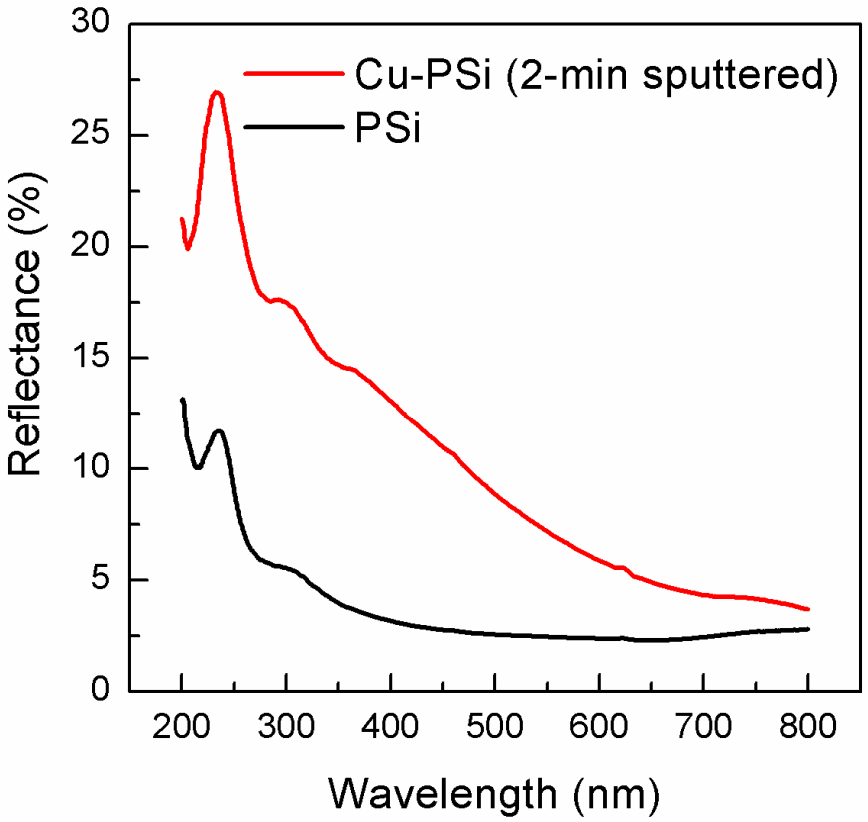


Fig. 3.8. Surface reflectance spectra of freshly prepared porous silicon (PSi, black) and Cu-coated porous silicon (Cu-PSi, red).

The optical reflectance spectra of the Si samples were measured, as shown in Fig. 3.8, to support the PL results. The surface reflectance spectra of PSi and planar Si have been shown in Fig. 2.5 and Fig. 3.8 provides the comparison between the Cu-PSi and PSi. The surface reflectance of PSi decreased to 5% compared to that value (~50%) of planar Si (Fig. 2.5, and the sharp reflectance change at around 364 nm was caused by the change of light source). This decrease in surface reflectance can be attributed to multi-reflection among surface columns. This result also demonstrated that optical loss, which is a very important index for the optical properties of Si, decreased. The reflectance curve of Cu-PSi has a similar tendency as that of PSi. In the long-wavelength range, the reflectance of Cu-PSi is almost same as that of PSi, while in the short-wavelength range, the deviation becomes very distinct, and the mean value of the reflectance of Cu-PSi is higher than that of PSi (Fig. 3.8). Despite this, the reflectance is still significantly lower than that of planar Si (Fig. 2.5). In the UV region in particular, a sudden decrease at ~250 nm indicates an optical absorption region around this area. In fact, the results of the reflectance test are also consistent with the PL spectra shown in Figs. 3.4 and 3.5.

Oxygen/metal defects under quantum confinement effect are the reasons for the PL from PSi and Cu-PSi in this study. Under quantum confinement conditions (for example: Si with the size <4.3 nm), the most significant change is that the band gap became wider than that of the bulk. In Figs. 2.2c and 2.2d show that the PSi contains Si nanocrystals in silicon oxide side walls, and these Si nanocrystals divide the continuous conduction and valence bands into isolated energy levels. After this change, the band gap became wider. For PSi, when an electron is excited, three transition paths can be considered (Fig. 3.9a, upper).

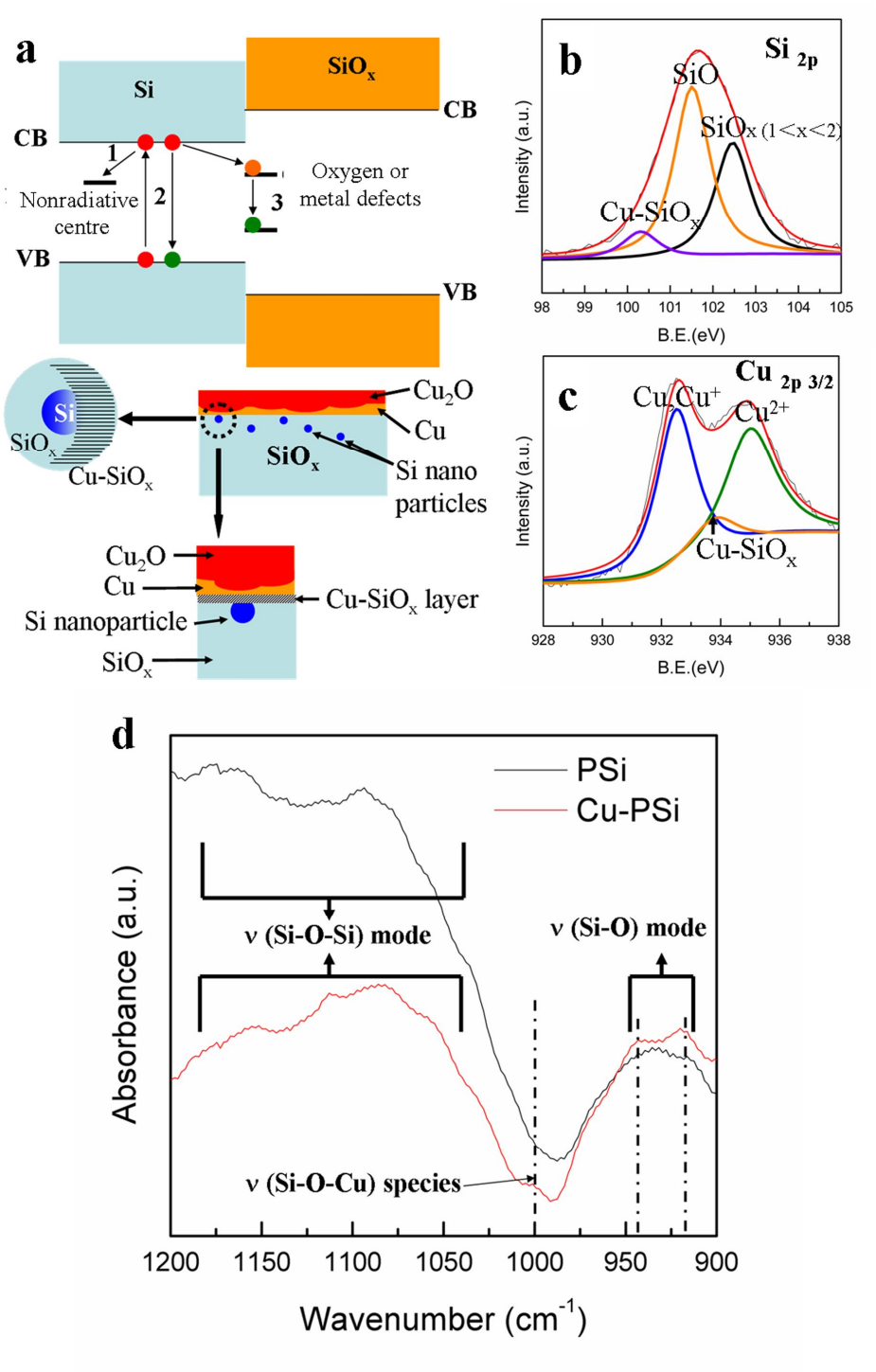


Fig. 3.9. (a) Schematic illustrations of the photoluminescence mechanism of porous silicon and Cu-PSi (upper). Surface structure model of Cu-PSi (bottom); (b) XPS result of Si 2p peak for Cu-PSi (sputtering duration: 1 min); (c) XPS result of Cu 2p peak for Cu-PSi (sputtering duration: 1 min); (d) FTIR spectra of the Cu-PSi with 1 min sputtering treatment (red) and PSi (black).

(1) nonradiative centers (mark 1), (2) recombination with holes (mark 2), and (3) capture by interface oxygen defects (mark 3). The latter two models resulted in PL phenomena. For Cu-PSi, the surface SiO film is very unstable even at room temperature, which combined with the sputtered Cu and formed a new ultra-thin compound layer. The interface structural model of Cu-PSi is shown in Fig. 3.9a (bottom). Simultaneously, such a structure (Cu-SiO_x $x < 2$) can donate new Cu related defect sites to the band gap, and this Cu related defect sites are considered as a type of PL center.[89–93] To confirm the presence of Cu-SiOx ($x < 2$), the XPS spectra of Si 2p of Cu-PSi were measured, as shown in Fig. 3.9b.

Compared with the XPS spectrum of fresh PSi (see Fig. 2.3b), the SiO (light blue line) peak was still present, and SiO_2 (black line) transformed to unsaturated silicon oxides (SiO_x, $1 < x < 2$). Moreover, a new peak (purple line) appeared at 100.4 eV and replaced the Si peak (99.7 eV). As the electronegativity of Cu is less than that of oxygen, the peak shifted to lower energy when Cu reacted with SiO. This implies that the peak at 100.4 eV arose from the Cu-SiO_x ($x < 2$) or SiO_x ($x < 1$). Moreover, the XPS of Cu $2p_{3/2}$, as shown in Fig. 3.9c, shows a peak at ~933.9 eV, a typical position of Cu and Si oxide compounds.[94] Based on these results, the peak at 100.4 eV can be assigned to Cu-SiO_x ($x < 2$). However, it is very strange that the Si peak was not observed in this XPS spectrum. The most plausible reason for this absence is the detection limit: the limit of detection of our XPS device (JEOL JPS-9200) is 0.1 at% and 2–5 nm in depth. From Fig. 2.2d and Fig. 2.3b, the surface structure of the freshly prepared PSi can be described as that the Si nanoparticles are surrounded by amorphous Si oxides (the thickness of the Si oxide layer is about 100 nm as shown in

Fig. 3.1). So, the relatively weak Si peak in the XPS spectrum shown in Fig. 2.3b comes from the Si nanoparticles in the Si oxide layer. Compared to Si oxides, even in the XPS spectrum of the freshly prepared PSi, the content of Si is very few. As the aging time increased in air, parts of the Si nanoparticles in the Si oxide layer were oxidized and its content became lower than the XPS detection limit (0.1 at%), resulting in the absence of Si peak in the XPS spectra of the aged PSi (Figs. 2.7b and 2.7c). Because the Cu-PSi was prepared by using an aged PSi substrate, the reason for the absence of Si peak in the XPS spectrum of Cu-PSi is same to the reason for the aged PSi. Another notable phenomenon is the presence of CuO in the XPS spectrum; however, CuO was absent in the diffraction pattern. This indicates that CuO existed in the amorphous form on the surface. The existence of Cu–O–Si was also confirmed by the FTIR analysis, as shown in Fig. 3.9d. Three absorption bands appeared at 930 cm^{-1}, 1070 cm^{-1}, and 1180 cm^{-1} in both the spectra, were attributed to the Si–O stretching mode, and Si–O–Si asymmetric stretching modes (the latter two), respectively.[95,96] Concurrently, compare with the curve of PSi (black line), the spectrum of Cu-PSi (red line) showed three new shoulders at 919 cm^{-1}, 945 cm^{-1} and 1002 cm^{-1}. These shoulders can be assigned to the perturbation of copper: in particular, the shoulder at 1000 cm^{-1} which has been demonstrated as Si–O–Cu stretching species in previous researches.[97,98]

3.1.6 Photoluminescence properties of Cu-coated HF-treated aged n-type PSi

Not only the p-type PSi, but also the n-type PSi can also improve its PL stability by this method. The preparation method of n-type PSi was same as the the sample prepared in Chapter 2; the conditions of Cu coating process were same as those of the

p-type sample. The PL spectra of the freshly prepared PSi and freshly prepared Cu coated n-type PSi (Cu-nPSi) are shown in Fig. 3.10. For the freshly prepared n-type PSi, it shows a red PL centered at 660 nm which is similar with the PL spectrum from p-type PSi. Same as the p-type PSi, the PL of the n-type PSi also downgraded very rapidly in ambient air (after aged in ambient air for 1 month, the PL almost disappeared). To improve the stability, same treatments as the p-type PSi was applied in this aged n-type PSi before Cu coating. The PL spectra of the Cu-nPSi shown in Fig. 3.10 indicate that a red-shift peak located at 710 nm was observed with a 78% of the intensity value of the freshly prepared n-type PSi was observed from the Cu-nPSi, which was quite different from the p-type Cu coated samples.

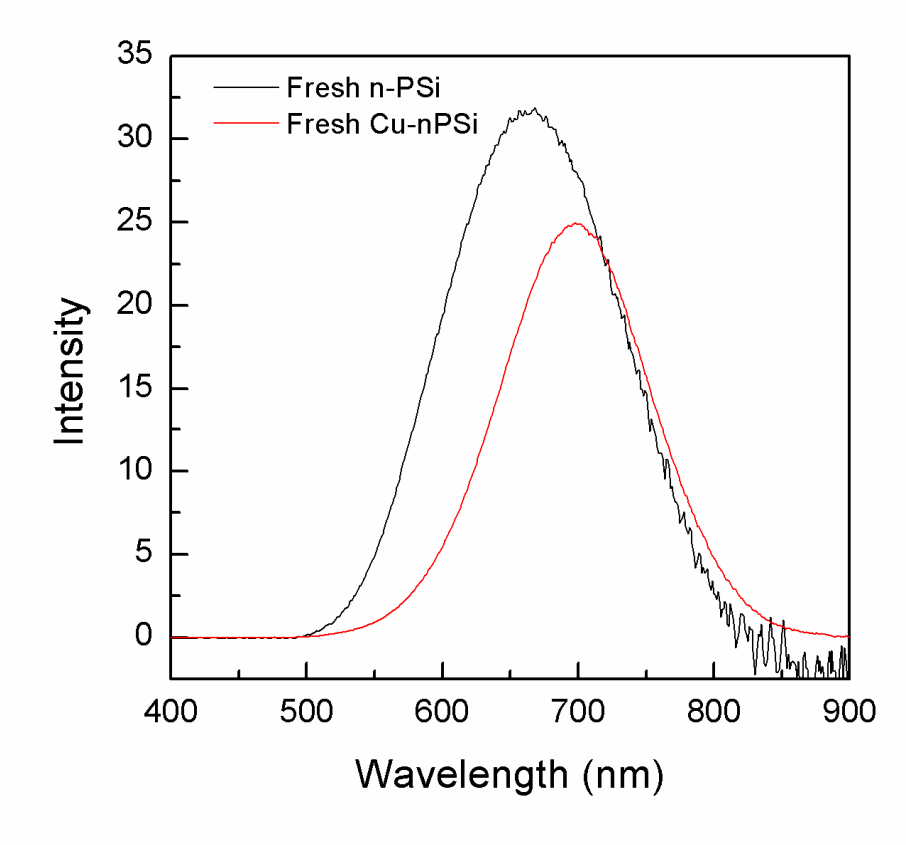


Fig. 3.10. Photoluminescence spectra of freshly prepared n-type porous silicon (n-PSi, black line) and freshly prepared Cu coated n-type PSi (Cu-nPSi, redline, aged in air for 1 month and Cu sputtering time was 2 min). Excitation wavelength = 320 nm.

The PL stability of the Cu-nPSi is shown in Fig. 3.11. After stored in ambient air for 1 month, the PL intensity of the Cu-nPSi did not change so much, although it showed a little decrease. The difference of the stability between the red peak in freshly prepared n-type PSi and Cu-nPSi confirmed that the origin of these two peaks were different. The red peaks in the spectra of freshly prepared n-type PSi and Cu-nPSi were attributed to oxygen defects and Cu related defects, respectively.

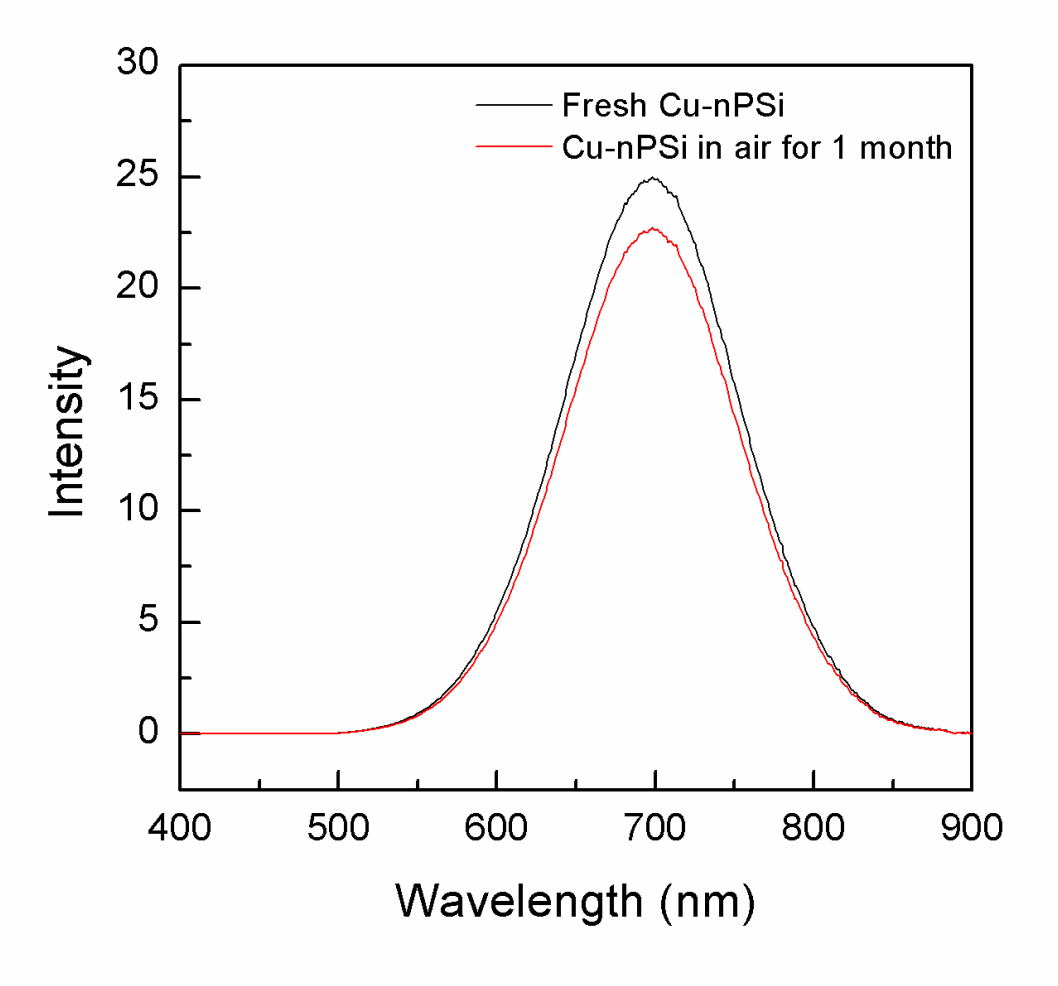


Fig. 3.11. Aging effects on the photoluminescence intensity of Cu-nPSi under 2 min sputtering treatment.

To find out the reason for the difference of the PL behaviors between n and p-type Cu coated PSi. The surface composition of n-type PSi was characterized by XPS, as shown in Fig. 3.12. One obvious difference of the XPS spectra of these two samples is the content of the Si. In previous p-type PSi, the content of Si was quite few compared to that of the Si oxides (SiO and SiO_2). However, in n-type PSi, the content of Si increased very significantly. That means the oxidation degree of the n-type PSi is lower than that of the p-type PSi. In other word, the number of the oxygen defects on the surface of n-type PSi is less than that on the p-type PSi. The increase of the Si content in n-type PSi can influence the composition of SiO_x, changing the band gap structure. Simultaneously, the Cu related defects position in the band gap of SiO_x also changed, resulting the different PL performance between n and p-type PSi.

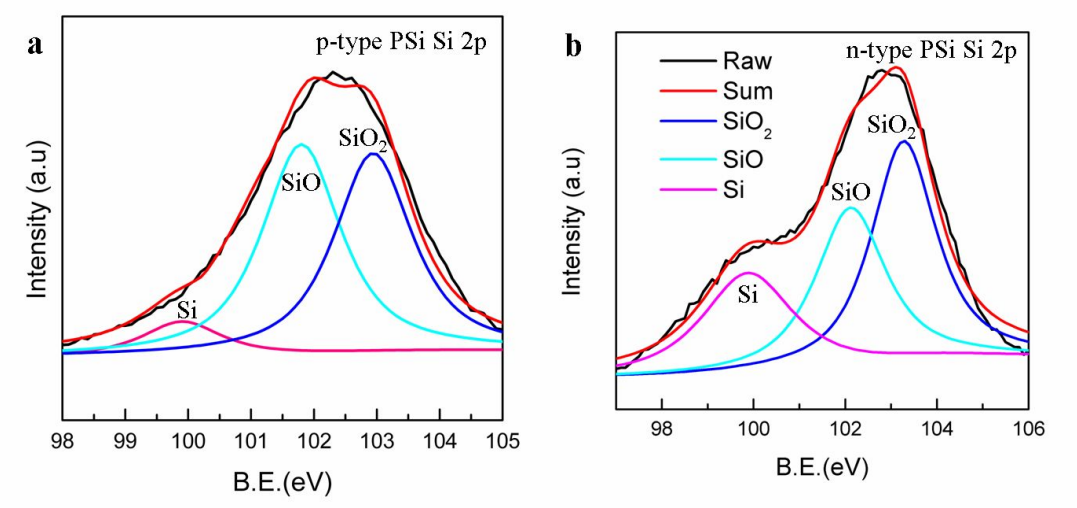


Figure 3.12. (a) Narrow XPS scan of Si 2p peak of the freshly prepared p-type PSi; (b) Narrow XPS scan of Si 2p peak of the freshly prepared n-type PSi.

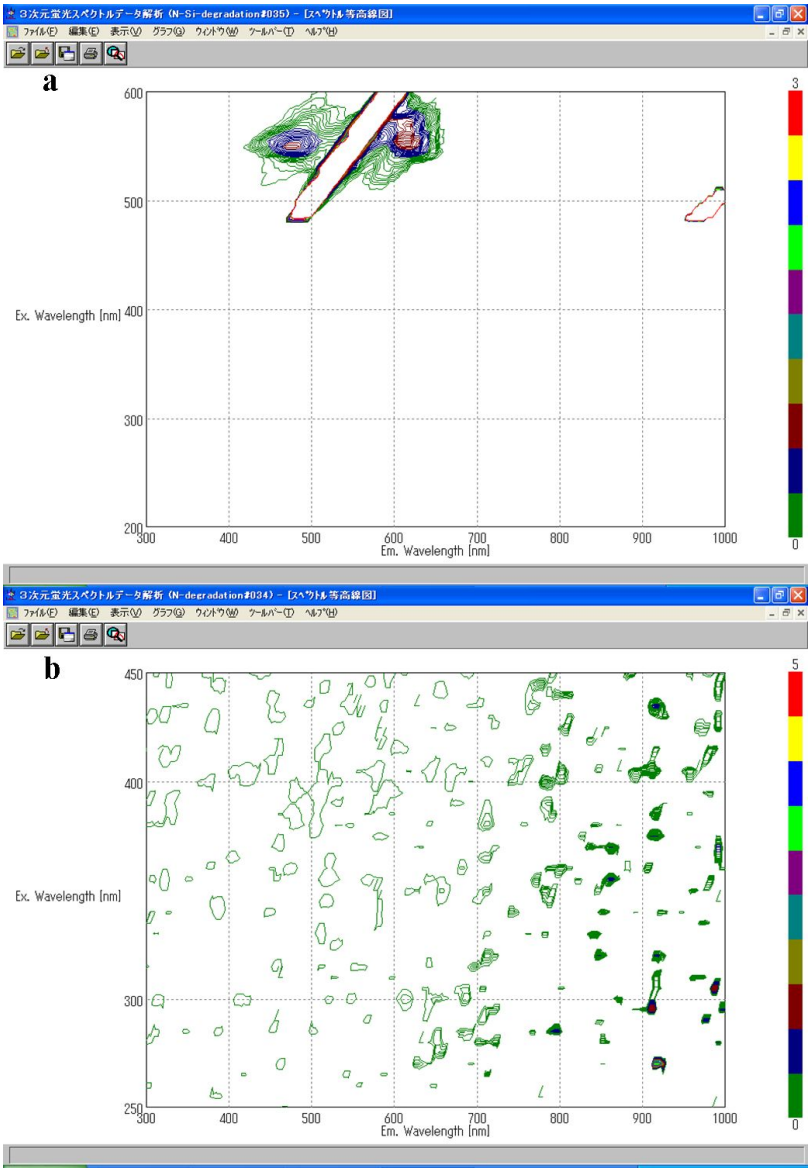


Figure 3.13. (a) 3D image of the PL aging result (1 month in air) of the n-type PSi prepared by Ag assisted method; (b) 3D image of the PL spectra of the related Cu-coated sample (aged in air for 1 month and 2-min Cu deposition time).

However, not all PSi samples can improve their PL behaviors by room temperature Cu-coating method. The n-type PSi prepared by Ag assisted method shows different result. Fig. 3.13 provides the PL aging results of the n-type PSi prepared by Ag assisted method (a) and the PL spectra of the related Cu-coated sample (b). The aging test result was same as the n and p-type PSi prepared by

electrochemical anodization, after exposed to ambient air for one month, PL disappeared. However, the Cu coating on this sample (pre-treatments are same as the n and p-type electrochemical anodized PSi) shows no change happened on the PL.

The reason for this phenomenon is that the surface states of silver assisted corroded sample are only Si and SiO_2 (Fig. 2.13b), no unstable states formed on the surface. That is to say, Cu related defects did not form on the surface, *i.e.*, Si and SiO_2 are very stable at room temperature, and Cu cannot react with them. After Cu coated, Cu, Si and SiO_2 were present in isolation, no influence with each other.

In this section, various Cu-PSi composite structures with changed PL were developed and the preparation did not require a high-temperature environment. P-type Cu-PSi showed a dual PL bands at blue and yellow range. Compared to the PL of fresh p-type PSi, the PL intensity of these two bands was increased. Simultaneously, the PL stability of Cu-PSi was also improved. The formation of Cu-related defect sites in the band gap of Si nanoparticle/SiO_x and less efficient oxidation process on the surfaces were determined as the major factors for the enhanced PL intensity and relatively high stability. The improved fluorescence properties of PSi may extend the opportunities for Si-based optoelectronics in the future. Simultaneously, PL from Cu-nPSi also showed an obvious stability improvement while the Cu-nPSi prepared by Ag assisted corrosion method did not show any improvement. Different surface states of these three samples cause their different PL behaviors.

3.2: The fluorescence properties of nanoisland-structured SiO_x/Cu_xO composite

3.2.1 Introduction

Although strong PL was observed from PSi, the PL emission always shows a single PL band. Recently, multi-visible-band emitting materials have been pursued in light-emitting field for the potential application as a white-light source. Because the PSi often shows a single PL, combine with some other fluorescent materials is a feasible way to obtain Si based multi-visible-band emitter. So far, although nano Cu/Cu^{+} can show blue emission,[99] Cu/PSi composites usually show either a single blue PL as the presence of Cu^{+} or Cu^{2+} disrupts the native red PL from PSi,[100,101] or a single red PL due to the relatively weak blue PL centers.[102] So, it is necessary to design Cu-Cu oxide/PSi composites with a suitable structure to obtain the dual/multiple-band PL emission with intensive intensities. One feasible approach is making the distribution of the Cu^{+}/Cu^{2+} and the red PL centers associated with non-stoichiometric silicon nanoparticles well separated to avoid the mutual disturbance between them. In this section, the issue of the dual-PL from Cu/Si composite will be addressed.

3.2.2 Experimental method for SiO_x/Cu_xO nano-island composite

Preparation of nano-island structured SiO_x/Cu_xO composite. First, Cu thin film was deposited onto a Si wafer by using a magnetron sputtering method as follows. The phosphorus-doped, <111>-oriented Si wafer, with an electrical resistivity less than 0.02 Ω·cm, was washed with ethanol and acetone by ultrasonic oscillation for 5 min, and then it was rinsed again with purified water. The pressure of the sputtering vacuum chamber was less than 5.0×10^{-3} Pa and then Ar gas was purged into the chamber at 2 Pa. The distance between the sample and the sputtering target was maintained at 60 mm. The sputtering current and period were set to 30 mA and 3 min,

respectively. The thickness of the deposited Cu layer is estimated at ~10 nm. Then, the obtained SiCu sample was anodized in an electrolyte consisting of $Fe(NO_3)_3$ (0.008 mol· dm^{-3}), HF (46 %), and purified water (HF: H2O = 7: 5 (v/v)) with a current density of 100 mA·cm^{-2} for 1 h. The obtained sample was washed by purified water and dried in air at room temperature.

Surface structure was observed by a JEOL JSM-6510LA scanning electron microscope (SEM), and surface composition analysis was carried out by a JEOL JPS-9200 X-ray photoelectron spectroscopy (XPS) device equipped with a monochromatic Mg Kα source operating at 100 W under ultrahigh vacuum (~1.0 × 10^{-7} Pa) condition; the obtained spectra were calibrated by the C 1s peak. Photoluminescence spectra were captured using a Jasco FP-6600 spectrofluorometer. A JEOL JIB-4600F/HDK multibeam system was used to process the FIB sample to obtain a final thickness less than 100 nm and the thus-prepared FIB sample was transferred to a molybdenum-grid transmission electron microscope (TEM) stage. The lateral structure, the related electron diffraction patterns and the energy-dispersive spectroscopy (EDS) spectra of the prepared sample were obtained by JEM-2010 transmission electron microscope (TEM, 200 kV).

3.2.3 Surface structure of the prepared SiO_x/Cu_xO composite

Surface morphology of the as-prepared SiO_x/Cu_xO composite is shown in Fig. 3.14b. The isolated nanoisland is observed on the surface with a diameter of 200–500 nm. Compared with the surface of the anodized bare Si sample shown in Fig. 3.14a, the density of the nanoisland decreased and the distance among nanoislands increased. Moreover, the HR-TEM image (Fig. 3.14c) shows the Si nanoparticles on the surface and the lattice fringes with distance of 3.15 Å, corresponding to distorted Si (111)

(3.13 Å). These Si nanoparticles play an important role in changing the native properties due to the quantum confinement (QC).

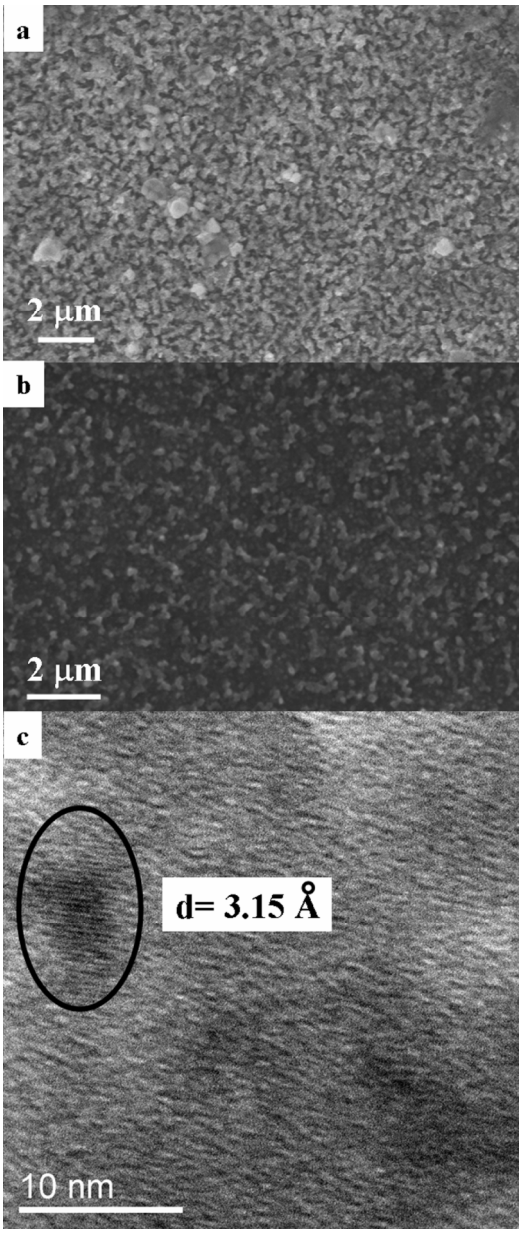


Fig. 3.14. (a) Scanning electron microscope (SEM) image of the electrochemical anodized bare Si. (b) SEM image of the surface morphology of the anodized SiO_x/Cu_xO composite. (c) High-resolution transmission electron microscope (HR-TEM) image of the surface structure of the sample shown in (b), the measured interplanar distance of 3.15 Å corresponds to the Si (111) plane (3.13 Å).

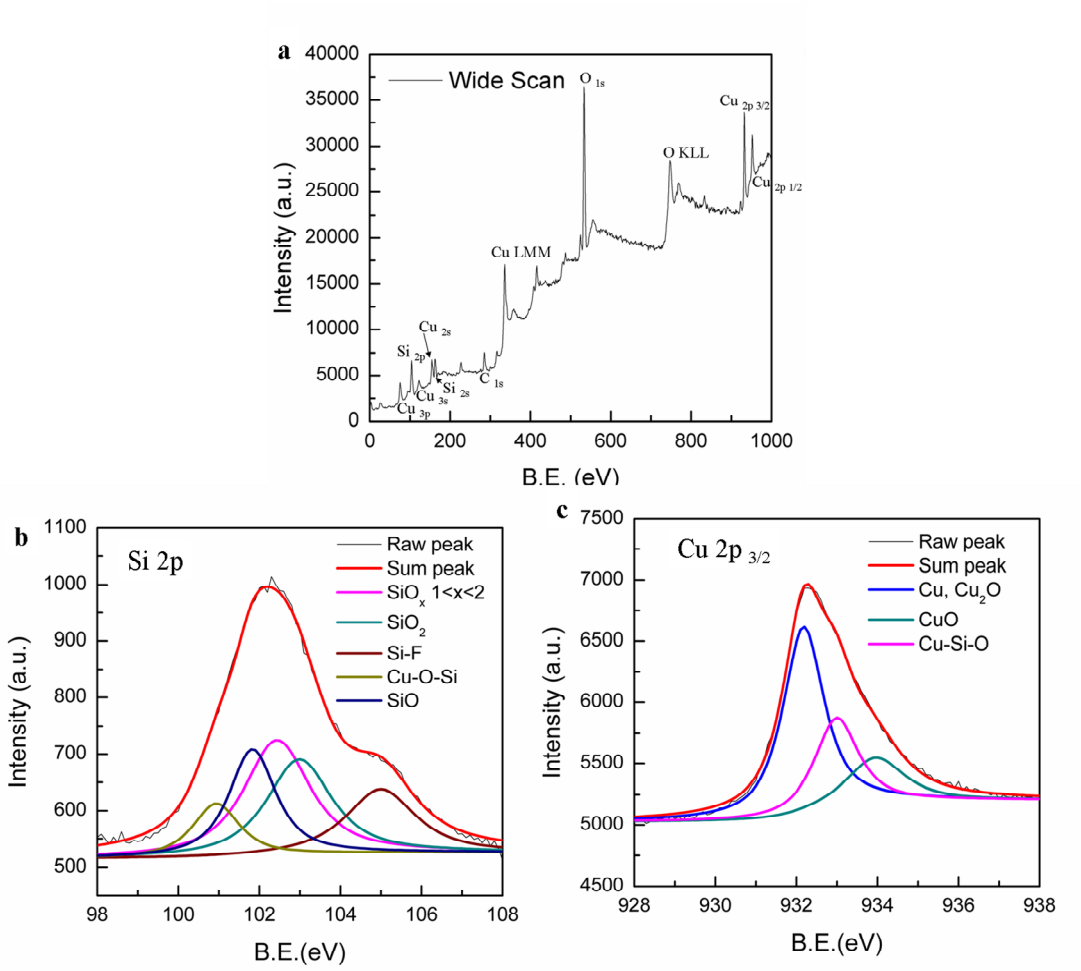


Fig. 3.15. (a) XPS wide-scan spectrum of the freshly prepared nanoisland SiOx/CuxO composite. (b) and (c) XPS narrow scan spectra of Si 2p area and Cu 2p3/2 area of freshly prepared nanoisland SiOx/CuxO composite, respectively.

Surface composition analysis of the prepared sample was carried out by XPS as shown in Fig. 3.15. The wide-scan XPS spectrum shown in Fig. 3.15a indicated that the sample surface comprised Si, Cu, C and O (H cannot be detected by XPS, even though it may exist on the surface). Detailed narrow-scan XPS of Si 2p and Cu $2p_{3/2}$ are shown in Figs. 3.15b and 3.15c. In the Si 2p spectrum, the main peak can be deconvoluted into five peaks at 100.8, 101.7, 102.5, 103.1 and 104.9 eV, which corresponded to Si–O–Cu, SiO, SiO_x ($1 < x < 2$), SiO_2 and Si–F structures (in the

order of increasing electro-negativity values of the elements bonded to Si from Cu to Si, O and F). F was not appeared in the wide-scan XPS spectrum; however, narrow-scan XPS can show a weak F 1s peak. Concurrently, narrow-scan XPS spectrum of Cu $2p_{3/2}$ showed that the Si–O–Cu structure also presented in the spectrum of Cu $2p_{3/2}$ area as well as the cuprous oxide and cupric oxide. The Cu ions are driven by electric potential and are moved into the protuberant nanoisland, these Cu ions may fill the interstitial vacancies (SiO, SiO_x) to form crystalline Cu and Cu-related defects (Si–O–Cu) that lead to blue PL. There was no characteristic peak of Si in the narrow-scan XPS spectra because the effective detection depth (less than 5 nm) of the XPS cannot reach the Si region, *i.e.*, after anodization, Si substrate was covered by Cu-oxides, Cu and Si-oxides, which will be discussed in Fig. 3.16.

Lateral morphology of the as-prepared nanoisland SiO_x/Cu_xO composited is shown in Fig. 3.16a. The height of the obtained nanoisland composite was ~150 nm. Simultaneously, different regions from the surface towards the Si substrate of the nanoisland composite were characterized by electron diffraction as shown in Figs. 3.16b–3.16d. Diffraction pattern of the protuberant area (80 nm from the substrate, Fig. 3.16b) showed only crystalline Cu_2O and Cu. The substrate is single-crystalline Si (Fig. 3.16c) and the sputtered Cu layer is only ~10 nm in thickness. The composition of the protuberant area was determined to be crystalline Cu_2O, Cu, amorphous Si oxides and amorphous CuO (as detected by XPS spectra shown in Fig. 3.15c). At the junction region (Fig. 3.16d) of the protuberant area and the bulk Si substrate, the pattern of Si was detected, although it was very weak. This indicated that Si nanoparticles shown in Fig. 3.14c may have come from this junction region and this explained the absence of Si in the XPS spectra shown in Fig. 3.15b.

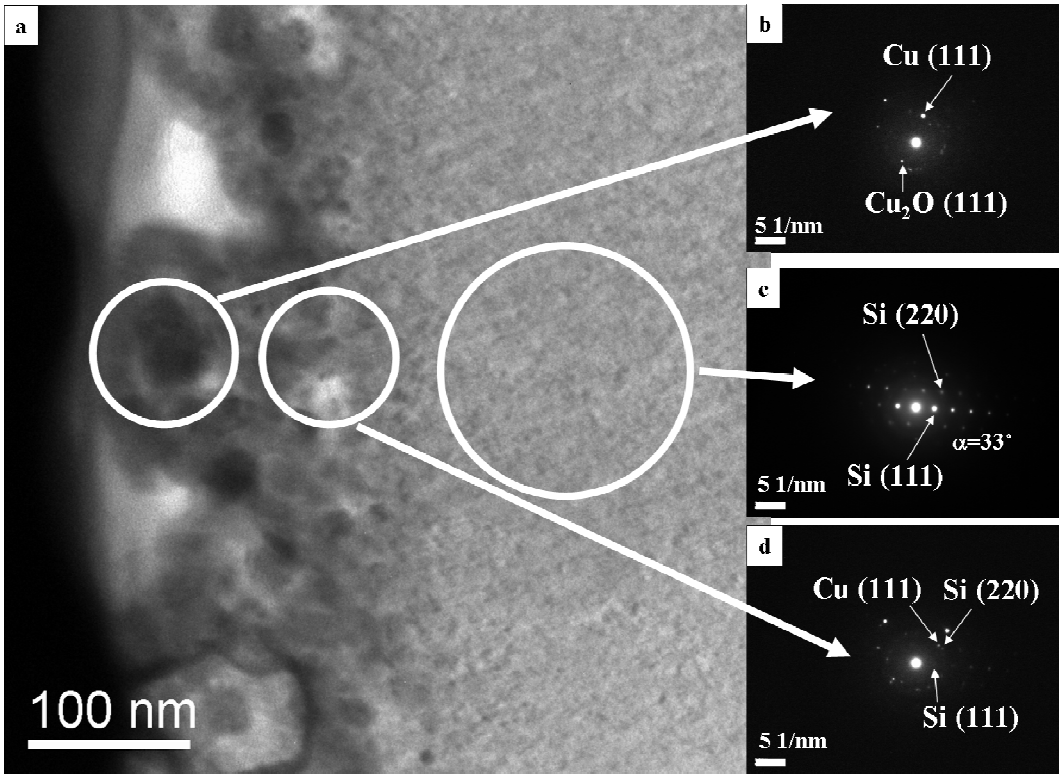


Fig. 3.16 (a) TEM image of the lateral structure of the prepared SiO_x/Cu_xO composite (the sample was prepared by focused ion beam (FIB) treatment; the thickness was less than 100 nm after FIB treatment). (b)–(d) Electron diffraction patterns of the corresponding circle regions, respectively.

This result further indicates that the Si nanoparticle area and Cu-oxides-concentrated area are separated. As the $Fe(NO_3)_3$ is an oxidant, compared to the sample prepared in the commonly used HF/ethanol electrolyte, the post-anodization oxidation degree of the outermost surface of our sample should be higher. In other words, the outermost surface is mainly composed of Si oxides, and Si nanoparticles are not concentrated on this region. However, from TEM image and diffraction results, $Cu^+/Cu2^+$ is mainly distributed at the outermost surface, indicating that red PL disturbance from Cu^+/Cu^{2+} can be avoided, which is crucial for dual PL emission.

3.2.4 Formation mechanism of SiO_x/Cu_xO nano-island composite

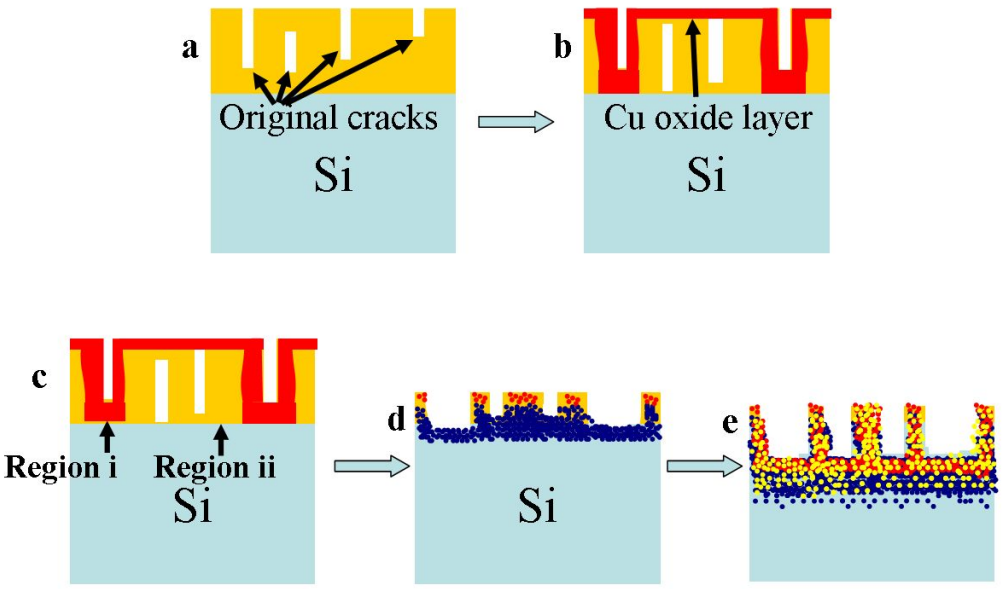


Fig. 3.17. Schematic of the formation mechanism (Red: Cu oxides; Light blue: Si; Dark blue dots: Si oxides; Yellow: Cu). (a) Cu sputtered Si wafer; (b) Cu sputtered Si wafer in air; (c) anodization start; (d) intermediate corrosion; (e) final obtained sample.

The schematic of the formation of the nanoisland-structured SiO_x/Cu_xO composite is shown in Fig. 3.17. Since the Cu cannot dissolve in HF, the key factors for the formation mechanism of nanoisland-structured SiO_x/Cu_xO composite are the native Cu oxides and the cracks in the Cu layer. As mentioned in Fig. 3.2, the Si surface is not an ideal surface, when a thin layer of Cu is deposited on the surface for a short period of time, it cannot form a continuous film due to surface tension (in our case, the thickness of the sputtered Cu layer was estimated at ~10 nm). That means the thin layer of Cu on the surface exists in the isolated block fashion. After Cu was sputtered on the Si surface, a thin original oxide layer will be formed automatically. This Cu oxide is soluble in acid solutions. At the beginning of the corrosion, the Cu

oxides were first dissolved by HF, and then, there are two corrosion routes.

Region i: This is the region underneath the bottom of the deep cracks. After the original Cu oxides were dissolved, these areas may come in contact with the electrolyte. Hence, the Si in this area may be corroded by the HF-containing electrolyte, as expressed in the below equations;

$$Cu_2O + 2HF \rightarrow 2CuF + H_2O \quad 3.1$$

$$Si + 4HF + 4h^+ \rightarrow SiF_4 + 4H^+ \quad 3.2$$

Region ii: This is the region underneath the Cu layer or the shallow, inner cracks. In these regions, after the original Cu oxides were dissolved, the Cu layer still remains thick enough, so that the corrosion speed became very slow. With help of the electric current, the Cu and the hydroxyl group (OH^-) formed Cu_2O again, and then the corrosion is repeated as shown in equations (1), (2) and (3). This process is expressed as the following equations.

$$2Cu + 2OH^- \rightarrow Cu_2O + H_2O + 2e^- \quad 3.3$$

$$Cu_2O + 2HF \rightarrow Cu_2F_2 + H_2O \quad 3.4$$

Finally, as the corrosion speeds of these two regions are different, the Cu-coated region became an island-shaped protuberance. In this case, the thickness of the Cu layer is a vital parameter for the formation of surface morphology as the cracks and native oxide layer conditions have a close relationship with the thickness of the deposited Cu layer.

3.2.5 Photoluminescence properties of SiO_x/Cu_xO nano-island composite

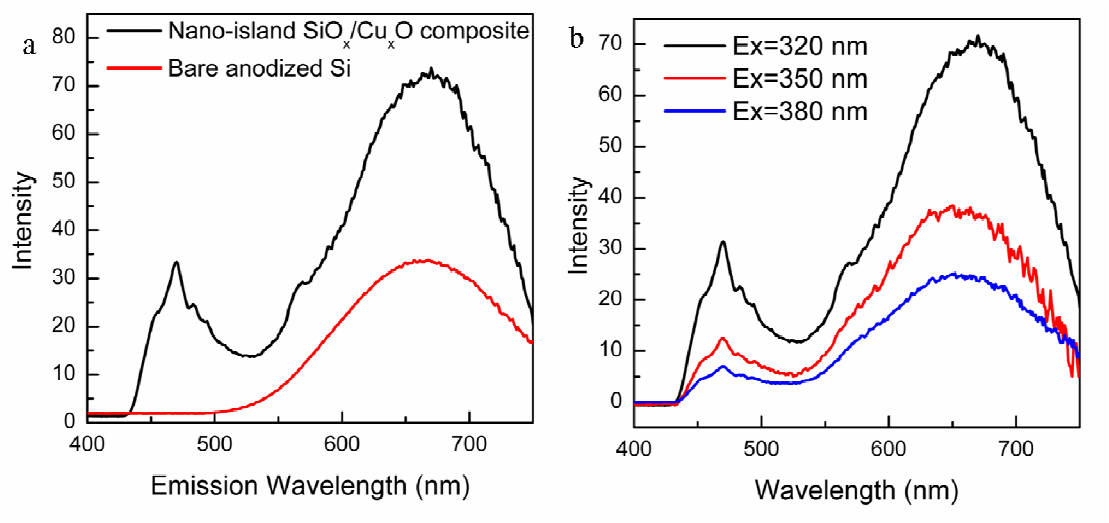


Fig. 3.18 (a) The fluorescence spectra of the freshly prepared nanoisland SiO_x/Cu_xO composite and anodized bare Si (the anodized bare Si was prepared by same method without Cu coating before electrochemical anodization. The emission spectra were collected at the excitation wavelength of 320 nm); (b) The fluorescence emission spectra of the freshly prepared nanoisland SiO_x/Cu_xO composite collected under different excitation wavelengths.

The fluorescence spectra of the freshly prepared nanoisland-structured SiO_x/Cu_xO composite and the anodized bare Si are shown in Fig. 3.18a. Compared to the anodized bare Si, nanoisland SiO_x/Cu_xO composite showed two comparable PL bands at the red zone (peak centroid at 660 nm) and the blue zone (peak centroid at 469 nm). Compared to the reported Cu/PSi that has a single blue emission, the quenching of the red PL usually associated with the Cu ions doping did not happen; in comparison with Cu/PSi that has a single red emission, the intensity of the blue emission was comparable with that of the red one. For the red PL from anodized bare Si, the mechanism involves the oxygen defects that are in the QC (arising from the Si nanoparticles). In the case of nanoisland SiO_x/Cu_xO composite, the red PL still arose from the oxygen defects under QC effect. XPS spectrum (Figure 3.15b) and HR-TEM

(Fig. 3.14c) image confirmed the presence of oxygen defects (SiO and Si_3O_4) and Si nanoparticles (nano size induces the QC effect). One phenomenon that usually happens in Cu-ions-doped PSi is PL quenching because of the disruption of band-to-band transition due to the presence of Cu^+/Cu^{2+} impurities in the band gap. However, in our case, it did not happen. From Figs. 3.16b and 3.16d, the Cu^+ and Cu^{2+} are mainly distributed in protuberance area while the red PL originated from the junction zone. The distribution of Cu oxides away from oxygen defect from Si oxides prevented quenching of the red PL. Concurrently, full-width at half-maximum (FWHM) of the red PL peak became wider due to the Cu ions diffused into the Si substrate driven by electric potential and these ions were reduced to Cu (unlike Cu^+ and Cu^{2+}, pure Cu did not influence the native PL from PSi). So, the holes from the Cu ions may transport to the Si substrate to form more defects, broadening the PL peak in the red zone. Note that there was a small sub-band at 570 nm in the spectrum of nanoisland SiO_x/Cu_xO composite. This peak may be originated from the remaining Cu_2O as the band gap energy of Cu_2O is ~2.1 eV (590 nm).[103] In previous studies, the blue peak was attributed to carbonyl compounds; however, in our case, the aqueous electrolyte solution of $HF/Fe(NO_3)_3$ did not contain any organic molecules. That means carbonyl compounds are not the reason for blue PL. In our case, the blue peak originated from the Cu-related defects which play the same role as a luminescent centre.

As the Cu has a high diffusivity and Cu ion can be driven by electric potential, both Cu and Cu ions can diffuse into the protuberance layer. They will fill the interstitial vacancies and some of them may combine with the unstable SiO, resulting in the formation of Cu-SiO_x (Figs. 3.15b and 3.15c, Si–O–Cu). All these defect states are PL centres. *e.g.*, Cu-related defects in the band gap of SiO_x that arose from $3d^{10} \leftrightarrow$

$3d^9 4s^1$ transitions of Cu^+ resulted in the blue emission. The spikes in the blue peak are due to the intra d → d band transition of Cu^{2+}. In comparison with a previous report, the relatively enhanced blue emission may be due to the uniform distribution of Cu on the surface. Previously reported samples showed a fiber columnar structure and the Cu elements were only concentrated at the top of the fiber columns, so, the blue PL centers were only present there.[102]

a

Element	Weight (%)	Atomic (%)
O	11.0	29.0
Si	14.4	21.6
Cu	74.6	49.4

b

Element	Weight (%)	Atomic (%)
O	11.4	29.2
Si	16.4	24.1
Cu	72.2	46.7

Fig.3.19. EDS quantitative analysis of different regions of the prepared nanoisland SiO_x/Cu_xO composite: (a) EDS quantitative analysis of the protuberance region; (b) EDS quantitative analysis of the connection region between two protuberances.

However, in our samples, Cu distribution was very uniform (Fig. 3.19) on the surface, therefore, Cu defects can cover the entire surface area. The improved blue PL was the consequence of the increase in number of PL centers. From the spectra shown in Fig. 3.18b, under different excitation wavelengths, the two emission peaks appeared at identical positions and both these two peaks weakened in intensity as the excitation wavelength increased. This further confirmed that defects are the main reason for the visible fluorescence because of the constant value difference between

the two defect levels.

In this section, a nanoisland-structured SiO_x/Cu_xO composite was synthesized by electrochemical anodization from a Cu deposited Si wafer. The nanoisland surface consisted of Si oxides, crystalline Cu and Cu_2O, and amorphous CuO and Si nanoparticles. The formation mechanism of this nanoisland structure depended on the structure and oxidation of the sputtered Cu layer. Fluorescence spectrum of the freshly prepared nanoisland-structured SiO_x/Cu_xO composite showed two luminescence bands at red and blue zones and the intensities of these two bands are comparable. The red PL quenching did not happen due to the distribution regions of Cu^+/Cu^{2+} and Si nanoparticles were separated, which prevented the mutual disturbance of them. Defects sites (oxygen- and Cu-related defects) under quantum confinement effect are the reason for the change. Compared to the single-PL-band sample, the dual-band one is more promising for making white light emitters.

In this chapter, PL behavior improvement was achieved by a room temperature Cu coating treatment, surface states of Si was a crucial factor for the PL improvement; simultaneously, dual PL emission was successfully observed from Cu/Si composite. The mutual disturbance of Cu^+/Cu^{2+} and Si nanoparticles was avoided due to the separated distribution of them. These improvements can extend the application fields of silicon as a potential optoelectronic candidate and a promising white light emitter.

Chapter 4: The Enhanced Far Infrared Emission from Semiconductor and Metal Composite Deposited on Surface Modified Silicon

4.1: Introduction of terahertz

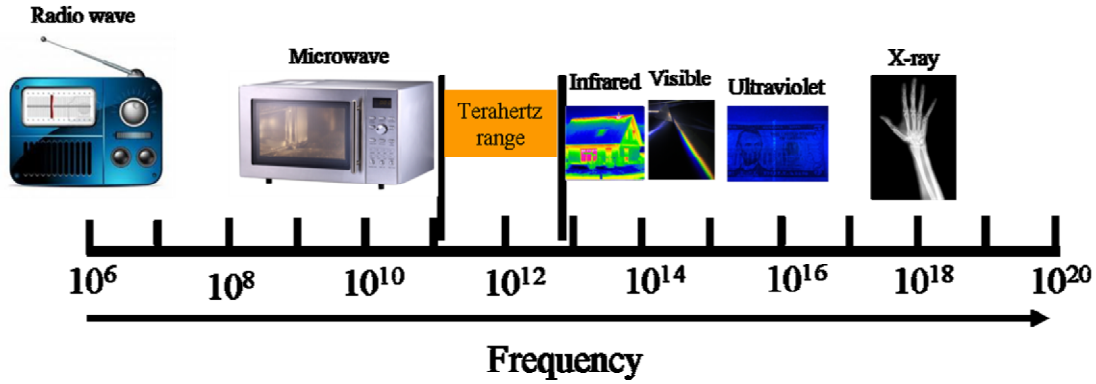


Fig. 4.1. Terahertz (THz) range in the frequency spectrum.

Terahertz (THz) radiation locates between the far-infrared and microwave regions and the corresponding frequency is at the range of $0.1 \times 10^{12} \sim 10 \times 10^{12}$. THz radiation is a promising technology in spectroscopy, imaging, and biological studies, among others.[104 – 106] Most dielectric and non-polar materials exhibit excellent transmissivity for THz radiation; therefore, it can be conveniently used in technologies for security check. In addition, the energy of the THz radiation is very low (~4.1 meV) compared to that of X-ray (100 eV ~ 100 keV), making it bio-friendly; therefore, it can be used for physical and medical investigation purposes and in non-damaging detection methods. In addition, the THz frequency range contains abundant information about molecular vibration and rotation, making the

THz spectrum an efficient means to identify the composition of materials.

4.2: New terahertz emission materials

Conventional THz materials are low-temperature grown GaAs (LT-GaAs), ZeTe, InAs etc. In recent time, new THz emitting materials has attracted much attention, especially the commonly used metals and semiconductors. Because these materials such as Si, Au and Cu are widely applied to microelectronic chip as the basic logical unit and intermediate layer for electronic adjustment, respectively. If intensive THz emission from these mentioned materials can be obtained, that will make THz technology potentially integrate with microelectronic device. Compare with the traditional THz emission materials, some commonly used semiconductors like Si, Ge, which have longer penetration depths,[59] that makes photon-generated carriers deviate from the surface field area (THz emission region). This, as well as the longer carrier lifetime (energy lost by heat in stead of the electromagnetic radiation), prevents the use of conventional indirect semiconductors as efficient THz emitters. For the metals, their surface field area is too narrow to produce intensive THz emission. So, in order to pursue the metal or indirect THz emitters, some specific treatments are required. Surface modification is an efficient approach to improving optical properties, thus overcoming the above-mentioned disadvantages. For example, nanostructured materials have been reported to be promising candidates for THz emitters, owing to their exceptional properties.[107–113] In particular, efficient THz emission has been reported for metallic nanostructured thin films and nanoarrays. Recent studies have

also reported the use of surface-modified conventional indirect semiconductors and metal/semiconductor composite as THz emitters without an external power supply.[59,114,115] However, until now, THz emission from above mentioned structure is still incomparable to traditional THz emitting materials. In this section, intensive THz emission from Cu_xO/metal nano thin film is presented.

4.3: Enhanced terahertz emission from Cu_xO/metal thin film deposited on surface modified silicon

4.3.1 Experimental method

In order to achieve above purpose, a columnar PSi was used as the substrate. The preparation method of the columnar PSi is same as the sample mentioned in section 2.1. B-doped (doping concentration is 1.0×10^{19} cm^3), <111> oriented silicon wafer was used as the anodized electrode, while Pt was used as the cathode. The electrolyte consisted of ferric nitrate (0.04 M), HF (46 %), and purified water (HF: H_2O = 7: 5 (v/v)). Current density was set to 100 mA cm^{-2} and maintained for 50 min at room temperature (RT).

The metal and semiconductor nano thin film was fabricated by magnetron sputtering method. Copper (Cu) and gold (Au) films were deposited by the magnetron sputtering method on both the planar and grating-structured silicon surfaces. The estimated thicknesses of Au and Cu are 50 and 160 nm, respectively. The obtained Cu/Au/Si samples were heated at 110 °C for different time periods in order to oxidize the copper layer (Cu oxides in the form of Cu_2O and CuO are semiconductors). Some samples were oxidized under ambient condition for at least one month.

A schematic illustration of the THz detection system is shown in Fig. 4.2. The femtosecond laser beam is split into two: the detection beam and the pump beam. The latter, at 45° with respect to the sample, illuminates the sample, generating THz emission, which is then collected by two parabolic mirrors and converges with the detection beam. These beams pass through an electro-optical crystal (ZeTe), and the signal amplitude is recorded on a computer. The femtosecond laser has a central wavelength of 800 nm with an 80-MHz repetition rate and 100-fs pulse width.

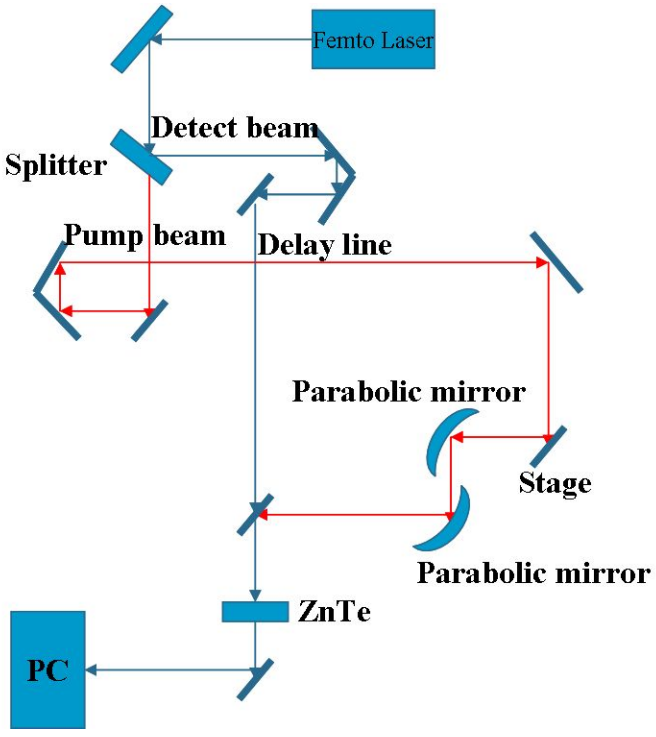


Fig. 4.2. Schematic illustration of the THz detection system.

Surface morphology of the prepared samples was characterized by a JEOL JSM-6510 scanning electron microscope (SEM). The JEOL JIB-4600F/HDK multi-beam system was used to process the sample for transmission electron microscope (TEM) observation and elemental mapping was carried out using a

Hitachi HD2000 scanning transmission electron microscope (STEM). Surface compositions were analyzed using a JEOL JPS-9200 X-ray photoelectron spectrometer (XPS).

4.3.2 THz emission mechanism from surface field

Fig. 4.3 shows the surface morphology of freshly obtained Cu/Au/PSi. The formation of regular micro-sized columns can be observed on the surface.

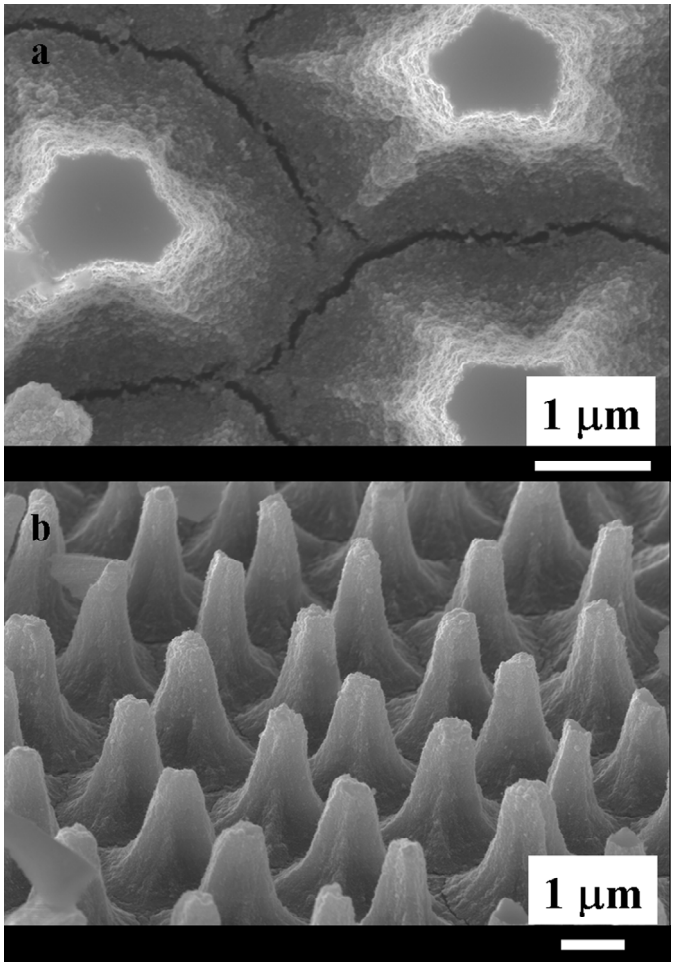


Fig. 4.3. (a) The surface structure of the bare porous silicon without metal deposition; (b) surface morphology of the fresh Cu/Au/MS-PSi (53° tilted); the sputtering thickness for Au and Cu are 50 and 160 nm, respectively.

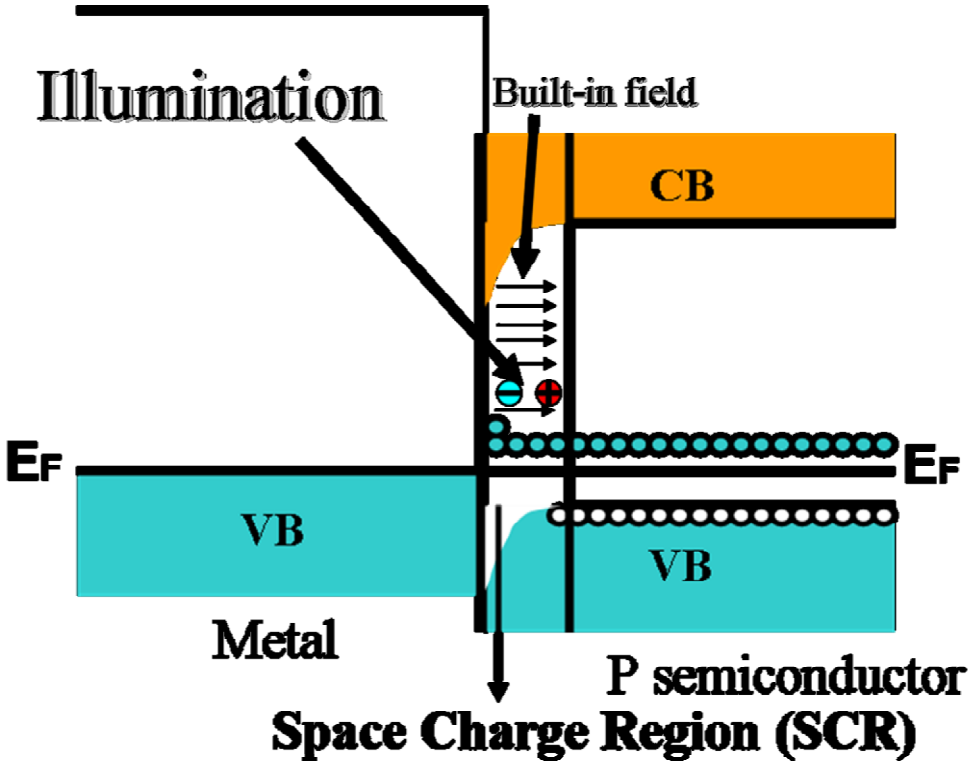


Fig. 4.4. Schematic diagrams of THz emission caused by built-in field at the interface.

A traditional way to generate and detect terahertz (THz) radiation is through ultrafast transient current, which originates from the motion of photon-generated electron–hole pairs in the built-in field on the surface or at the interface in semiconductors or semiconductor composites. In this case, the main reason of THz emission is the transient current induced in the built-in field at the interface between the metal and semiconductor (schematically represented in Fig. 4.4). In this study, I used two alloys, AuCu and Cu_xO ($x \leq 2$, heated or oxidized in air), as the metal and semiconductor, respectively. In this case, the contact between the metal and semiconductor is determined by their Fermi level (E_F). If the work function of the metal is lower than that of the semiconductor, electrons will flow into the semiconductor owing to the electric potential gradient. Assuming a p-type semiconductor (Cu_xO, $x \leq 2$), the incoming electrons decrease the density of the holes

at the semiconductor side. Finally, the space charge region is formed at the interface where the density of carriers is much lower than in the bulk. Under equilibrium, the induced built-in electric field overcomes the influence of the electron flow and no special optical phenomenon occurs. However, when the incident light illuminates the sample, photon-generated carriers can break the balance resulting in a transient current that radiates electromagnetic waves. The frequency of the emitted electromagnetic wave is proportional to the pulse width of the incident light. So, if the pulse width of the incident light is at the range of femto-second scale, the emitted electromagnetic wave will be at THz frequency region.

4.3.3 THz emission properties from Cu_xO/AuCu oxidized in air

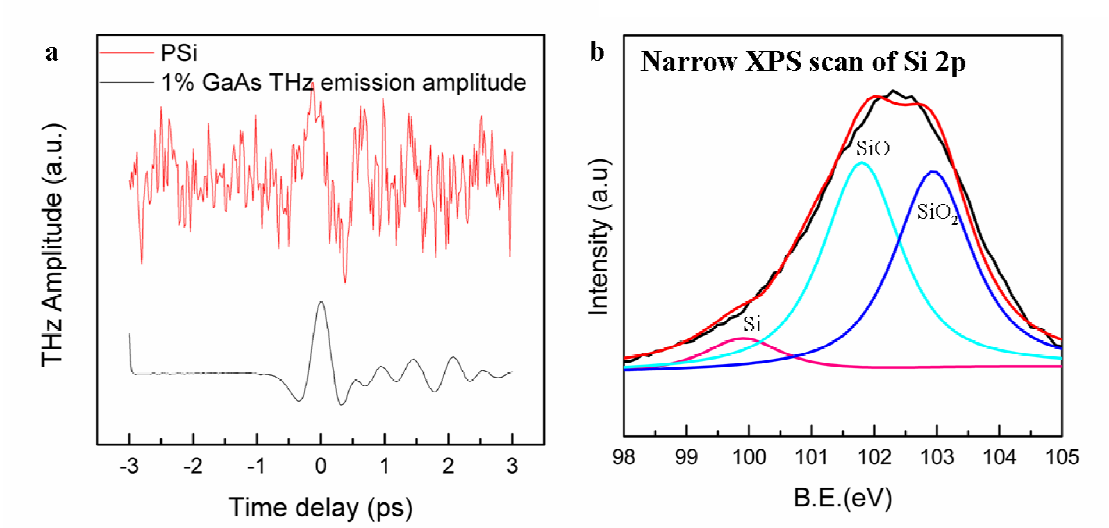


Fig. 4.5. (a) THz emission spectrum from bare PSi substrate; (b) Narrow XPS scan of Si 2p peak.

The emission properties from the bare PSi substrate are shown in Fig. 4.5a. In this case, use the THz emission amplitude of GaAs as the reference. In Fig. 4.5a, The THz emission amplitude from the PSi substrate is very weak with a poor signal to

noise ratio. That means the THz contribution of the PSi substrate can be ignored. Some reports about the PSi indicate that the PSi can enhance the THz emission capacity due to the multi-reflection among the surface structures that reduces the optical penetration depth. However, in my sample, the main surface states are Si oxides (SiO and SiO_2). The formation condition of the surface field shown in Fig. 4.4 is broken by these insulators, resulting in a poor THz emission performance from PSi substrate.

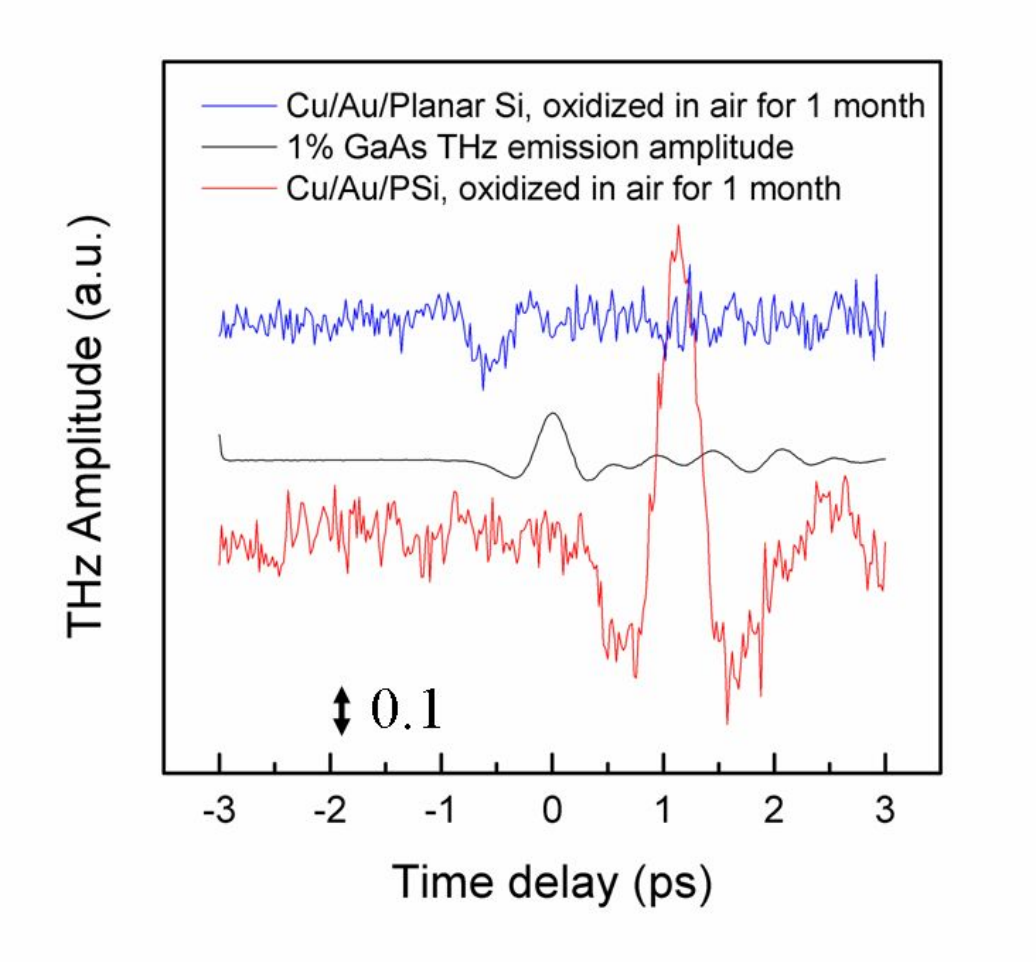


Fig. 4.6. THz emission properties from the Cu/Au/PSi samples oxidized in air automatically for one month.

First, the THz emission properties from the samples stored in air for one month

are shown in Fig. 4.6. Here, still use the THz amplitude value of GaAs as the reference and two kinds of samples were tested (blue line: Cu and Au were deposited on the planar Si substrate; red line: Cu and Au were deposited on the PSi substrate). THz emission amplitude from the Cu/Au/planar Si is only ~1% of the amplitude value from unbiased GaAs while the THz emission signal is obviously enhanced by using the PSi substrate, its amplitude can achieve ~5% of the amplitude value from unbiased GaAs.

4.3.4 THz emission properties from heated Cu_xO/AuCu

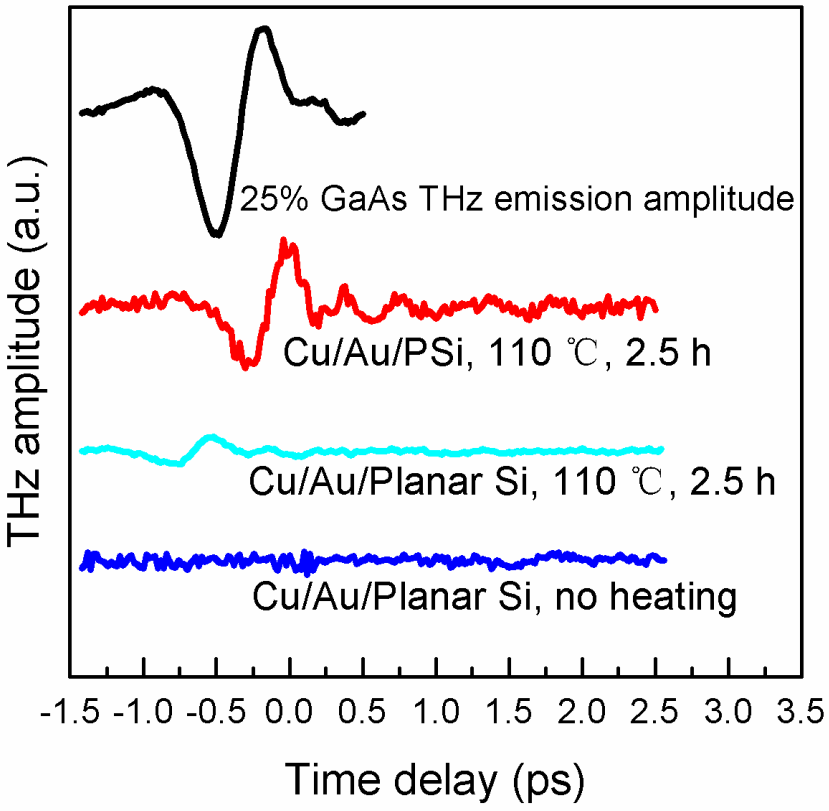


Fig. 4.7. THz emission properties from the Cu/Au/PSi samples heated at 110 ˚C for 2.5 h (storage time is one day in air after heating).

For the THz spectra shown in Fig. 4.6, storage in air for one month is an important factor. As mentioned in Fig. 4.4 part, metal and metal contact cannot produce any THz emission as the surface field can not induced efficiently at the interface of two metals. The Cu/Au layers oxidized in air can make the Cu layer become Cu_xO which comprises Cu, Cu_2O and CuO. The formed Cu_2O and CuO contact with the Au layer may match the formation conditions of the surface field. However, native oxidation in air has a disadvantage that the formed Cu oxides on the outermost layer are very stable at room temperature, which will hinder the inner oxidation happen. In order to make the oxidation of the Cu layer more efficiently, some prepared samples were heated at 110 $^{\circ}$C for 2.5 hours. The spectra of these heated samples are shown in Fig. 4.7. Similar with the results shown in Fig. 4.6, the THz emission of the sample on PSi substrate is several times higher that on the planar one and the amplitude is comparable to that from the GaAs. Simultaneously, the unheated sample does not show any THz emission. From above results, the PSi substrate plays a key role in THz emission enhancement no matter in heating or ambient treatment; the oxidation of the deposited Cu layer is very crucial for THz emission, the mild oxidized one (Fig. 4.7 cyan line) is very difficult to detect THz signal.

In order to find out the optimum for the oxidation of deposited Cu layer, THz emission tests of the Cu/Au/PSi heated at 110 $^{\circ}$C for different time and Cu/Au/PSi heated at 110 $^{\circ}$C for 2.5 h with different Cu thickness are shown in Fig. 4.8 and Fig. 4.9, respectively. In Fig. 4.8, at first, THz emission amplitude increased with the increase of the heating time, and then, it achieved the maximum value when the heating time is 2.5 h. After that, when the heating time is longer than 2.5 h, THz emission amplitude decreased very rapidly. From these results, one conclusion that

the composition of the heated Cu layer determines the THz emission efficiency can be summarized.

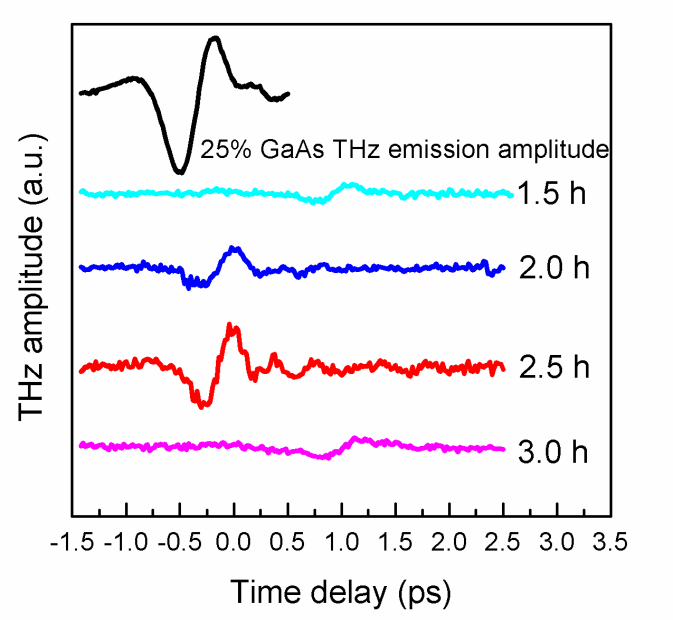


Fig. 4.8. THz emission properties from the Cu/Au/PSi samples heated at 110 ˚C for different time (storage time is one day in air after heating).

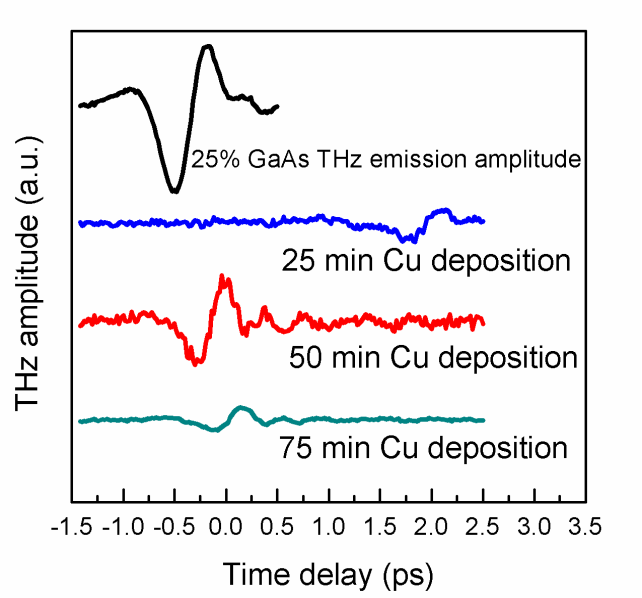


Fig. 4.9. THz emission properties from the Cu/Au/PSi samples heated at 110 ˚C for 2.5 h with different Cu thickness (storage time is one day in air after heating).

On the other hand, THz emission spectra from Cu/Au/PSi samples heated at 110 °C for 2.5 h with different Cu thickness further confirms the composition of the heated Cu layer is the decisive factor for THz emission, as shown in Fig. 4.9. Under same heating conditions, different amount of Cu means that the oxidation conditions of the Cu layers are different. As a result, THz emission amplitude shows various values. Combine with the results shown in Figs. 4.7 and 4.8, two obvious conclusion can be obtained: the oxidation situation of the deposited Cu layer is very important for THz emission; THz emission from the PSi substrate is several times higher than that from the planar one.

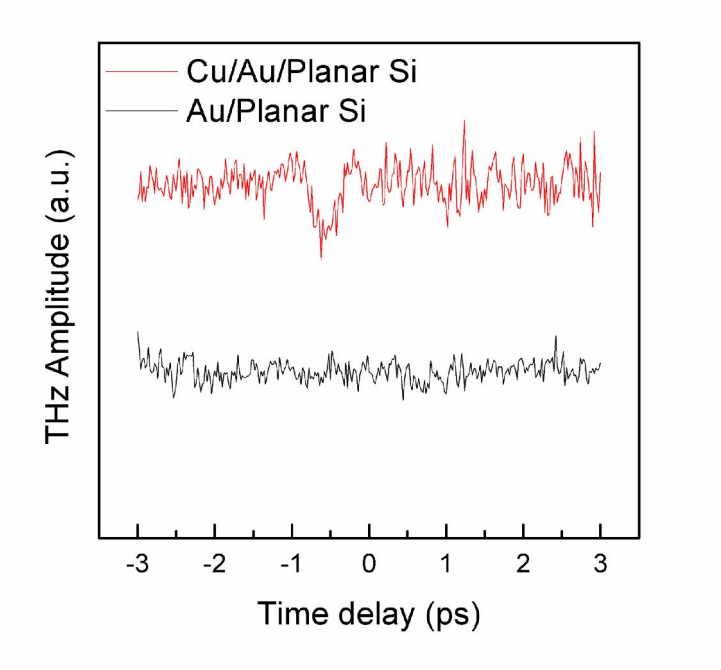


Fig. 4.10. THz emission spectra with different deposition conditions (red line: Cu (50 nm)/Au (3 nm) on the planar substrate oxidized in air automatically for 1 month; black line: only Au (3 nm) on the planar substrate oxidized in air automatically for 1 month).

4.3.5 Surface and interface structure of CuxO/AuCu

Simultaneously, THz emission spectrum from only Au deposited sample is shown in Fig. 4.10. That proves the Au and PSi interface did not offer any contribution to the THz radiation. Based on the theory mentioned in Fig. 4.4, Au and Si contact will not form a surface depletion region as the Fermi level of Au is higher than that of Si. Also, the Si surface was covered by Si oxides, so, the contact of Au and Si was hindered by this insulator layer. However, because the Fermi level of Au is higher than that of Cu and Cu oxides, contact of Cu_xO and Au also can not form a depletion region at their interface. To find out the interface structure of the Cu and Au interface after oxidation, STEM mapping images are shown in Fig. 4.11.

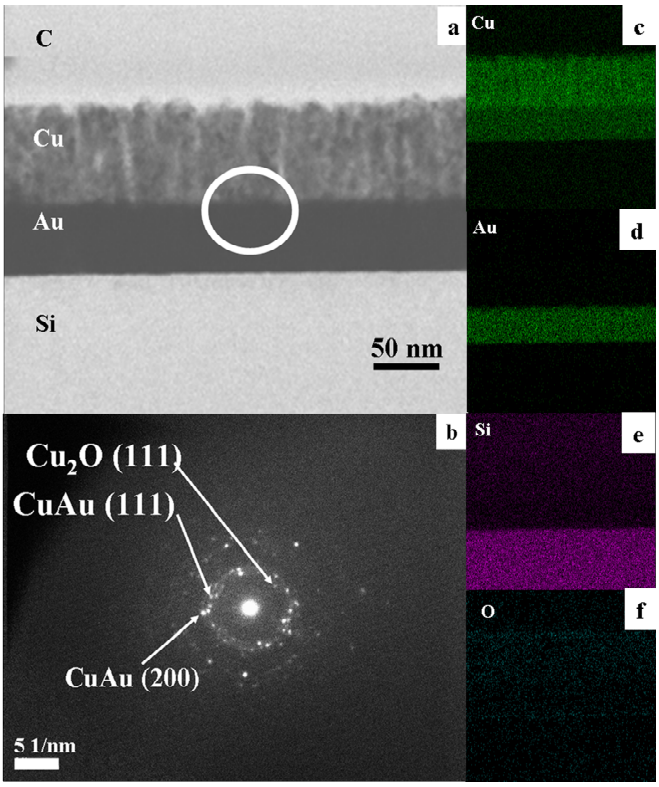


Fig. 4.11. (a) Interface structure of Cu (80 nm)/Au (50 nm) deposited on the planar silicon substrate oxidized in ambient air for four months; (b) selected area electron diffraction pattern at the Cu/Au layer (the white circular region in Fig. 4.11a); (c)–(f) elemental mapping results of the Cu/Au/Si sample shown in Fig. 4.11a.

The lateral image of the interface structure of Cu/Au on the planar silicon substrate is shown in Fig. 4.11a. Four layers were clearly observed: the bottom one was identified as the silicon substrate and the top one was the carbon layer used to protect the Cu/Au layers during TEM sample processing using focused ion beam (not presented in the THz testing samples). The SAED pattern, shown in Fig. 4.11b, confirmed that both Cu_2O and CuAu alloys are formed at the interface. According to our XPS spectra, amorphous CuO is also present on the surface (Fig. 4.12). Figs. 4.11a and 4.11b show the formation of Cu_xO ($x \leqslant 2$, semiconductor)/AuCu alloy (metal) on the surface. On the other hand, Figs. 4.11c – 4.11f show the elemental mapping results for the interface. An overlapping area between Cu and Au is clearly observed. Combining this with the SAED pattern, we understand that Cu diffuses into the Au plate, forming the AuCu alloy. Because the work function of Cu is lower than that of Au and so the CuAu alloy has a lower work function than Au, which induces the formation of the SCR.

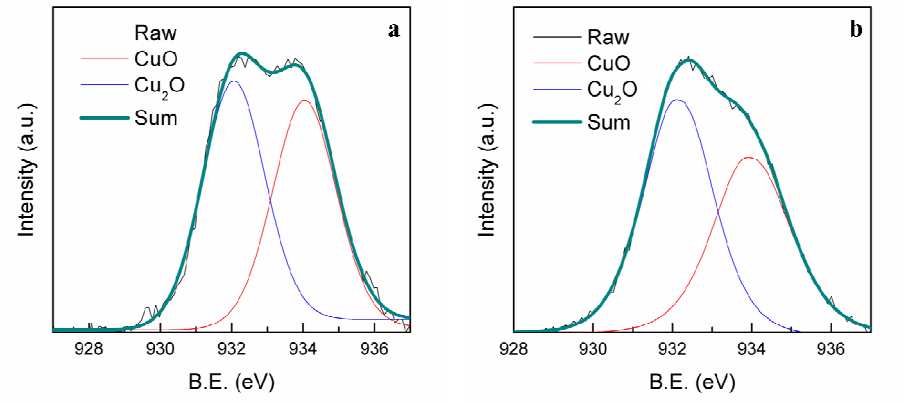


Fig. 4.12. (a) and (b) are XPS spectra of the different regions of the Cu (80 nm)/Au (50 nm)/ planar Si oxidized in ambient air for four months.

From the results discussed above, the degree of oxidation of the Cu layer is an important factor for THz emission from the Cu/Au thin film and is independent of the substrate. As mentioned above, the Cu/Au interface does not produce any THz radiation; therefore, the THz emission can be attributed to Cu_xO ($x \leqslant 2$). Both Cu_2O and CuO are p-type semiconductors with band gaps of 2.1 and 1.2 eV, respectively, which are higher and lower than the energy of the femtosecond laser (1.55 eV). The emission from femtosecond laser has a broad band, even that, band gap energy of Cu_2O (~590 nm) still higher than that of the short-wave band edge (~620 nm) of the laser source; meanwhile, the laser beam spot was not perfectly focused, which resulted in negligible two or multi-photon absorption arising from three or higher order nonlinear optics. Notably, CuO is an indirect semiconductor. For indirect semiconductors, a long carrier lifetime can lead to weak electromagnetic radiation. Therefore, a suitable band gap of the Cu oxide *i.e.*, a suitable value of the x in Cu_xO, that matches the energy of the incident light is essential for light absorption and consequent photon-induced carrier generation. In this study, the optimum oxidation conditions under ambient air are heating for 2.5 h at 110 ^{o}C.

Moreover, the role of the PSi substrate appears to be noteworthy as it contributes to much stronger THz emission compared to that from the planar Si substrate. This improvement is mainly attributed to three reasons. The first reason is the increase of the optical absorption (the related data is shown in Fig. 2.5). THz emission amplitude is proportional to the change rate of the photocurrent in the built-in field. The change rate of the photocurrent increases with higher density and shorter lifetime of the photon-generated carriers. Moreover, the density of the photon-generated carriers is

determined by the intensity of the built-in field and the optical absorption rate of the incident light. So, the enhanced optical absorption is an important parameter for the THz emission improvement. However, only the absorbed light in the built-in field will contribute the THz emission. Although light absorption depth in AuCu alloy is estimated to be 18 nm, the built-in field thickness in AuCu side is usually less than 1 nm. So, in AuCu, most of the light is absorbed out of the built-in field area. Localized surface plasmon resonance is a way to overcome this problem. In general, planar substrate cannot excite surface plasmon as the value of wave number of the surface plasmon is always higher than that of the incident light. But, in our case, the repeated surface column morphology can yield a higher wave number which is comparable to the value of the surface plasmon wave. As a result, considerable absorbed light was concentrated on the metal surface which overlaps with the built-in field region efficiently. The estimated order for matching the surface plasmon resonance condition is 8. Although at this order, the intensity of the absorbed light only takes a small amount of the total incident light, even the absorption increased a very small amount that can influence the final result very significantly. Third, the efficient contact area of the Cu_xO and CuAu was increased due to the columnar surface morphology. Use the image shown in Fig. 4.3, the contact area of the Cu_xO and Au on the PSi substrate is estimated ~ 6 times higher than than that on the planar substrate. In addition, the signal to noise ratio of the samples on the PSi substrate became lower compared with the sample on the planar one. The reason for this decrease is caused by the high adsorption capacity of the PSi, *i.e.*, the adsorbed water or carbon dioxide molecules can influence the emission of THz.

In this chapter, THz emission properties from Cu_xO and metal interface on planar and columnar substrate were investigated. The oxidation degree of the Cu layer was

very important for THz emission and the THz emission from sample deposited on the PSi substrate was about several times higher than that on the planar one. Increased optical absorption, enlarged contact area of Cu_xO and metal, as well as the surface plasmon resonance arose from the regular columnar surface contributed the enhanced THz emission. Moreover, THz emission amplitude of the Cu_xO/CuAu/PSi sample was comparable to the traditional THz emission material, GaAs, which is important for the development of THz integrated microelectronics.

Chapter 5: Summary and Future Work

Study in this dissertation focuses on the functionalization of surface modified silicon. The dissertation is constructed from five chapters as summarized below.

In chapter 1, the review on surface modification of silicon for functionalization, particularly the importance, applications and challenges, are presented. This chapter is directed to show the problems of surface modified silicon for optical applications, and my research objective and proposed approaches to overcome these problems. Silicon is a material of interest in many research areas and applications. However, for some optical applications, Si is not a good choice. In order to extend the application of Si, the silicon surface is often modified to achieve higher optical absorption, stronger and more stable visible fluorescence emission and so on. Despite the fact that there has been great improvement in this research field, the remaining challenges still hinder the practical applications. One of the problems associates with the formation of porous structure when the typical surface modified Si was prepared by common electrochemical anodization. The porous surface causes difficulties in the deposition of some additional homogenous thin metal layers which are often required to modify the electronic properties on demand for specific electronic applications. Simultaneously, the photoluminescence (PL) from such surface modified Si usually shows a single red emission with a poor stability. Therefore, the study presented in this dissertation is focused on solving these issues.

In chapter 2, preparation and formation mechanism of the columnar porous silicon (PSi) was investigated. Surface morphology of the traditional surface modified

Si prepared by electrochemical anodization in conventional aqueous hydrofluoric acid (HF)/ethanol electrolyte shows an irregular porous structure which is inconvenient to form homogeneous metal film structure on its surface for practical application. One way to solve this problem is preparing the columnar Si surface. For this purpose, an oxidant containing aqueous solution was used as the electrolyte to replace the conventional one. Various columnar PSis were obtained and the prepared samples with regular columnar surface are suitable candidates to form homogeneous metal films on its surface for practical devices. This is also the first time to synthesis the columnar surface by pure electrochemical anodization.

Chapter 3 is first focused on solving the problem of PL quenching related to the columnar PSi. In order to improve the stability of PL from the prepared columnar PSi, my study proposed a feasible approach to create stable PL center by sputtering deposition of a Cu layer onto the columnar PSi at room temperature followed by aging and HF etching. This method was proposed to protect and create stable PL centers by avoiding the effect of high temperature treatment which often required in common preparation technique. Compared to the unstable red PL of anodized porous Si, the resulting Cu coated porous Si after aging and etching shows a dual PL bands at blue and yellow range with increased intensity. These two emissions also exhibited a good stability with negligible degradation after three months. The improvement of PL can be attributed to the surface unstable SiO that combines with the sputtered Cu, forming new Cu related defect sites and surface nanostructures. These results can extend the application field of silicon as a potential optoelectronic candidate.

Secondly, the Si based white light emitting materials have been pursued in light-emitting field. However the combination of blue fluorescent Cu or Cu oxide

with red fluorescent PSi in single composites always shows a single PL emission as the mutual disturbance of Cu ions and PSi. Aiming to develop the dual or multiple PL emission with comparable intensity from Cu/PSi composite, my research focused on introducing the separation between these two types of PL emission centers in the composite via tailoring the surface structure. For this purpose, a nano-island structured SiO_x ($x \leqslant 2$)/Cu_xO ($x \leqslant 2$) composite was prepared from a Cu deposited Si wafer by electrochemical anodization in a HF and ferric nitrate electrolyte. The composition of the nano-island was consisted of Cu, Cu oxides, Si nanoparticles and Si oxides with separated distribution regions of the Cu ions and Si nanoparticle. As a result, an uncommon dual-visible-band PL at red and blue ranges with comparable intensity was observed. The origin of the red PL is due to oxygen defects in the band gap of Si nanoparticles/Si oxides; the blue PL is the consequence of the transitions between $3d^{10} \leftrightarrow 3d^9 4s^1$ of Cu^+ and the intra d $\rightarrow$ d band transition of Cu^{2+} in the interstitial vacancies of Si oxides. Compare to the electrochemical anodized bare Si sample, the nano-island structured SiO_x/Cu_xO composite emitting a dual-PL-band is more promising for white light emitter.

Chapter 4 is devoted is to utilize the columnar PSi for improvement of the terahertz (THz) emission from metal-semiconductor interface. THz emission from Cu_xO ($x \leqslant 2$)/AuCu nano thin film was studied by using the columnar PSi substrate. The results demonstrate that the THz emission from the samples on the columnar PSi was several times more efficient than that from the sample on planer Si substrate. Additionally, surface reflectance in the case of the PSi substrate was significantly reduced compare to that in the case of the planar one, owing to multiple reflections on the column surface. Because Si, Cu and Au are widely applied to microelectronic chip

as the logical unit and intermediate layer for electronic adjustment respectively, the enhanced THz emission from CuAu composite on PSi substrate can make THz technology potentially integrate with microelectronic device.

Finally, Chapter 5 summaries the contributions and future perspectives of my study presented in this dissertation. The successful functionalization of the surface modified Si is achieved including stable PL emission, dual PL from Si/Cu based materials and enhanced THz emission from metal/semiconductor on columnar PSi surface. The preparation methods and findings in my study contribute to the fundamental understanding on formation of columnar morphology, stabilization of PL center, creation of multiple PL emission based on modifying porous Si surface with metal and metal oxides, as well as the improvement of THz emission from the columnar PSi based composites. The results are important for the development of Si-based optoelectronic device and THz integrated microelectronics.

Nanostructured Si is a promising material in recent researches. Not only the research fields in this dissertation, but also, for example, surface enhanced Raman scattering, photovoltaic applications and LED heterojunction. The combination PSi and other optoelectronic materials have a promising future in efficient LED source.

Reference

1 D. A. Neamen, Semiconductor Physics and Device, McGraw-Hill, New York, NY 10020 (2003).

2 E. H. Nicollian and J. R. Brews, MOS (Metal Oxide Semiconductor) Physics and Technology, John Wiley & Sons, Somerset, New Jersey (1982).

3 G. P. Agrawal and N. K. Dutta, Long wavelength semiconductor lasers, Van Nostrand Reinhold Co. Inc., New York, NY (1986).

4 S. M. Sze，K. N. Kwok, Physics of Semiconductor Device, John Wiley & Sons, Hobuken, New Jersey (1986).

5 E. H. Rhoderick and R. H. Williams, Metal and Semiconductor Contacts, CLARENDON PRESS • OXFORD (1988).

6 D. K. Schroder, Semiconductor Material and Device Characterization, John Wiley & Sons, Hobuken, New Jersey (2006).

7 P. Antognetti and G. Massobrio, Semiconductor Device Modeling with Spice, McGraw-Hill, Inc. New York, NY, (1993).

8 M. E. Levinshtein, S. L. Rumyantsev and M. S. Shur, Properties of Advanced Semiconductor Materials: GaN, AIN, InN, BN, SiC, SiGe, John Wiley & Sons (2001).

9 K. Seeger, Semiconductor Physics: An Introduction, Springer-Verlag berlin Heidelberg New York (1991).

10 C. T. Sah, R. N. Noyce and W. Shockley, Carrier Generation and Recombination in P-N Junctions and P-N Junction Characteristics, *Proceeding of the Ire IEEE* **45**, 1228 (1957).

11 S. Nakamura, T. Mukai and M. Senoh, High-Power GaN P-N Junction Blue-Light-Emitting Diodes, *Jpn. J. Appl. Phys.* **30**, L1998 (1991).

12 F. C. Rong, W. R. Buchwald, E. H. Poindexter et al., Spin-dependent Shockley-read recombination of electrons and holes in indirect-band-gap semiconductor *p-n* junction diodes, *Solid-State Electronics* **34**, 835 (1991).

13 M. Aceves, J. Carrillo, J Carranza et al., Duality metal oxide semiconductor–PN junction in the Al/silicon rich oxide/Si structure as a radiation sensor, *Thin Solid Films* **373**, 134 (2000).

14 C. P. Please, An Analysis of Semiconductor P-N Junctions, IMA Journal of Applied Mathematics **28**, 301 (1981).

15 D. V. Kuksenkov, H. Temkin, A. Osinsky et al., Low-frequency noise and performance of GaN p-n junction photodetectors, *J. Appl. Phys.* **83**, 2142 (1998).

16 R. J. Stirn and Y. C. M. Yeh, A 15% efficient antireflection‐coated metal-oxide-semiconductor solar cell, *Appl. Phys. Lett.* **27**, 95 (1975).

17 A. Martí, N. López, E. Antolín, et al., Novel semiconductor solar cell structures: The quantum dot intermediate band solar cell, *Thin Solid Films* **511–512**, 638 (2006).

18 J. Shewchun, J. Dubow, C. W. Wilmsen et al., The operation of the semiconductor-insulator-semiconductor solar cell: Experiment, *J. Appl. Phys.* **50**, 2832 (1979).

19 K. Hara, T. Horiguchi, T. Kinoshita et al., Highly efficient photon-to-electron conversion with mercurochrome-sensitized nanoporous oxide semiconductor solar cells, *Solar Energy Materials and Solar Cells* **64**, 115 (2000).

20 J. H. Werner, S. Kolodinski and H. J. Queisser, Novel optimization principles and efficiency limits for semiconductor solar cells, *Phys. Rev. Lett.* **72**, 3851 (1994).

21 S. J. Fonash, The role of the interfacial layer in metal−semiconductor solar cells, *J. Appl. Phys.* **46**, 1285 (1975).

22 J. Shewchun, J. Dubow, A. Myszkowski et al., The operation of the semiconductor-insulator-semiconductor (SIS) solar cell: Theory, *J. Appl. Phys.* **49**, 855 (1978).

23 A. Mittiga, E. Salza, F. Sarto et al., Heterojunction solar cell with 2% efficiency based on a Cu_2O substrate, *Appl. Phys. Lett.* **88**, 163502 (2006).

24 J. F. Gibbons, G. W. Cogan, C. M. Gronet et al., A 14% efficient nonaqueous semiconductor/liquid junction solar cell, *Appl. Phys. Lett.* **45**, 1095 (1984).

25 F. Hetsch, X. Xu, H. Wang et al., Semiconductor Nanocrystal Quantum Dots as Solar Cell Components and Photosensitizers: Material, Charge Transfer, and Separation Aspects of Some Device Topologies, *J. Phys. Chem. Lett.* **2**, 1879 (2011).

26 D. E. Carlson and C. R. Wronski, Amorphous silicon solar cell, *Appl. Phys. Lett.* **28**, 671 (1976).

27 Q. H. Wang, K. Kalantar-Zadeh, A. Kis et al., Electronics and optoelectronics of two-dimensional transition metal dichalcogenides, *Nature Nanotechnology* **7**, 699 (2012).

28 D. Jariwala, V. K. Sangwan, L. J. Lauhon et al., Carbon nanomaterials for electronics, optoelectronics, photovoltaics, and sensing, *Chem. Soc. Rev.* **42**, 2824 (2013).

29 K. J. Ebeling, Integrated Optoelectronics: Waveguide Optics, Photonics, Semiconductors, Springer-Verlag berlin Heidelberg (1993).

30 K. Zhang， D. Li, Electromagnetic Theory for Microwaves and Optoelectronics, Springer-Verlag berlin Heidelberg New York (1998).

31 H. Zhong, Z. Bai and B. Zou, Tuning the Luminescence Properties of Colloidal I–III–VI Semiconductor Nanocrystals for Optoelectronics and Biotechnology Applications, *J. Phys. Chem. Lett.* **3**, 3167 (2012).

32 G. Eda and S. A. Maier, Two-Dimensional Crystals: Managing Light for Optoelectronics, *ACS Nano* **7**, 5660 (2013).

33 J. Liu, R. Camacho-Aguilera, J. T. Bessette et al., Ge-on-Si optoelectronics, *Thin Solid Films* **520**, 3354 (2012).

34 K. Gui, K. Mutkins, P. E. Schwenn et al., A flexible n-type organic semiconductor for optoelectronics, *J. Mater. Chem.* **22**, 1800 (2012).

35 P. Kambhampati, Multiexcitons in Semiconductor Nanocrystals: A Platform for Optoelectronics at High Carrier Concentration, *J. Phys. Chem. Lett.* **3**, 1182 (2012).

36 F. Pelayo García de Arquer and G. Konstantatos, Metal-insulator-semiconductor heterostructures for plasmonic hot-carrier optoelectronics, *Optics Express* **23**, 14715 (2015).

37 S. Zhang, Z. Yan, Y. Li et al., Atomically Thin Arsenene and Antimonene: Semimetal–Semiconductor and Indirect–Direct Band-Gap Transitions, *Angewandte Chemie* **127**, 3155 (2015).

38 H. Zhong, B. Chen, Z. Bai et al., Colloidal I-III-VI Semiconductor Nanocrystals for Light-emitting and Display Applications, International Photonics and Optoelectronics Meetings (POEM), Wuhan, China, 25–26 May 2013.

39 Y. S. Su and H. C. Chang, Bridging Photonics and Optoelectronics Curriculum for the Solar Photovoltaic and LED Industries, *International Journal of Photoenergy* **2014**, 1 (2014).

40 K. P. Homewood and M. A. Lourenço, Optoelectronics: The rise of the GeSn laser, *NATURE PHOTONICS* **9**, 78 (2015).

41 Z. Alferov, Heterostructures for Optoelectronics: History and Modern Trends, *Proceedings of the IEEE* **101**, 2176 (2013).

42 T. C. King, Y. P. Yang, Y. S. Liou et al., Tunable defect mode in a semiconductor-dielectric photonic crystal containing extrinsic semiconductor defect, *Solid State Communications* **152**, 2189 (2012).

43 M. J. Sailor, Porous silicon in practice: preparation, characterization and applications, Wiley-VCH, Weinheim, Germany (2012).

44 V. Torres-Costa and R. J. Martín-Palma, Application of nanostructured porous silicon in the field of optics. A review, *Journal of Materials Science* **45**, 2823 (2011).

45 R. J. Martin-Palma ; M. Manso-Silvan ; V. Torres-Costa, Biomedical applications of nanostructured porous silicon: a review, *J. Nanophoton.* **4**, 042502 (2010).

46 Z. Huang, N. Geyer, P. Werner et al., Metal-Assisted Chemical Etching of Silicon: A Review, *Adv. Mater.* **23**, 285 (2011).

47 C. D. G. Allan and M. Lannoo, Theoretical aspects of the luminescence of porous silicon, *Phys. Rev. B* **48**, 11024 (1993).

48 A. G. Cullis and L. T. Canham, Visible Light Emission Due to Quantum Size Effects in Highly Porous Crystalline Silicon. *Nature* **353**, 335 (1991).

49 J. A. Pradeep and P. Agarwal, An Alternative Approach to Understand the Photoluminescence and the Photoluminescence Peak Shift with Excitation in Porous Silicon. *J. Appl. Phys.* **104**, 123515 (2008).

50 L. Brus, Luminescence of Silicon Materials: Chains, Sheets, Nanocrystals, Nanowires, Microcrystals, and Porous Silicon. *J. Phys. Chem.* **98**, 3515 (1994).

51 H. Foll, M. Christophersen, J. Carstensen et al., Formation and application of porous silicon, *Materials Science and Engineering R* **39**, 93 (2002).

52 V. Lehmann and H. Foll, Formation Mechanism and Propeties of Electrochemically Etched Trenches in n-Type Si, *J. Electrochem. Soc.* **137**, 653 (1990).

53 S. Zangooie, R. Jansson, H. Arwin, Microstructural control of porous silicon by electrochemical etching in mixed HCl/HF solutions, *Appl. Surf. Sci.* **136**, 123 (1998).

54 T. Unagami, Formation Mechanism of Porous Silicon Layer by Anodization in HF Solution, *J. Electrochem. Soc.: SOLID-STATE SCIENCE AND TECHNOLOGY* **127**, 476 (1980).

55 B. Zhang, H. Wang, L. Lu et al., Large-Area Silver-Coated Silicon Nanowire Arrays for Molecular Sensing Using Surface-Enhanced Raman Spectroscopy, *Adv. Funct. Mater.* **18**, 2348 (2008).

56 L. A. Porter, Jr., Hee Cheul Choi, J. M. Schmeltzer, Electroless Nanoparticle Film Deposition Compatible with Photolithography, Microcontact Printing, and Dip-Pen Nanolithography Patterning Technologies, *Nano Lett.* **2**, 1369 (2002).

57 K. Peng, Y. Wu, H. Fang et al. Uniform, Axial-Orientation Alignment of One-Dimensional Single-Crystal Silicon Nanostructure Arrays, *Angew. Chem. Int. Ed.* **44**, 2737 (2005).

58 R. Fan, Y. Wu, D. Li, Fabrication of Silica Nanotube Arrays from Vertical Silicon Nanowire Templates, *J. Am. Chem. Soc.*, **125**, 5254 (2003).

59 P. Hoyer, M. Theuer, R. Beigang, Terahertz emission from black silicon, *Appl. Phys. Lett.* **93**, 091106 (2008).

60 E. Garnett and P. Yang, Light Trapping in Silicon Nanowire Solar Cells, *Nano Lett.*, **10**, 1082 (2010).

61 M. Nolan, S. O'Callaghan, G. Fagas et al., Silicon Nanowire Band Gap Modification. *Nano Lett.* **7**, 34 (2007).

62 D. Nesheva, C. Raptis, A. Perakis, Raman Scattering and Photoluminescence from Si Nanoparticles in Annealed SiO_x Thin Films, *J. Appl. Phys.* **92**, 4678 (2002).

63 Y. Q. Wang, Y. G. Wang, L. Cao, et al., High-efficiency Visible Photoluminescence from Amorphous Silicon Nanoparticles Embedded in Silicon Nitride, *Appl. Phys. Lett.* **83**, 3474 (2003).

64 D. Brodoceanu, R. Elnathan, B. Prieto-Simon et al., Dense Arrays of Uniform Submicron Pores in Silicon and Their Applications, *ACS Appl. Mater. Interfaces* **7**, 1160 (2015).

65 J. A. L. López, G. G. Salgado, A. P. Pedraza et al., Structural and Optical Properties of SiOx Films Deposited by HFCVD, *Proc. Eng.* **25**, 304 (2011).

66 O. A. Yeshchenko, I. M. Dmitruk, A. A. Alexeenko et al., Size-dependent Surface-plasmon-enhanced Photoluminescence from Silver Nanoparticles Embedded in Silica, *Phys. Rev. B* **79**, 235438 (2009).

67 G. W. Meng, X. S. Peng, Y. W. Wang et al., Synthesis and Photoluminescence of Aligned SiO_x Nanowire arrays, *Appl. Phys. A* **76**, 119 (2003).

68 Y. W. Wang, C. H. Liang, G. W. Meng et al., Synthesis and Photoluminescence Properties of Amorphous SiO_x Nanowires, *J. Mater. Chem.* **12**, 651 (2002).

69 E. Kayahan, The Role of Surface Oxidation on Luminescence Degradation of Porous Silicon, *Appl. Surf. Sci.* **257**, 4311 (2011).

70 T. Nakamura, T. Ogawa, N. Hosoya et al., Effects of Thermal Oxidation on the Photoluminescence Properties of Porous Silicon, *J. Lumin.* **130**, 682 (2010).

71 H. J. Xu and X. J. Li, Silicon Nanoporous Pillar Array: A Silicon Hierarchical Structure with High Light Absorption and Triple-band Photoluminescence, *Opt. Express* **16**, 2933 (2008).

72 P. Menna, G. D. Francia, V. L. Ferrara, Porous silicon in solar cells: a review and a description of its application as an AR coating, *Solar Energy Materials and Solar Cells* **37**, 13 (1995).

73 C. B. Han , C. He , and X. J. Li, Near-Infrared Light Emission from a GaN/Si Nanoheterostructure, *Array, Adv. Mater.* **23**, 4811 (2011).

74 Z. Zhang and J. T. Yates, Jr., Band Bending in Semiconductors: Chemical and Physical Consequences at Surfaces and Interfaces, *Chem. Rev.* **112**, 5520 (2012).

75 X. T. Zhou, R. Q. Zhang, H. Y. Peng et al., Highly Efficient and Stable Photoluminescence from Silicon Nanowires Coated with SiC, *Chem. Phys. Lett.* **332**, 215 (2000).

76 B. Gelloz, A. Kojima and N. Koshida, Highly Efficient and Stable Luminescence of Nanocrystalline Porous Silicon Treated by High-pressure Water Vapor Annealing. *Appl. Phys. Lett.* **87**, 031107 (2005).

77 A. Daami, G. Bremond, L. Stalmans et al., Efficient Luminescence from Porous Silicon, *J. Lumin.* **80**, 169 (1999).

78 L. Lin, X. Sun, R. Tao et al., The Synthesis and Photoluminescence Properties of Selenium-treated Porous Silicon Nanowire Arrays, *Nanotech.* **22**, 075203 (2011).

79 M. Rahmani, A. Moadhen, M. A. Zaibi et al., Photoluminescence Enhancement and Stabilisation of Porous Silicon Passivated by Iron, *J. Lumin.* **128**, 1763 (2008).

80 E. Kayahan, White Light Luminescence from Annealed Thin ZnO Deposited Porous Silicon, *J. Lumin.* **130**, 1295 (2010).

81 N. Negishi, M. Matsuoka, H. Yamashita et al., Characterization of Copper Ion Catalyst Encapsulated in SiO2 Matrices by the Sol-Gel Method and Their Photocatalytic Activity for Decomposition of NO into N2 and O2 at 275 K, *J. Phys. Chem.* **97**, 5211 (1993).

82 D. Andsager, J. Hilliard, J. M. Hetrick et al., Quenching of porous silicon photoluminescence by deposition of metal adsorbates, *J. Appl. Phys.* **74**, 4783 (1993).

83 D. K. Polyushkin, E. Hendry, E. K. Stone et al., THz Generation from Plasmonic Nanoparticle Arrays, *Nano Lett.* **11**, 4718 (2011).

84 L. Brewer and R. K. Edwards, The stability of SiO solid and gas, *J. Phys. Chem.*, **58**, 351 (1954).

85 A. Mesli and T. Heiser, Defect reactions in copper-diffused and quenched p-type silicon, *Phys. Rev. B* **45**, 11632 (1992).

86 A. A. Istratov, C. Flink, H. Hieslmair et al., Intrinsic Diffusion Coefficient of Interstitial Copper in Silicon, *Phys. Rev. Lett.* **81**, 1243 (1998).

87 G. Zhang, J. Long, X. Wang et al., Controlled synthesis of pure and highly dispersive Cu(II), Cu(I), and Cu(0)/MCM-41 with $Cu[OCHMeCH2NMe_2]_2$/MCM-41 as precursor, *New J Chem.* **33**, 2044 (2009).

88 M. Anpo, Y. Shioya, H. Yamashita et al., Preparation and Characterization of the Cu+/ZSM-5 Catalyst and Its Reaction with NO under UV Irradiation at 275 K. In situ Photoluminescence, EPR, and FT-IR Investigations, *J. Phys. Chem.* **98**, 5744 (1994).

89 M. Nakamura and S. Murakami, Deep-Level Transient Spectroscopy and Photoluminescence Studies of Formation and Depth Profiles of Copper Centers in Silicon Crystals Diffused with Dilute Copper, *Jpn. J. Appl. Phys.* **49**, 071302 (2010).

90 Y. M. Huang, Photoluminescence of copper‐doped porous silicon, *Appl. Phys. Lett.* **69**, 2895 (1996).

91 A. Carvalho, D. J. Backlund and S. K. Estreicher, Four-copper complexes in Si and the Cu-photoluminescence defect: A first-principles study, *Phys. Rev. B* **84**, 155322 (2011).

92 N. Lopez, F. Illas and G. Pacchioni, Adsorption of Cu, Pd, and Cs atoms on regular and defect sites of the SiO_2 surface, *J. Am. Chem. Soc.* **121**, 813 (1999).

93 M. Steger, A. Yang and T. Sekiguchi, Photoluminescence of deep defects involving transition metals in Si: New insights from highly enriched 28Si, *J. Appl. Phys.* **110**, 081301 (2011).

94 S. B. Jung, H. H. Park and H. C. Kim, Investigation of the bonding states of the SiO2 aerogel film/metal interface, *Thin Solid Films* **447-448**, 575 (2004).

95 W. Lin and H. Frei, Anchored Metal-to-Metal Charge-Transfer Chromophores in a Mesoporous Silicate Sieve for Visible-Light Activation of Titanium Centers, *J. Phys. Chem. B* **109**, 4929 (2005).

96 D. B. Mawhinney, J. A. Glass and J. T. Yates, FTIR Study of the Oxidation of Porous Silicon, *J. Phys. Chem. B* **101**, 1202 (1997).

97 M. Dai, J. Kwon, M. D. Halls et al., Surface and interface processes during atomic layer deposition of copper on silicon oxide, *Langmuir* **26**, 3911 (2010).

98 M. Dai, J. Kwon, E. Langereis et al., In-situ FTIR study of atomic layer deposition (ALD) of copper metal films, *ECS Trans.* **11**, 91 (2007).

99 M. Chiba, M. N. Thanh, Y. Hasegawa et al., Synthesis of binary solid solution Cu–Pd nanoparticles by DMF reduction for enhanced photoluminescence properties, *J. Mater. Chem. C* **3**, 514 (2015).

100 K. Y. Suh, Y. S. Kim and H. H. Lee, Blue photoluminescence from in situ Cu-doped porous silicon, *J. Appl. Phys.* **91**, 10206 (2002).

101 X. Lu, Y. Ishida and T. Yonezawa, Synthesis and fluorescence property of columnar porous silicon: the influence of Cu-coating on photoluminescence behaviours from hydrofluoric-acid-treated aged columnar porous silicon, *New J. Chem.* **39**, 6267 (2015).

102 M. Naddaf, O. Mrad and A. Al-zier, Characterization of nanostructured CuO–porous silicon matrix formed on copper-coated silicon substrate via electrochemical etching, *Appl. Phys. A* **115**, 1345 (2014).

103 M. Izaki, T. Shinagawa, K. T. Mizuno et al., Electrochemically constructed p-Cu_2O/n-ZnO heterojunction diode for photovoltaic device, *J. Phys. D: Appl. Phys.* **40**, 3326 (2007).

104 B. B. Hu and M. C. Nuss, Imaging with terahertz waves, *Opt. Lett.* **20**, 1716 (1995).

105 N. Li, J. Shen, J. Sun et al., Study on the THz spectrum of methamphetamine, *Opt. Express* **13**, 6750 (2005).

106 M. R. Scarfi, M. Romano, R. Di Pietro et al., THz exposure of whole blood for the study of biological effects on human lymphocytes, *J. Biol. Phys.* **29**, 171 (2003).

107 Y. Gao, M. Chen, C. Yang et al., Analysis of terahertz generation via nanostructure enhanced plasmonic excitations, *J. Appl. Phys.* **106**, 074302-1 (2009).

108 G. H. Welsh and K. Wynne, Generation of ultrafast terahertz radiation pulses on metallic nanostructured surfaces, *Opt. Express* **17**, 2470 (2009).

109 R. B. Jaculbia, M. H. M. Balgos, N. S. Mangila IV et al., Enhanced terahertz emission from GaAs substrates deposited with aluminium nitride films caused by high interface electric fields, *Appl. Surf. Sci.* **303**, 241 (2014).

110 C. A. Meserole, G. L. Fisher, D. J. Hilton et al., Growth of thin Fe (001) films for terahertz emission experiments, *Appl. Surf. Sci.* **253**, 6992 (2007).

111 F. Kadlec and P. Kužel, Study of terahertz radiation generated by optical rectification on thin gold films, *Opt. Lett.* **30**, 1402 (2005).

112 X. Wu, B. Quan, X. Xu et al., Effect of inhomogeneity and plasmons on terahertz radiation from GaAs (100) surface coated with rough Au film, *Appl. Surf. Sci.* **285P**, 853 (2013).

113 H. Ahn, Y. P. Ku, Y. C. Wang et al., Terahertz emission from vertically aligned InN nanorod arrays, *Appl. Phys. Lett.* **91**, 132108 (2007).

114 G. B. Jung, Y. J. Cho, Y. Myung et al., Geometry-dependent terahertz emission of silicon nanowires, *Opt. Express* **18**, 16353 (2010).

115 G. K. P. Ramanandan, A. J. L. Adam and P. C. M. Planken, Enhanced terahertz emission from Schottky junctions using plasmonic nanostructures, *ACS Photonics* **1**, 1165 (2014).

List of Research Achievement

Journal Publications:

[1] X. Lu, Y. Ishida, and T. Yonezawa, Synthesis and fluorescence properties of columnar porous silicon: the influence of Cu-coating on the photoluminescence behaviour of hydrofluoric-acid-treated aged columnar porous silicon, *New J. Chem.*, 2015, **39**, 6267.

[2] X. Lu, Y. Ishdia, T. M. Nguyen, and T. Yonezawa, Synthesis and fluorescence properties of nanoisland-structured SiO_x/Cu_xO composite, *Journal of Materials Chemistry C*, 2015, **3**, 8358.

[3] X. Lu, Y. Ishida, T. Mishina, M. T. Nguyen, and T. Yonezawa, Enhanced Terahertz Emission from Cu_xO/Metal Thin Film Deposited on Columnar-Structured Porous Silicon, *Bullentin of Chemical Society of Japan*, DOI: 10.1246/bcsj.20150173, in press.

[4] X. Lu and T. Yonezawa, Terahertz emission from Cu_xO/Au thin film, *Microwave Photonics (MWP) and the 2014 9th Asia-Pacific Microwave Photonics Conference (APMP)*, IEEE, 2014, 164–165.

[5] C. Xue, T. Yonezawa, M. T. Nguyen, and X. Lu, Cladding Layer on Well-Defined Double-Wall TiO2 Nanotubes, *Langmuir,* 2015, **31**, 1575.

Presentations in Academic conference:

[1] Efficient and Stable Photoluminescence from Copper Coated Porous Silicon. *Chemistry Society of Japan, Summer Session of Hokkaidao Branch*, 12th July, Muroran, 2014 (Oral presentation).

[2] Efficient Terahertz Emission from Interface Schottky Field on Porous Silicon. *Japan Metallic Association, Summer Session of Hokkaidao Branch*, 28th July, Sapporo, 2014 (Poster presentation).

[3] Improved Terahertz Emission from Schottky Contact on Porous Silicon, *Japan Society of Applied Physics Autumn Meeting*, 17th September, Sapporo, 2014 (Oral presentation).

[4] Photoluminescence Behaviors from Copper Coated Porous Silicon, *Annual Meeting on Photochemistry 2014*, 12th October, Sapporo, 2014 (Oral presentation).

[5] Terahertz emission from CuxO/Au thin film. *Microwave Photonics (MWP) and the 2014 9th Asia-Pacific Microwave Photonics Conference (APMP),* 23rd October, Sapporo, 2014 (Poster presentation).

[6] Double Photoluminescence Bands from Anodized SiCu Composite, *The 3rd International Doctoral Students Symposium*, 26th October, Sapporo, 2015 (Oral presentation).

Acknowledgement

In the past three years in Japan, I received a lot of kind helps from many wonderful people here. I want say “Arigado” to them for their time, guidances and helps.

First of all, I would like to thank my supervisor, Prof. Tetsu Yonezawa who has always supported me in my doctoral research. He gave me many crucial suggestions on my research from his wide knowledge and rich experience. His logical, practical, creative and flexible way of thinking also inspired me so much on my doctoral research. His hard-working, high-efficiency, modesty and wide view are very important for me to learn in my future work. My experience in his research group will be of great benefit for me.

I also would like to thank my lab-staffs assistant Prof. Yohei Ishida and Thanh Mai Nguyen. They gave me great help on my experiment, scientific discussion as well as other activities in Japan.

The system of English Engineering Education is beneficial for the international students to study in Hokkaido University, it gave me many chances to get close to Japanese society. And, I should also thank China Council Scholarship which supports my life in Japan.

In Hokkaido University, I should also say thanks to, assistant Prof. Fujita in Laboratory of Chemical Reaction Engineering, associate Prof. Mishina in department of science, Ms. Kyoko Kawamura and Yuki Tsuji in the international Affairs Office of Engineering, Coordinator Natalya Shmakova in the system of English Engineering Education, Also, many people around me gave me many help and they will be a good memory for me.

Resume

Educational background

30/06/2005	High school of Hualong district, Henan, China	graduated
14/09/2005	Department of Physics, Henan Normal University	enrolled
01/07/2009	–same as above–	graduated
01/09/2009	Master's program, Division of Optics, School of Physical Engineering, Zhengzhou University	enrolled
01/07/2012	–same as above–	graduated
01/10/2012	Doctoral program, Division of Materials Science and Engineering, Graduate School of Engineering, Hokkaido University	enrolled
25/09/2015	–same as above–	coursework expected to complete

Research background

01/09/2009–01/07/2012 Division of Optics, School of Physical Engineering, Zhengzhou University, The optical properties of surface modified Si in terahertz range.

01/10/2012–25/09/2015 Division of Materials Science and Engineering, Graduate School of Engineering, Hokkaido University, The functionalization of surface modified Si.